Tor Vergata University, Rome, Italy

Department of Computer, Systems and Production Engineering

GeoInformation Ph.D.

PolSOM and TexSOM in Polarimetric SAR Classification

MENTOR

Prof. Domenico Solimini

CANDIDATE

Cosimo Putignano

June 2009

Tor Vergata University, Rome, Italy

Department of Computer, Systems and Production Engineering
GeoInformation Ph.D. Thesis

PolSOM and TexSOM in Polarimetric SAR Classification

Mentor

Prof. Domenico Solimini .....

Candidate

Cosimo Putignano .....

June 2009

Alla mia famiglia e ad Agne

Acknowledgements

> Investigare è vedere quello che tutti hanno visto, ma pensare quello a cui nessuno ha mai pensato.
>
> Werner Karl Heisenberg
> (1901–1976)

I would like to acknowledge Prof. Domenico Solimini for his valuable support always provided during all these years of study, Prof. Giovanni Schiavon and Prof. Fabio Del Frate for their advices during this research.

Marco Del Greco is gratefully acknowledged for the fruitful collaboration during the development of the algorithms.

Sento il dovere di ringraziare tutte le persone che in modo diverso hanno contributo alla mia formazione. Tra questi vi sono gli studenti, i dottori ed i professori del laboratorio di Telerilevamento dell'Università Tor Vergata di Roma: Prof. Paolo Ferrazzoli, Prof.ssa Leila Guerriero, Michele Iapaolo, Andrea Minchella, Andrea Della Vecchia, John Peter Merryman Boncori, Chiara Solimini, Riccardo Duca, Bambang Trisasongko, Andrea Radius, Emanuele Angiuli, Pasquale Sellitto, Marco Lavalle, Giorgio Licciardi, Fabio Pacifici, Michele Lazzarini, Emanuele Loret, Matteo Soccorsi.

Rivolgo un particolare ringraziamento ad Alessandro Burini, prezioso collega di studio e lavoro, oltre che insostituibile amico, con il quale ho condiviso e continuo a condividere i momenti di gioia e difficoltà che la vita ci riserva; Antonio e Federico, per voi "grazie" non sarà mai abbastanza.

Non posso non ringraziare gli amici "romani" (Fabiana, Marcello, Silvano, Roberta, Valeria, Giovanni, Luca, Stefania, Carlo, Paolo, Giuseppe, Clara, ecc.) ed alberobellesi (Vittorio, Francesca, Scupett, Ciccio, Leo, ecc.) per avermi supportato ed incoraggiato durante le scelte.

Desidererei ringraziare la mia famiglia: mamma Silvana, papà Giuseppe, mia sorella Alessandra, mia zia Cosima, mio zio Pierino e i miei due *fratelli* Mimmo (2/2) e Lorenzo, per esserci sempre e in ogni caso; loro mi avrebbero sostenuto con lo stesso affetto qualsiasi cammino avessi deciso di intraprendere. Ringrazio i miei parenti di Conversano (zii e cugini) per i quali sarò sempre "Mino di Alberobello", ringrazio i miei nonni Cosimo e Nunzia, Rita e Lorenzo, per avermi guardato sempre con un sorriso. Grazie anche ad Aurelija, che è riuscita a trasmettermi molto, senza bisogno di parlare.

Infine grazie ad Agne, gražiausias dalykas man nutikęs gyvenime.

Crist Crist aijout all'artist, cha
l'uomn d for s'à vaitn d'appllor.

Contents

Abstract

The polarimetric observables in a SAR image possess an intrinsic physical information [1], what makes polarimetric data fit to unsupervised classification [2], without need of *a–priori* information on the scene. Indeed, in natural targets, like vegetation, surface, volume and sometimes double-bounce scattering mechanisms are mixed, while backscattering from man-made targets can be usually attributed to dihedrons, trihedrons and bare surfaces. In many cases a radar resolution cell hosts more than one mechanism, although an average or dominant scattering mechanism can be identified for the purposes of classification. Following Chandrasekhar's pioneering target decomposition [3] and the generalized and systematic theory by Huynen [4], a number of approaches to the interpretation of the scattering processes and to the identification of scatterers have appeared in the open literature, e.g., [5], [6], [7], [8].

Target decomposition theory laid down the basis for the classification of radar images. In particular, the formalism worked out by Cloude [9], [10] led to the introduction of an unsupervised classification scheme [11], further augmented and improved by subsequent contributions [12], [13], [14], also connecting the fuzzy logic theory [15], [16] with Wishart's statistical approach and electromagnetic modeling [17], [18].

Neural Network Algorithms (NNA) have been used in multispectral images classification [19] and for change maps [20], but their application

to polarimetric SAR image classification is more limited. In supervised schemes, the NNA were trained by Huynens parameters [21], or by the polarimetric coherence matrix [**T**], H and α [22]. Unsupervised Neural Net classifiers, based on Self-Organizing Maps (SOM) [23], have exploited Müller matrix directly [24], polarization signatures [25], or parameters derived from decomposition, like Huynen's [26], or Freeman's [27].

In this Thesis two novel unsupervised classification algorithms, named PolSOM and TexSOM, for polarimetric data are proposed. Both algorithms are SOM–based and have been tested on complex Italian landscapes, where classification can become quite challenging and a limited use of polarimetric data has been reported for undulating, heterogeneous and fragmented scenarios.

AIRSAR fully polarimetric data from MAC-Europe Campaign and RADARSAT–2 data acquired for a SOAR project (SOAR–1488) have been classified and confusion matrices have been computed from ground truth maps.

PolSOM and TexSOM performances have been compared with each other and with consolidated and commonly used classification method, to assess their potential. The Neural Network algorithms have been carefully designed based on an in-depth analysis of their operation and, for the first time at the author's knowledge, both object-based and pixel-based information are jointly used in Radar polarimetric image analysis. The proposed classification algorithms are proving to be fairly versatile and not strictly confined to polarimetric images, like the other considered algorithms.

Introduction

This thesis consists of three parts. The first chapter regards the state of the art, where major developments in Radar polarimetry are reviewed. A synoptic table is provided, which summarizes most of the classification methods for polarimetric images. The rationale driving this research is also highlighted.

The second chapter describes some widely used classification algorithms of polarimetric data and provides details on the self organizing map method in polarimetry.

Finally, two novel neural–networks based methods for unsupervised classification of polarimetric SAR data are proposed, critically discussed and compared with other unsupervised approaches.

Chapter 1

State of the Art

This chapter aims at presenting a review of the development of Radar polarimetry for Earth Observation and summarizes recent methods for polarimetric data classification.

1.1 Radar polarimetry historical background

Reviews on the history of radar polarimetry can be found in literature [4], [28]. Early stages are related to the development of radar technologies and, in particular, to the progress during World War II. Initial work on specific radar polarimetry is attributed to Sinclair [29], after whom the scattering matrix was named. It is known that the information provided by a fully polarimetric radar can be arranged in matrix form. In that way, a single data can be viewed as a $[2 \times 2]$ complex scattering matrix (simply named scattering matrix or Sinclair matrix) whose entries represent measured backscattering for the four combinations of transmitted-received polarizations in an orthogonal basis.

Later, an important pioneering work was done by Kennaugh [30], who defined the concept of optimal polarization for a target in the monostatic case and whose ideas were the basis of further advances throughout the fifties

and sixties. From that period it is important to note: the works by Rumsey [31] on the study of the transmission between elliptically polarized antennas by making use of the impedance concept that appears in transmission lines; the works by Deschamps ([32], [33]) on the geometrical representation of polarization on the Poincaré sphere; the works by Kales [34] on the polarization efficiency concept and those by Bohnert [35] on experimental issues.

Advances took place in practical applications about the information provided by the scattering matrices, e.g., Graves [36] showed that the scattering matrix can be reduced to diagonal form by sub-group transformations. That eigenanalysis was further employed by Bickel ([37], [38]) to define some quantities that entirely specify the scattered return from a body. By using the Poincaré sphere, Copeland [39] demonstrated how to classify a target according to its polarization transforming properties, whereas Lowenschuss [40] postulated that it is possible to distinguish between objects of similar shape by looking at polarization responses.

The subsequent important milestone in radar polarimetry was the work carried out by Huynen [4] on target decomposition theory. He contributed a first generalization of the decomposition techniques and renewed the interest of the remote sensing community in radar polarimetry[1].

After that, Ioannidis [41] reported a method to use polarization to discriminate between radar targets and background clutter. The importance of polarization in various inverse problems at different frequency bands and with many applications, was theoretically shown by Boerner [42]. Two reviews about polarization diversity in radar were also presented in [43] and [44].

The understanding in the variation of the scattering coefficients with polarization increased with the introduction of the concept of wave synthesis [45] and a new way to display the polarization dependence of the radar cross section (called polarization signatures (Sect. (2.1.5)). With those, the polarization characteristics of a scene can be synthesized and studied at any possible polarization by only measuring two orthogonal polarizations. These

[1] Principles of target decomposition theory are detailed in section (2.1.7).

studies, mainly based on two-dimensional plots, were extensively employed in subsequent years for analyzing the scattering mechanisms present in natural scenes. Apart from target decomposition, there have been more recent notable developments in aspects regarding radar polarimetry. Some important workshops focused on polarimetry were held, in which several authors contributed significant advances [46]. Moreover, two useful books have been published, illustrating the early applications of radar polarimetry to remote sensing of the earth's cover ([47], [48]) and including theoretical modeling of natural targets, operational aspects of polarimetric SAR and examples with real data. Finally, it is important to cite contributions from some authors to calibration issues: Wiesbeck [49], Freeman ([50],[51]), Van Zyl [52] and Sarabandi ([53], [54]).

1.2 Classification Techniques

The main advantage of polarimetry for constructing classification schemes is that no *a-priori* knowledge about the scene is required because the observables have an intrinsic physical meaning. This fact makes polarimetric data ideal for unsupervised classification, as firstly attempted by Van Zyl [2]. Since some supervised applications are present in literature, the general breakdown for the classification methods in supervised (Sect. 1.2.3) and unsupervised (Sect. 1.2.2) will be maintained.

Details on main classification techniques are now given. It is pointed out that Target-Decomposition based methods (Sect.1.2.1) represent the foundation in radar polarimetry analysis and almost all classification algorithms, both supervised and unsupervised are based on them.

In section (1.2.4), attention is focused on neural networks approach, whereas in section (1.2.5) a synoptic table (Tab. 1.1) showing the classification of the algorithms is provided.

1.2.1 Target Decomposition

The main objective in radar remote sensing is to extract information about a target by observing the backscattering.

Wave interaction with natural or man–made media depends on geometry (i.e., size, shape, orientation distribution and spatial arrangement of the objects in the radar resolution cell) and dielectric properties of the target. The interaction conveys the information on the target into the various quantities measured by Radar. These observables can be arranged in matrices, of which the scattering matrix is the basic one. A sound theory relates the features of measurement matrices to the polarization features of backscattering and in turn to the target characteristics (Sect. (2.1.7)). For classification or for parameters retrieval, target can be characterized through an average or dominant scattering mechanisms, resulting from the various mechanisms co–existing in the scattering cell. However, identification and quantification of the elemental mechanisms contributing to the overall scattering can be a powerful tool for characterizing the target. This is the core idea of Target Decomposition (TD) theory, whose aim can be summarized as the decomposition of the cell–averaged matrix into a sum of independent matrices representing independent elements and the association of a scattering mechanism with each element in the cell.

Many targets of interest in radar remote sensing require a multivariate statistical description due to the combination of coherent speckle noise and random vector scattering effects from surface and volume. For previous targets, it is of interest to generate the concept of an average or dominant scattering mechanism for classification purposes or inversion of scattering data. TD theorems are aimed at providing such an interpretation based on sensible physical constraints such as the average target being invariant to changes in wave polarization base. Summarizing, therefore, the aim of TD is: to decompose or express the average matrix into a sum of independent matrices representing independent elements and to associate a physical mechanism with each element.

This decomposition leads to an easier interpretation of the scattering processes. The first documented example of decomposition appeared in [3], where Chandrasekhar proposed the decomposition of the scattering by a cloud of small anisotropic particles into the sum of a conventional Rayleigh scattering term plus a randomly polarized noise term (due to the particle anisotropy). The generalization of the TD approaches to other

scattering problems was addressed later by Huynen [4]. Since then, there has been a great interest in the formulation of TD theorems for establishing a unified scheme of analysis and a complete mathematical description of the problem in order to avoid ambiguities and incoherences between alternative approaches.

Following the indications of Cloude [55], TD theories can be classified according to the kind of matrix that is effectively decomposed as a sum of matrices and, also, to the type of analysis carried out with the averaged matrices. There are three main groups of TD theories:

- those employing coherent decomposition of the scattering matrix;
- those based on the Müller matrix (Sect. (2.1.9)) and Stokes vector (Sect. (2.1.11)), named also Huynen type decomposition;
- those using an eigenvector analysis of the covariance or coherency matrix (Sect. 2.1.14).

There have been many cases of the three classes in the literature and some hybrid approaches have also been proposed.

1.2.1.1 Coherent Decomposition Theorems

A first class of TD theorems are coherent decomposition theorems where the scattering matrix is expressed as the complex sum of basis matrices like the Pauli matrices (Sect. (2.1.12)). In this approach, with each basis matrix an elementary scattering mechanism is associated.

It has been demonstrated [55] that an orthonormal basis is needed for decomposition purposes to the generation of a polarimetric scattering vector (vectorization of the scattering matrix), from which second order statistics may be defined. One example in [55] shows how the scattering matrix decomposition singles out four scattering mechanisms: single scattering from a flat rough surface, diplane scattering with a relative orientation of 45^0 and orthogonal scattering, i.e., transforming each incident polarization into its orthogonal state.

Two other approaches to coherent TD, were formulated by Krogager ([6], [56]) and Cameron ([5], [57]) who have proposed specific but very different linear combinations of the scattering matrix. Krogager postulated the separation of a coherently averaged scattering matrix into a weighted sum of the scattering matrices of a sphere, a diplane and an helix ([58], [59], [60]). Note that, as shown in [55], this particular selection of elementary targets entails that the single components of the decomposition are not orthogonal and that the decomposition is not basis invariant.

In the Cameron approach, the scattering matrix is decomposed, again using the Pauli matrices, in terms of basis–invariant target features. Cameron considers a class of targets termed symmetric, which have linear eigenpolarizations on the Poincaré sphere (Sect. (2.1.1)) and have a restricted target vector parameterization [55]. Cameron was able to show that a general scattering matrix can be expressed as a linear combination of two symmetric components. One strength of this approach is that the three components are orthogonal and that the minimum symmetric component has only one free parameter, its absolute phase angle. These two examples highlight a major problem with coherent decompositions: there are many ways of decomposing a given scattering matrix, and without *a–priori* information, it is impossible to apply a unique decomposition, even if the methods can be considered unsupervised. Besides these drawbacks, the key issue of the averaging must be pointed out. The fields scattered from a set of elementary targets in a resolution cell add coherently to produce the field received by the Radar. Since the received signal result from a variable interference between field contributions, space–time fluctuations are observed. This phenomenon is known as coherent speckle and must be accounted for when dealing with data from a coherent radar (the physical origin of speckle is described in [61]). To solve this problem, which can be treated as a multiplicative noise, there are a number of techniques available (see for instance [62] for a review on speckle filtering techniques and ([63], [64]) for speckle in the specific polarimetric case), but they generally involve an incoherent averaging to arrive at the second order statistics which are needed to represent this type of noise. An improvement in Cameron decomposition was given by Touzi [8]. He proposed a technique to identify pure targets in SAR images, based

on the Cameron decomposition. This technique determines the nature of a target on the maximum symmetrical component of the Cameron decomposition. In conclusion, the TD theories based on coherent averaging of the scattering matrix are exposed to problems due to speckle, so they are not appropriate when applied to radar remote sensing of natural random targets like vegetation. Nonetheless, they are still suitable when the scene is dominated by a single scattering element, or a few of them and, under certain specific conditions, a radar with high resolution is employed [58].

1.2.1.2 Müller matrix and Stokes vector Decomposition Theorem

This class of TD theories is based on matrices resulting from an incoherent averaging, thus avoiding the effect of coherent speckle. As an example of the application of the target vector formalism to random media scattering it is important to consider the Mischenko decomposition [65]. Even if that method was initially applied to the problem of multiple scattering from a cloud of particles, he showed that there is a simple but important relationship between the coherent and incoherent multiple scattering contributions and some implications of this result for remote sensing applications have been explored [66]. Müller matrix based decomposition Theorem, also named Huynen type decompositions, because he was the first to propose such a method [4], usually works with the Müller matrix. Huynen type theories attempt the extraction of a single scattering matrix from the averaged data and the remainder is assigned to a distributed target or a "noise" contribution, but not to other single scattering component. Other examples in this sense are Chandrasekhar decomposition [3] and the Barnes/Holm decomposition. The physical interpretation of the coherency or covariance (Sect. (2.1.13)) matrix had also been addressed by a particular case of a Huynen type decomposition which was proposed by Freeman ([67], [68], [7]). Freeman decomposition models the covariance matrix as the contribution of three scattering mechanisms:

- *volume scattering*, where a canopy of scatterers is modeled as a set of randomly oriented dipoles;

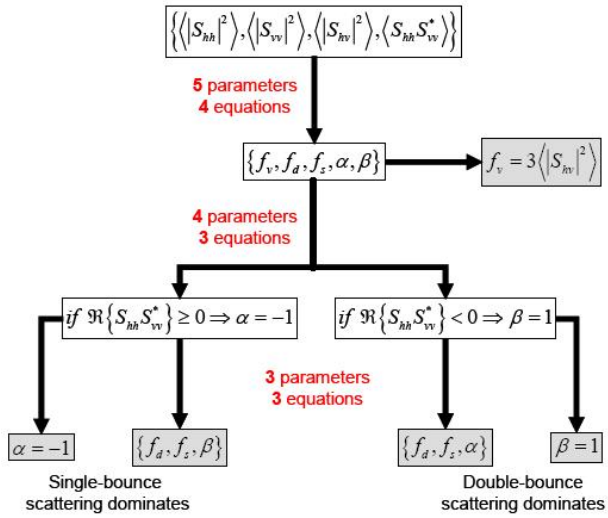

Figure 1.1: Inversion of the Freeman decomposition parameters [69].

- *double-bounce scattering*, modeled by a dihedral corner reflector;
- *surface or single-bounce scattering*, modeled by a first-order Bragg surface scatterer.

In Fig. 1.1 the scheme employed to invert the Freeman decomposition is shown.

It was demonstrated [55] that it is not applicable to a wide range of scattering problems. However, when applied to some observations of mature forests it has been quite useful for discrimination and classification purposes.

1.2.1.3 TD based on the eigenvector analysis of the covariance or coherency matrix

The third and final class is represented by eigenvector decompositions of the coherency or covariance matrix (Sect. (2.1.14)). This class of TD theories is also based on matrices resulting from an incoherent averaging, but the goal

of the eigenvectors-based TD analyses is to represent the averaged data as a summation of single scattering mechanisms. The selection of these single scattering mechanisms is based on statistical independence between them. At first sight, the TD based on eigenvector analyses has two fundamental advantages:

1. The eigenvalue problem is basis invariant;

2. The solution of the problem leads to a diagonalization of the coherency matrix, thus yielding statistical independence between the set of scattering processes;

The development of this last class of TD theories can be considered quite recent, since it started about the middle 1980s. The starting point was a new formalism presented in [9] for describing depolarizing systems. Although the physical interpretation of this theory was clear since the beginning, its application to remote sensing still took some years. In the meantime, the complete algebraic description of this formalism was rigorously formulated by Cloude([10], [70]). This was the first example where an eigenvector decomposition of the coherency matrix was shown. Cloude identified an important basis invariant parameterization in terms of three eigenvalues and a set of angles (obtained from the unitary eigenvectors). These parameters were related to physical scattering mechanisms in the scene and, for the special case of reflection symmetry, were used to model the random media problem as a single scattering mechanism with a degree of disorder, the entropy, consisting in a logarithmic sum of eigenvalues.

1.2.2 Unsupervised

Turning back to the interpretation of the different parameters that appear when the eigenvector decomposition is performed, besides entropy, two new parameters with a physical meaning were defined by Cloude in [11]: an angle related to the type of scattering mechanism (alpha), and an orientation angle of a canonical target that represents the scattering mechanism (beta) (Sect. (2.1.14)). Moreover, [11] presents a classification scheme for polarimetric

SAR images based on the combination of entropy and alpha. An additional parameter, called anisotropy, was proposed in [12] in order to form, together with entropy and alpha, a useful set of parameters for classification purposes. After the introduction of H/A/α classification algorithm, a lot of hybrid algorithms were proposed. In quite all this new methods, the Cloude's parameters are used to train supervised algorithms, or to define decisions rules.

The first improvement in H/A/α was the assumption of the complex Wishart distribution for the polarimetric covariance matrix (Sect. (2.1.13)) [13]. In this algorithm, Cloude's method was used to initially classify the polarimetric SAR image and then, from the initial map, a training set is derived for a maximum likelihood classifier based on the Wishart distribution. The deficiency of the previous approach was that the classification result lacked details, because of the preset zone boundaries in the H and α plane. Indeed, with that classification method, clusters may fall on the boundaries and more than one cluster may be enclosed in a zone [14]. In order to solve this problem, a new solution was proposed by [14] (Sect. (2.1.15)). Unlike other algorithms that classify pixels statistically and ignore their scattering characteristics, the algorithm proposed by Lee not only uses a statistical classifier, but also preserves the purity of dominant polarimetric scattering properties. In brief, the algorithm uses a combination of a scattering model-based decomposition developed by Freeman and Durden and the maximum likelihood classifier based on the complex Wishart distribution. The first step consists of the application of the Freeman and Durden decomposition to divide pixels into three scattering categories: surface scattering, volume scattering, and double-bounce scattering. To preserve the purity of scattering characteristics, pixels in a scattering category were restricted to be classified with other pixels in the same scattering category. A class initialization scheme was also devised [1.2] to initially merge clusters from many small clusters in each scattering category by applying a merge criterion developed on the basis of the Wishart distance measure. Then, the iterative Wishart classifier was applied. The stability in convergence was much superior to that of the previous algorithm using the H/A/α-Wishart classifier.

Some examples of fuzzy clustering algorithms applied to polarimetric

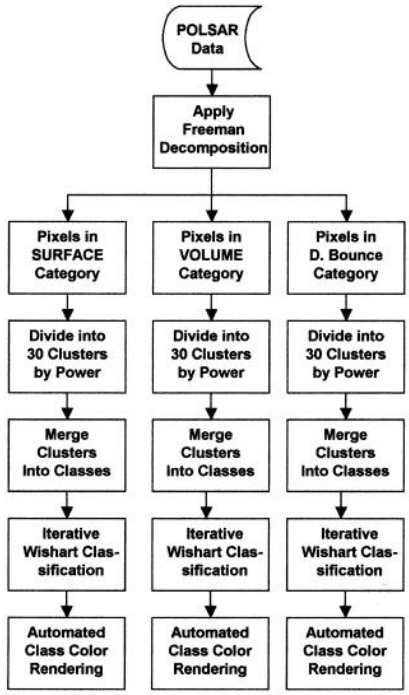

Figure 1.2: Flowchart of the algorithm proposed by Lee [69].

SAR classification where also tested ([71], [15], [16]). Kersten [17], together with J. S. Lee, connected the fuzzy logic theory with Wishart statistical approach. In that work five clustering techniques were compared for fully polarimetric SAR classification purposes. They showed that pixel model is more important than the clustering mechanism. The fuzzy logic technique was also used to improve separation among the zones of H/α method (Fig. 1.3) [18] (Sect. (2.1.14)).

In another research, image segmentation and clustering techniques were based on H/α/A and the power SPAN (Sect. 2.1.14), together combined with a log–likelihood clustering estimator [72]. The following were derived from the experiment:

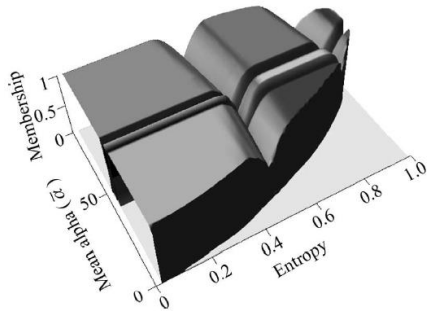

Figure 1.3: Fuzzy membership functions applied to each zone in the H/α plane [18].

1. SPAN has additional information that is not contained in H/α/A;

2. Data log–likelihood has the potential ability to reveal the inner structure of fully polarimetric SAR data.

Electromagnetic models were also used for classification purposes. One of the most important was developed at Tor Vergata University in order to analyze a multi-frequency data [73].

Other important examples of unsupervised algorithms for fully polarimetric unsupervised classification were given by:

1. Schou et al. [74], simulated annealing method was used to improve H/α classification;

2. Rignot et al. [71], the covariance matrix was used to perform an unsupervised segmentation;

3. Fukuda et al. [75], a wavelet–based texture feature set was derived and applied to multifrequency polarimetric images;

4. Wang et al. [76], method based on independent component analysis (ICA). Several independent components are extracted from the channels and classified by Fuzzy–C–Mean method;

5. Hong et al. [77], the Gaussian Markov random field model was applied to the classification of multi-frequency polarimetric SAR data. Previous technique was also explored by Tran et al. in [78];

6. Yong et al. [79] and Lardeux et al. [80], methods based on Support Vector Machine techniques;

7. Rodionova [81], two-stage classification was performed using Freeman and Durden decomposition and textural features obtained from gray level co-occurrence matrices;

8. Hoekman et al. [82], consisting in a six steps method for image segmentation;

9. Reigber et al. [83], Fuzzy logic approach was mixed with K-Means classification algorithm.

1.2.3 Supervised

As mentioned before, the main advantage of polarimetry for constructing classification schemes is that no *a-priori* knowledge about the scene is required because the observables have an intrinsic physical meaning. Anyway, some supervised techniques have been developed. Supervised classification relies on the a priori knowledge of the location and identity of land cover types that are in the image. In this sense coherent target decomposition approaches may be viewed as supervised, because for the target classification or detection, the electromagnetic structure (dihedral, helix, etc.) of the target itself must be known. Other supervised approach were performed by:

1. Martinez et al. [84], where Multifractal features are used in a supervised segmentation;

2. Benz [16], where a fusion of a supervised learning fuzzy distribution estimator and an unsupervised learning fuzzy vector quantizer is proposed;

3. Du et al. [85], where a supervised classification using target decomposition theorems and the complex Wishart distribution was used.

1.2.4 Neural-Network Based

Artificial neural networks have been of major interest in many research areas and a wide range of applications have been presented. In particular, neural networks have been reported as a successful tool for medical and industrial image processing. Neural networks also have been used in remote sensing classification as well and have been reported to classify multi-spectral imageries, like as: [86], [19], [87] and for multi-spectral change maps purposes [20]. The use of neural networks for classification of SAR data also has been presented [88].

However, very limited articles have been found utilizing neural network, particularly for polarimetric SAR data and, in general, many reports are limited to the use of supervised method. There are, also, some hybrid applications, reported in section (1.2.4.3).

1.2.4.1 Supervised

One of the first work utilizing supervised neural network for polarimetry was proposed by Pottier [21]. In that work, starting from the scattering matrix, Müller matrix was calculated and decomposed, in order to obtain Huynen parameters. Finally, those parameters were used to train the net. Pottier's idea was raised again in 1998 [22] but with the difference that instead of Huynen parameters, H and α parameters of the polarimetric coherence matrix (Sect. (2.1.13)) were used. In 2002, neural network performances were compared with a statistical approach based on simulated annealing technique. In that work, the two techniques were found to behave in a similar fashion when applied for the classification of multipolarimetric/multifrequency SIR–C SAR images.

1.2.4.2 Unsupervised

The majority of the researches in unsupervised method are focused on Self-Organizing Map, widely acknowledged as Kohonen Map [23]. First studies were performed by Pottier et al. in [26] and [24]. Pottier et al. exploited the use of Huynen parameters together with unsupervised networks, oppositely to the research performed in [21]. In the work performed by Hara et al. [24] instead of Huynen parameters, unsupervised neural classification was performed directly on the Müller matrix. Hara et al. continued with their research on neural networks and one year after, they proposed an application on Sea Ice [89]. A new approach was presented by Ito and Omatu [25], where polarization signatures were used instead of input data. In [90] Hosokawa and Hoshi presented a supervised use of Self-Organizing Map. An additional layer (Grossberg layer) was added to the net in order to perform the training phase. In [91] the parameters of the co-occurrence matrix (extracted from the gray level image) together with H and α parameter were used to perform unsupervised classification, whereas in [27] elements of the polarimetric coherency matrix, derived features like Freeman decompositions, Alpha, Entropy, Anisotropy, and eigenvalues of the coherency matrix were used.

1.2.4.3 Hybrid Neural Network algorithms

Some hybrid approaches were also proposed. In [92] and [93] a Principal Components Analysis was preformed before the back-propagation neural network training. Especially in the second work, PCA was used in order to reduce the size of the network. The problem of the data volume reduction, was also tackled by Chen et al. [94] in order to improve the efficiency of the neural classifier. They solved the problem with a correlation analysis techniques to remove redundancy from the training data. They showed that with P–band HH polarization, L–band VH polarization, L–band HH polarization, C–band HH polarization and C–band VV polarization the results was very close to those obtained using full information. In [95] and [96] fuzzy membership function were used before the neural classification and, finally, in [97] a mixed architecture using supervised and unsupervised

neural networks was introduced.

1.2.5 Synopsis

In this section a Synoptic table containing analyzed classification methods is provided.

Algorithm	*Supervised*	*Unsupervised*	*Hybrid*
TD 1		Pauli	
TD 1		[6]	
TD 1		[5]	
TD 1		[8]	
TD 1		[66]	
TD 1		[4]	
TD 2		[3]	
TD 2		[98]	
TD 2		[67]	
TD 3		[55]	
H/A/α		[11]	
H/A/α Wishart		[13]	
Lee Polarimetric category preserving		[14]	
Fuzzy logic		[71]	
Fuzzy logic		[15]	
Fuzzy logic		[16]	
Fuzzy-Wishart		[17]	
Fuzzy-H/A/α		[18]	
H/A/α SPAN		[72]	
Model Based		[73]	
Simulated Annealing H/A/α Covariance matrix		[74] [71]	
Wavwlet and Texture		[75]	

Table 1.1 – Continued on next page

Algorithm	*Supervised*	*Unsupervised*	*Hybrid*
Fuzzy logic ICA		[76]	
Markov Random Field Support Vector Machine		[78] [80]	
Freeman-Durden Texture		[81]	
Fuzzy logic K-means Multifractal Features	 [84]	[83]	
Fuzzy logic TD2-Wishart	[16] [85]		
NN trained with Huynen	[21]		
NN trained with H/A/α	[22]		
SOM applied on Huynen parameters		[26]	
SOM applied on Müller matrix		[24]	
SOM applied on polarimetric signature		[25]	
SOM supervised	[90]		
SOM-Texture H/A/α		[91]	
SOM Coherency Matrix		[27]	
Backpropagation- PCA			[92]
SOM-Fuzzy			[96]

Table 1.1: SAR polarimetric data Classification algorithms.

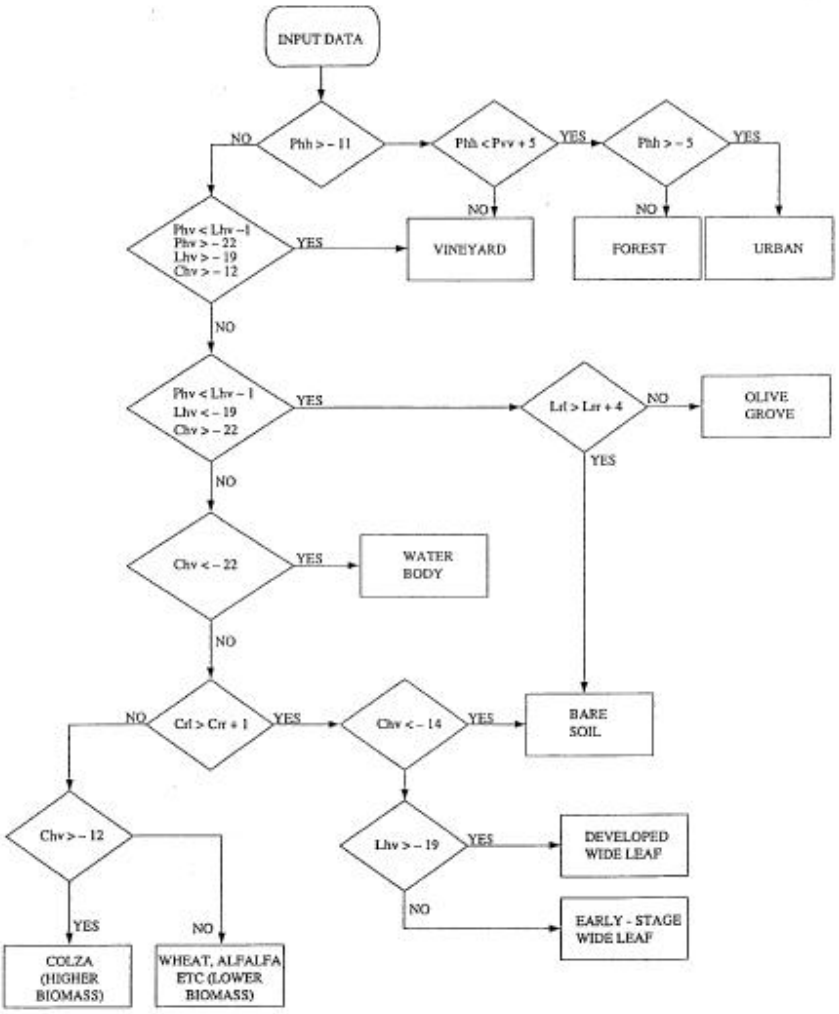

Figure 1.4: Block diagram of the classification algorithm developed at Tor Vergata University, Rome, Italy [73].

1.3 Motivations & Innovations of this research

Classification algorithms described in the previous sections show how different approaches are possible in the analysis of polarimetric data. It is important to emphasize, however, that many of previous methods, born as target detection applications, have been adapted to land cover classification purposes. For the previous reasons, some information necessary for the production of classified maps were not taken into account.

Many of the maps produced for commercial purposes are made by photo interpreters using optical data. These maps are very well detailed and the overall accuracy attains high percentage level, but the processing times are long. That characteristic makes photo–interpretation not applicable when a near real–time processing is needed (i.e., natural disasters). Moreover, Radar data are difficult to photo–interpret and new missions provide data more quickly, greatly decreasing the revisit time with respect to the past missions. However, some trademarks of the "Human–Brain processor" can be used to design a new classification algorithm. The first one is the ability to perform parallel computations, in order to find solutions even if the input data are corrupted. The second one is is the ability of the brain to provide contextual information, this type of information is directly contained in the pixels of the images, but can be extracted only when properties of groups of pixels are considered.

The innovation introduced in this Thesis consists in implementing two new classification algorithms for polarimetric SAR images that, through the use of non-supervised neural networks, are able to manage heterogeneous information and performing parallel computation.

These algorithms are able to exploit the results obtained in many years of study about theory of polarimetric SAR data, and modern concepts about image processing. Improvements in classification overall accuracy with respect to the methods previously described is shown, because new strategies have been used to control the neural network without using it as a black box.

Chapter 2

Polarimetry and SOM background

In this Chapter a brief background about polarimetry an self organizing map is provided. Widely used polarimetric classification algorithms have been described in detail.

2.1 Polarimetry background

2.1.1 Stokes Formalism

In the 1852 Stokes introduced new parameters in order to characterize polarization state of a wave. The parameters S_0, S_1, S_2, S_3, named *Stokes parameters*, are:

$$\mathbf{Y} = \begin{bmatrix} S_0 \\ S_1 \\ S_2 \\ S_3 \end{bmatrix} = \begin{bmatrix} E_h E_h^* + E_v E_v^* \\ E_h E_h^* - E_v E_v^* \\ 2\Re\{E_h E_v^*\} \\ 2\Im\{E_h E_v^*\} \end{bmatrix} = \begin{bmatrix} |E_h|^2 + |E_v|^2 \\ |E_h|^2 - |E_v|^2 \\ 2E_h E_v \cos(\delta) \\ 2E_h E_v \sin(\delta) \end{bmatrix} \tag{2.1}$$

where E_v and E_h are the horizontal and the vertical component of the electric field $\mathbf{E}$, $\delta = \delta_h - \delta_v$ is the phase difference between E_h ed E_v . The parameter S_0 is proportional to the superficial density power related to the wave, S_1 is the the difference between the superficial densities power

related to the horizontal and vertical polarizations. Parameters S_2 and S_3 are related to the phase difference between the h and v components of the electric field. Even if the Stokes vector consists in four parameter, only three of them are independent:

$$S_0^2 = S_1^2 + S_2^2 + S_3^2 \tag{2.2}$$

For partial polarized waves, not all the superficial density power is contained in the polarized components, as a consequence the total superficial density power is greater that polarized components:

$$S_0^2 > S_1^2 + S_2^2 + S_3^2 \tag{2.3}$$

Considering full polarized waves, Stokes parameters are:

$$\mathbf{Y} = \begin{bmatrix} S_0 \\ S_0\cos(2\psi)\cos(2\chi) \\ S_0\sin(2\psi)\cos(2\chi) \\ S_0\sin(2\chi) \end{bmatrix} = S_0 \begin{bmatrix} 1 \\ \cos(2\psi)\cos(2\chi) \\ \sin(2\psi)\cos(2\chi) \\ \sin(2\chi) \end{bmatrix} = S_0\hat{\mathbf{Y}} \tag{2.4}$$

where ψ is the inclination angle , χ is the ellipticity angle and $\hat{\mathbf{Y}}$ is the normalized Stokes vector. Polarization state of a fully polarized plane wave can be represented by means of a point P having Cartesian coordinate S_1, S_2, S_3 and belonging at a sphere surface with radius S_0 named *Poincaré Sphere*.

Angle 2ψ defines the latitude of the point P and 2χ the longitude. As previously discussed, the sign of χ characterizes the orientation of the polarization state. Where $\chi > 0$ there are the left-hand polarizations and where $\chi < 0$ there are the right-hand polarizations. At the poles are represented circular polarizations and at the equator the linear ones. Eq. (2.2) is valid for a complete polarization wave; in general Eq. (2.3) must be used. In this sense it is necessary a parameter named *degree of polarization* p:

$$p = \frac{\sqrt{S_1 + S_2 + S_3}}{S_0} \tag{2.5}$$

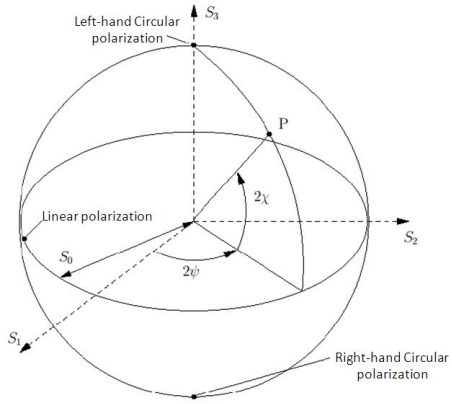

Figure 2.1: Polarization states on the Poincaré sphere.

Considering that Stokes vector can be decomposed in the sum of a fully polarized component and a completely depolarized one, if the degree of polarization p is used:

$$\mathbf{Y} = \begin{bmatrix} S_0 \\ S_1 \\ S_2 \\ S_3 \end{bmatrix} = \begin{bmatrix} 1-p \\ 0 \\ 0 \\ 0 \end{bmatrix} + S_0 p \begin{bmatrix} 1 \\ \cos(2\psi)\cos(2\chi) \\ \sin(2\psi)\cos(2\chi) \\ \sin(2\chi) \end{bmatrix} \tag{2.6}$$

2.1.2 Jones Formalism

In radar applications Jones formalism is preferred. In this formalism for the representation of the wave polarization state a bi-dimensional complex space is used instead of a real tri-dimensional one, typical of Stokes . Electric field of a wave propagating in the z can be written as:

$$\mathbf{E}(z) = \hat{E}_x(z)\mathbf{e}_x + \hat{E}_y(z)\mathbf{e}_y$$

where:

$$\hat{\mathbf{E}}_x(z) = \hat{\mathbf{E}}_x e^{-jkz} = E_{x0} e^{-jkz} e^{j\delta_x} \mathbf{e}_x$$

$$\hat{\mathbf{E}}_y(z) = \hat{\mathbf{E}}_y e^{-jkz} = E_{y0} e^{-jkz} e^{j\delta_y} \mathbf{e}_y$$

the same expression can be rewritten using a complex bi-dimensional vector $\mathbf{J}$ introduced by Jones [99], [100], [101]:

$$\mathbf{J} = \begin{bmatrix} E_x \\ E_y \end{bmatrix} = \begin{bmatrix} E_{x0} e^{j\delta_x} \\ E_{y0} e^{j\delta_y} \end{bmatrix} \tag{2.7}$$

Jones vector contains all the information about the polarization ellipse, but, if two different waves propagating in opposite directions are considered, they can be represented by the same vector. In order to optimize that problem a couple of subscripts are used [102]:

$$\mathbf{E}_+(\mathbf{r}, t) = \Re\{\mathbf{E}_+ e^{j(\omega t - \mathbf{k}\cdot\,\mathbf{r})}\} \tag{2.8}$$

$$\mathbf{E}_-(\mathbf{r}, t) = \Re\{\mathbf{E}_- e^{j(\omega t + \mathbf{k}\cdot\,\mathbf{r})}\} \tag{2.9}$$

Vectors $\mathbf{E}_\pm$ are named *Jones's directional vectors* [103], with $\mathbf{E}_+$ conjugate of $\mathbf{E}_-$. Conjugacy operation applied to Jones's vectors corresponds to the sign change if the phase difference is considered ($\delta = \delta_b - \delta_a$) or rather consists in the change of the orientation related to the state of polarization. Parameter ρ of Eq. (2.20) can be used to define Jones's vectors:

$$\mathbf{J} = \begin{bmatrix} E_{x0} \\ E_{y0} \end{bmatrix} = E_{x0} \begin{bmatrix} 1 \\ \rho \end{bmatrix} \tag{2.10}$$

or, alternatively, Jones's vectors can be expressed as a function of inclination angle ψ and ellipticity angle χ. Considering normalized Jones vector $\hat{\mathbf{J}}$, obtained assuming $|\mathbf{J}| = 1$ [104], the following equation can be defined:

$$\hat{\mathbf{J}}(\theta, \psi) = \begin{bmatrix} \cos\psi\cos\chi - j\sin\psi\sin\chi \\ \sin\psi\cos\chi + j\cos\psi\sin\chi \end{bmatrix} \tag{2.11}$$

where the polarization state is not dependent from the superficial density of power associated to the electromagnetic wave. When $\chi = 0$ all linear polarization are described, in this case Jones vector is dependent only from inclination angle ψ:

$$\hat{\mathbf{J}}_{lin}(\psi) = \begin{bmatrix} \cos\psi \\ \sin\psi \end{bmatrix} \tag{2.12}$$

Circular right-hand and left-hand are expressed in the following way:

$$\hat{\mathbf{J}}_R = \frac{1}{\sqrt{2}} \begin{bmatrix} 1 \\ -j \end{bmatrix} \qquad \hat{\mathbf{J}}_L = \frac{1}{\sqrt{2}} \begin{bmatrix} 1 \\ j \end{bmatrix} \tag{2.13}$$

2.1.2.1 Polarization Basis Change

Polarization ratio changes according to the selected basis. If the orthogonal basis $\{\mathbf{e}_{x1}, \mathbf{e}_{x2}\}$ and $\{\mathbf{e}_{y1}, \mathbf{e}_{y2}\}$ are considered, electric field can assume the following formulation:

$$\mathbf{E} = E_{x1}\mathbf{e}_{x1} + E_{x2}\mathbf{e}_{x2} = E_{y1}\mathbf{e}_{y1} + E_{y2}\mathbf{e}_{y2} \tag{2.14}$$

and:

$$\mathbf{J}_{x1,x2} = \begin{bmatrix} E_{x1} \\ E_{x2} \end{bmatrix} \qquad \mathbf{J}_{y1,y2} = \begin{bmatrix} E_{y1} \\ E_{y2} \end{bmatrix} \tag{2.15}$$

are the related Jones's vectors.

In order to transform one complex vector in another, $[\mathbf{U}]_{2\times2}$ matrix must be used:

$$\mathbf{J}_{y1,y2} = [\mathbf{U}]_{2\times2}\mathbf{J}_{x1,x2} \tag{2.16}$$

The Matrix $[\mathbf{U}]_{2\times2}$ must be unitary; considering ρ_x the polarization ratio referred to the basis $\{\mathbf{e}_{x1}, \mathbf{e}_{x2}\}$, vectors in the new basis $\{\mathbf{e}_{y1}, \mathbf{e}_{y2}\}$ can be written as [105], [56],[106]:

$$\mathbf{e}_{y1} = e^{j\delta_{y1}} \frac{1}{\sqrt{1+\rho_x\rho_x^*}} \begin{bmatrix} 1 \\ \rho_x \end{bmatrix} \tag{2.17}$$

$$\mathbf{e}_{y2} = e^{j\delta_{y2}} \frac{1}{\sqrt{1+\rho_x\rho_x^*}} \begin{bmatrix} -\rho_x^* \\ 1 \end{bmatrix} \tag{2.18}$$

where δ_{y1} e δ_{y2} represent the reference phases in the new basis. It is proved that $\delta_{y1} = -\delta_{y2}$ [107]. Transformation matrix $[\mathbf{U}]_{2\times2}$ represents

the projection of the new basis $\{\mathbf{e}_{y1}, \mathbf{e}_{y2}\}$ in the old one $\{\mathbf{e}_{x1}, \mathbf{e}_{x2}\}$, with $\det([\mathbf{U}]_{2\times2})$=1 [108].

Expression of $[\mathbf{U}]_{2\times2}$ matrix become:

$$[\mathbf{U}]_{2\times2} = \frac{1}{\sqrt{1+\rho_x\rho_x^*}} \begin{bmatrix} e^{j\delta_{y1}} & -\rho_x^* e^{-j\delta_{y1}} \\ \rho_x e^{j\delta_{y1}} & e^{-j\delta_{y1}} \end{bmatrix} \tag{2.19}$$

Reference phase δ_{y1} is not relevant for the determination of polarimetric parameters, for the previous reason usually assumes zero value ($\delta_{y1} = 0$).

2.1.3 Complex polarization ratio

Information about polarization state can be extracted by means of a complex parameter, named *complex polarization ratio* ρ [109] that represents the complex ratio between the orthogonal components of the electric field in a specified basis: for instance, considering $\{\mathbf{e}_x, \mathbf{e}_y\}$ basis:

$$\rho = \frac{E_{y0}}{E_{x0}} \cdot e^{j(\delta_y - \delta_x)} = \frac{\cos(2\chi) + j\sin(2\chi)}{1 - \cos(2\psi)\cos(2\chi)} \tag{2.20}$$

It is also valid:

> *If a particular state of polarization is considered, that imply a particular value of ρ, exists a orthogonal state $\rho_\perp$ that respects the following equation:*
>
> $$\rho\rho_\perp^* = -1 \tag{2.21}$$
>
> *additionally, $\rho_\perp^*$ coincides with the complex conjugate of the complex polarization ratio ρ* [58].

Polarization states that respect Eq. (2.21) play a important role in the polarization theory, as will be shown in the following sections.

2.1.4 Huynen's polarization fork

The Huynen's polarization fork is used for the analysis of of the optimal polarization states [110]. It defines Huynen fork a 4-pronged figure in the

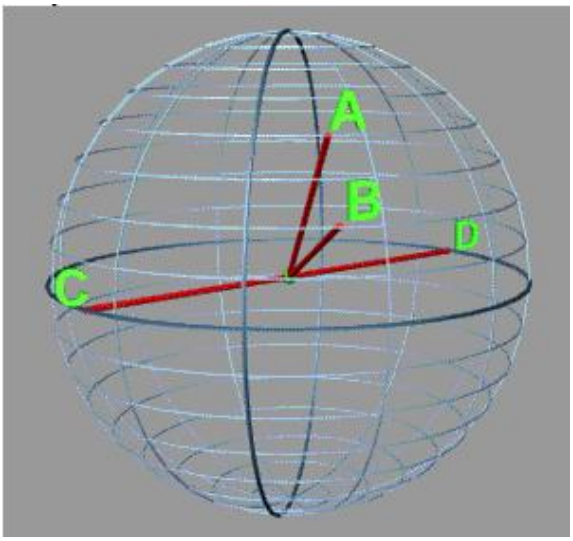

Figure 2.2: Huynen's fork.

Poincaré sphere connecting points of co-pol nulls and cross-pol nulls with the center of the sphere. The line connecting the two cross-pol nulls passes through the center of the Poincaré sphere, and represents two of the prongs of the Huynen fork. The other two prongs are lines from the center of the sphere to each of the two co-pol nulls. In Fig. 2.2, the red lines $(C-D)$ join the two cross–pol nulls, passing through the center of the sphere. The line meets the surface at latitude zero and longitudes -40^0 and $+40^0$. The other red lines $(A-B)$ start from the sphere's center (the green dot), and meet the surface at the co–pol nulls at latitudes $+20^0$ and $+40^0$ and longitude $+20^0$.

2.1.5 Polarization Signatures and pedestal height

Because the incident wave can take on so many polarizations, and the scattering matrix consists of 4 complex numbers, it is helpful to have a graphical method of visualizing the response of a target as a function of the

incident and backscattered polarizations.

One visualization way is provided by the polarization signature of the target. The scattering power can be determined as a function of the four wave polarization variables, the incident and backscattered ellipcity and inclination angles, but these constitute too many independent variables to observe conveniently. To simplify the visualization, the backscattered polarizations are restricted to be either the same polarization or the orthogonal polarization as the incident wave. This choice of polarization combinations leads to the calculation of the co-polarized and cross-polarized responses for each incident polarization, which are portrayed in two surface plots called the co-pol and cross-pol signatures. These two signatures do not represent every possible transmit-receive polarization combination, but a useful visualization of the target's backscattering properties.

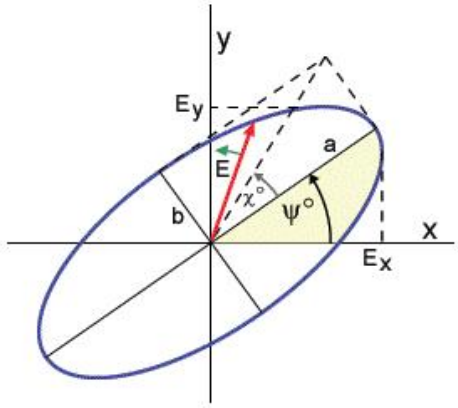

Figure 2.3: Polarization ellipse.

An incident electromagnetic wave can be selected to have an Electric Field vector with an ellipticity χ between -45^0 and $+45^0$, and an orientation ψ between 0^0 and 180^0 (Fig. 2.3). For an incident wave of unit amplitude, the power of the co-polarized (or cross-polarized) component of the scattered wave is presented as the z value on the plots. Often the

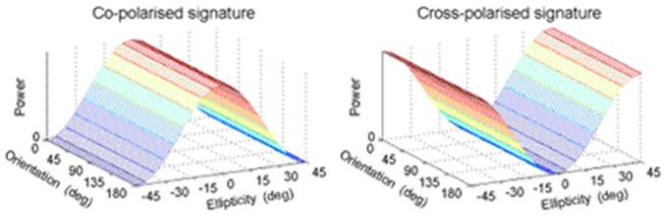

Figure 2.4: Polarization signatures of a large conducting sphere or trihedral corner reflector.

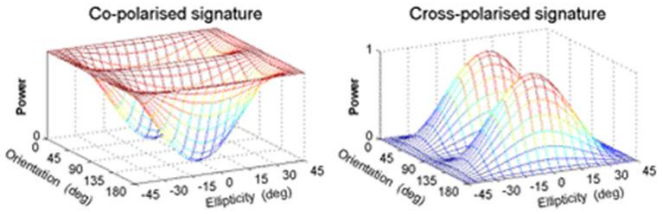

Figure 2.5: Polarization signatures of a dihedral or double-bounce reflector.

plots are normalized to have a peak value of one. The polarization plots have peaks at polarizations that give rise to maximum received power, and valleys where the received power is smallest, in agreement with the concept of Huynen's polarization fork (see section (2.1.4)) in the Poincaré sphere.

Fig. 2.4 shows the polarization signatures of the simplest class of targets: a large conducting sphere or a trihedral corner reflector. The wave is backscattered with the same polarization, except for a change of sign of the ellipticity.

For more complicated targets, the polarization signature takes on different characteristic shapes. Interesting signatures are obtained from a dihedral corner reflector and from Bragg scattering off the sea surface. In the case of the dihedral reflector, when its corner (the intersection of its sides) is aligned horizontally, parallel to the horizontal axis of the EM wave, the co-pol response is a maximum for linear or elliptical horizontal, linear

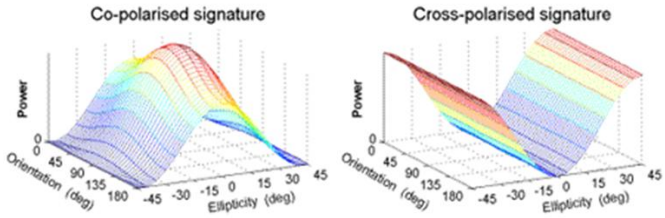

Figure 2.6: Polarimetric signatures of Bragg scattering from the sea surface.

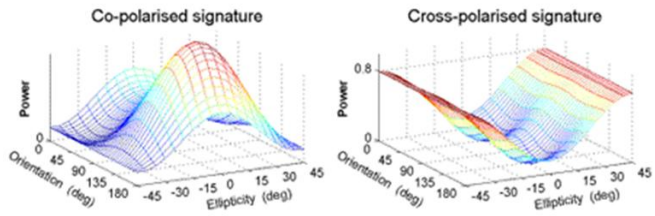

Figure 2.7: Polarization signature of a target having a pedestal height of about 0.2.

or elliptical vertical and circular polarizations (Fig. 2.5). Because the two reflecting surfaces of the dihedral sides negate the sign of the ellipticity a second time, this results in a typical double-bounce or even-bounce signature. However, if the reflector is rotated by 45^0 around the radar line of sight, the linear horizontal co-pol response is zero and the linear horizontal cross-pol response is a maximum. This property means that the dihedral can be used as a simple way of creating a cross-pol response in an HH radar system. In the case of Bragg scattering, the response has a ridged shape similar to the single-bounce sphere, except that the backscatter of the vertical polarization is higher than that of the horizontal polarization (Fig. 2.6). The co-pol response has a peak at orientation angle $\psi = 90^0$ and at ellipticity angle $\chi = 0^0$.

A useful parameter that can be obtained from polarization signatures

is the pedestal height. It represents the minimum value of intensity found on the signature, when the maximum response is normalized to unity. The height of the pedestal is an indicator of the presence of an unpolarized scattering component in the received signal, and thus is related to the degree of polarization of a scattered wave. If a single target is scattering and the backscattered wave is fully polarized, or if the signature is calculated from a single non-averaged measurement, the pedestal height is zero. But if the signature is calculated from an average of several samples (i.e. filtering procedures), and there are multiple, dissimilar scatterers present or there is noise in the received signal, the pedestal height will be non-zero. Thus the pedestal height is also a measure of the number of different types of scattering mechanism found in the averaged samples (Fig. 2.7). A fully unpolarized wave is represented by a plane at 0.5 value and this state is usually named *flat equal power density profile*. In this case polarimetric analisys can not be performed. Usually, for particular kind of targets, the pedestal height and the entropy (Sect. 2.1.14) increase with increasing of frequency. Microwaves at lower frequencies such as L-band and P-band have better ability to penetrate the natural targets and interact more extensively with its structural components (i.e, leaves, branches and trunks). Microwaves at higher frequencies (C- and X-Band) tend to interact primarily with the upper portion of the natural targets and the dominant polarimetric scattering becomes volume.

2.1.6 Scattering Source Grouping

Scattering sources may be grouped in broad categories [111] , each associated to typical scattering behaviors, as shown in [2] and [47]. In particular:

- Soil response can be associated with a rough surface scattering effect. This effect is important for bare soils and, in general, at low frequencies, where many agricultural crops are rather transparent. σ^0_{RL} is appreciably higher than σ^0_{RR} and σ^0_{HV} is low. At lower frequencies (P– and L–band) $\sigma^0_{VV} > \sigma^0_{HH}$, as predicted by the Small Perturbation surface scattering model [112], while at high frequencies (C–Band) $\sigma^0_{VV} = \sigma^0_{HH}$.

- Vertical structures, like forest trunks and crop stalks, produce double-bounce scattering. In general, this mechanism is important at P–band for forests and at L–band for some agricultural crops like corn and sunflower. σ^0_{HV} is low, as in the soil scattering case, but, differently from the soil, σ^0_{HH} is generally higher than σ^0_{VV} and the large difference between σ^0_{RL} and σ^0_{RR} disappears.
- Ensembles of inclined cylindrical structures, like forest branches and crop stems, produce volume scattering with an appreciable presence of multiple scattering. The differences $\sigma^0_{HH} - \sigma^0_{HV}$ and $\sigma^0_{VV} - \sigma^0_{HV}$ are much lower than those for soil and vertical structures. In circular polarization, $\sigma^0_{RL} \approx \sigma^0_{RR}$.
- Ensembles of inclined planar structures, like leaves, also produce volume scattering; however, an appreciable amount of single "facet" scattering is present. $\sigma^0_{HH} - \sigma^0_{HV}$ and $\sigma^0_{VV} - \sigma^0_{HV}$ differences are relatively low, similarly to the cylinder case, but at circular polarization, the "facet" effect generates appreciable positive $\sigma^0_{RL} - \sigma^0_{RR}$ differences.

The scatterer dimension have important effect too. Let branches and stems be represented as ensembles of cylinders with the length proportional to the radius. For a canopy of equal cylinders, the backscatter coefficient changes with the cylinder length (expressed in wavelengths) and show a maximum [113]. It follows that, for each band, there is a range of cylinder dimensions generating a dominant contribution to the backscatter. For leaves, which can be described as discs, scattering is dependent on thickness and moisture content [114].

2.1.7 Backscattering processes matrix analysis

For the representation of the scattering mechanisms two different matrices are used: *Scattering Matrix*, sometimes named Sinclair matrix, and the *Müller* matrix. Both matrices define relations between backscattered wave and incident wave; the main difference is that the Scattering Matrix is based on Jones formalism (Sect. (2.1.2), whereas Müller matrix is based on Stokes formalism (Sect. (2.1.1).

2.1.8 The Scattering Matrix

If the incident plane is expressed as:

$$\mathbf{E}^t = E_h^t \mathbf{e}_h + E_v^t \mathbf{e}_v \tag{2.22}$$

where subscripts h e v denote horizontal and vertical polarization, respectively. The induced currents in the target produce an electromagnetic wave that, in the far–field approximation, can be considered locally plane. The expression of backscattered wave is:

$$\mathbf{E}^s = E_h^s \mathbf{e}_h + E_v^s \mathbf{e}_v \tag{2.23}$$

The scattering process can be formulated by means of a linear transformation matrix based; the expression of the electromagnetic field received from the antenna is [115], [29]:

$$\mathbf{E}^s = [\mathbf{S}]\,\mathbf{E}^t = \begin{bmatrix} E_h^s \\ E_v^s \end{bmatrix} = \frac{e^{-jk_0 r}}{r} \begin{bmatrix} S_{hh} & S_{hv} \\ S_{vh} & S_{vv} \end{bmatrix} \begin{bmatrix} E_h^t \\ E_v^t \end{bmatrix} \tag{2.24}$$

The $[\mathbf{S}]$ matrix is a $[2 \times 2]$ complex matrix from which important characteristics about the target can be obtained. That matrix is named *Scattering Matrix* or *Sinclair Matrix*. Matrix's elements are complex like as $S_{ij} = |S_{ij}|\, e^{j\phi_{ij}}$ where $i, j \in \{h, v\}$. Terms S_{hh} and S_{vv} are named co-polar, whereas terms S_{hv} and S_{vh} are named cross-polar. It is important to note that the matrix does not depend from the distance and can be simplified by means of reciprocity theorem, where cross-polar elements are the same: $S_{hv} = S_{vh} = S_X$ [47]. The following expression can be obtained:

$$[\mathbf{S}] = e^{j\phi_0} \begin{bmatrix} |S_{hh}| & |S_X|\, e^{j(\phi_x - \phi_0)} \\ |S_X|\, e^{j(\phi_x - \phi_0)} & |S_{vv}|\, e^{j(\phi_{vv} - \phi_0)} \end{bmatrix} \tag{2.25}$$

where it is possible to note that independent parameters are 5 (3 amplitudes and 2 phases).

2.1.9 The Müller Matrix

The Eq. (2.6) can be rewritten in the following as in [47]:

$$\mathbf{Y} = [\mathbf{Q}]\mathbf{G} = \begin{bmatrix} 1 & 1 & 0 & 0 \\ 1 & -1 & 0 & 0 \\ 0 & 0 & 1 & 1 \\ 0 & 0 & j & -j \end{bmatrix} \begin{bmatrix} E_h E_h^* \\ E_v E_v^* \\ E_h E_v^* \\ E_v E_h^* \end{bmatrix} \tag{2.26}$$

In the case of monostatic radar, if both transmitted and received waves are represented with the Stokes formalism, the following equation can be written [116]:

$$\mathbf{G^s} = \frac{1}{r^2}[\boldsymbol{B}]\mathbf{G^t} \tag{2.27}$$

or rather:

$$\begin{bmatrix} |E_h^s|^2 \\ |E_v^s|^2 \\ E_h^s E_v^{s*} \\ E_v^s E_h^{s*} \end{bmatrix} = \frac{1}{r^2} \begin{bmatrix} S_{hh}S_{hh}^* & S_{hv}S_{hv}^* & S_{hh}S_{hv}^* & S_{hv}S_{hh}^* \\ S_{vh}S_{vh}^* & S_{vv}S_{vv}^* & S_{vh}S_{vv}^* & S_{vv}S_{vh}^* \\ S_{hh}S_{vh}^* & S_{hv}S_{vv}^* & S_{hh}S_{vv}^* & S_{hv}S_{vh}^* \\ S_{vh}S_{hh}^* & S_{vv}S_{hv}^* & S_{vh}S_{hv}^* & S_{vv}S_{hh}^* \end{bmatrix} \begin{bmatrix} |E_h^t|^2 \\ |E_v^t|^2 \\ E_h^t E_v^{t*} \\ E_v^t E_h^{t*} \end{bmatrix} \tag{2.28}$$

If Eq. (2.26) and Eq. (2.27) are used, the Stokes vector of the diffuse wave $\mathbf{Y^s}$ is:

$$\mathbf{Y}^s = [\mathbf{Q}]\mathbf{G}^s = \frac{1}{r^2}[\mathbf{Q}][\boldsymbol{B}]\mathbf{G}^t = \frac{1}{r^2}[\mathbf{Q}][\boldsymbol{B}][\mathbf{Q}]^{-1}\mathbf{Y}^t = \frac{1}{r^2}[\boldsymbol{M}_m]\mathbf{Y}^t \tag{2.29}$$

where $[\mathbf{Q}]^{-1}$ is the inverse Matrix. The Matrix $[\boldsymbol{M_m}]$ is a $[4 \times 4]$ real matrix that describes the connection between the Stokes vectors of the diffuse and transmitted waves. Different names can be used for the $[\boldsymbol{M_m}]$ matrix.

That Matrix is named phase matrix by Chandrasekhar [3] and is represented by the symbol [**P**], Stokes matrix by Deirmendjian [117] and represented with the symbol $[\sigma]$, transformation matrix by Van de Hulst [118] and represented with the symbol [**F**].

Since the theory of Stokes parameters and their linear transformation was introduced by Müller, in this Thesis the previous matrix will be named

Müller matrix. The complete matrix formulation is the following [119]:

$$[\boldsymbol{M_m}] = \begin{bmatrix} |S_{hh}|^2 & |S_{hv}|^2 & \Re(S_{hh}S_{hv}^*) & \Im(S_{hh}S_{hv}^*) \\ |S_{vh}|^2 & |S_{vv}|^2 & \Re(S_{vh}S_{vv}^*) & \Im(S_{vh}S_{vv}^*) \\ 2\Re(S_{hh}S_{vh}^*) & 2\Re(S_{hv}S_{vv}^*) & 2\Re(S_{hh}S_{vv}^* + S_{hv}S_{vh}^*) & \Im(S_{hh}S_{vv}^* + S_{vh}S_{hv}^*) \\ -2\Im(S_{hh}S_{vh}^*) & -2\Im(S_{hv}S_{vv}^*) & -\Im(S_{hh}S_{vv}^* + S_{hv}S_{vh}^*) & \Re(S_{hh}S_{vv}^* - S_{hv}S_{vh}^*) \end{bmatrix}$$

2.1.10 Basis change for [S] Matrix

Representation by means of [**S**] matrix depends form used polarization basis. Equations analyzed in section (2.1.2) can be used to transform a [**S**] matrix in $\{\mathbf{e}_h, \mathbf{e}_v\}$ basis in the [**S**] matrix in an arbitrary basis $\{\mathbf{e}_x, \mathbf{e}_y\}$ [120]:

$$[\mathbf{S}]_{xy} = [\mathbf{U}]_{2\times2}^T [\mathbf{S}]_{hv} [\mathbf{U}]_{2\times2} \quad where \quad [\mathbf{U}]_{2\times2} = \frac{1}{\sqrt{1+\rho\rho^*}} \begin{bmatrix} 1 & -\rho^* \\ \rho & 1 \end{bmatrix} \tag{2.30}$$

Elements of $[\mathbf{S}]_{xy}$ matrix in the $\{\mathbf{e}_x, \mathbf{e}_y\}$ basis, having polarization ratio ρ are:

$$\begin{aligned} S_{xx} &= \frac{1}{1+\rho\rho^*}[S_{hh} + 2\rho S_X + \rho^2 S_{vv}] \\ S_{xy} &= \frac{1}{1+\rho\rho^*}[\rho S_{hh} + (1-\rho\rho^*)S_X - \rho^* S_{vv}] \\ S_{yx} &= \frac{1}{1+\rho\rho^*}[\rho S_{hh} - (\rho\rho^* - 1)S_X - \rho^* S_{vv}] \\ S_{yy} &= \frac{1}{1+\rho\rho^*}[\rho^2 S_{hh} + 2\rho S_X + S_{vv}] \end{aligned} \tag{2.31}$$

where $S_X = S_{hv} = S_{vh}$ in agreement with the reciprocity theorem.

After the transformation the elements of the [**S**] matrix change, but some properties of the matrix are invariant like as:

1. The *SPAN* of the matrix (sum of quadratic elements of the matrix);
2. The symmetry of [**S**] matrix;

3. The determinant of [**S**] matrix: $\det([\mathbf{U}]_{2\times 2}) = 1$.

It is also valid the reciprocity theorem. Previous properties are usually used to transform a linear polarization into the circular one, in that way all aspects of the backscattered wave can be analyzed. Elements of $[\mathbf{S}]_{RL}$ can be calculated by the following equations:

$$\begin{aligned} S_{RR} &= jS_x + \frac{1}{2}(S_{hh} - S_{vv}) \\ S_{LL} &= jS_x - \frac{1}{2}(S_{hh} - S_{vv}) \\ S_{RL} &= \frac{j}{2}(S_{hh} + S_{vv}) \end{aligned} \tag{2.32}$$

2.1.11 Complex Scattering Vector

The results achieved in the previous section can be also obtained using a four complex-component vector:

$$\mathbf{k} = \frac{1}{2}\, tr([\mathbf{S}]\Psi) = [k_0, k_1, k_2, k_3]^T \tag{2.33}$$

where $tr[\mathbf{S}]$ is the trace of [**S**], sum of the diagonal elements, Ψ is a basis formed by a four $[2 \times 2]$ hermitian complex matrices [121]. In Eq. (2.33) two basis are principally used. The first one is the *Borgeaud basis* [122]:

$$\Psi_B = \left\{ 2\begin{bmatrix} 1 & 0 \\ 0 & 0 \end{bmatrix}, 2\begin{bmatrix} 0 & 1 \\ 0 & 0 \end{bmatrix}, 2\begin{bmatrix} 0 & 0 \\ 1 & 0 \end{bmatrix}, 2\begin{bmatrix} 0 & 0 \\ 0 & 1 \end{bmatrix} \right\} \tag{2.34}$$

to which corresponds the complex vector $\mathbf{k}_B$:

$$\mathbf{k}_B = [S_{hh}, S_{hv}, S_{vh}, S_{vv}]^T \tag{2.35}$$

The second basis, manly used, is named *Pauli basis* and is composed by the following *Pauli's spin matrices* [121]:

$$\Psi_P = \left\{ \sqrt{2}\begin{bmatrix} 1 & 0 \\ 0 & 1 \end{bmatrix}, \sqrt{2}\begin{bmatrix} 1 & 0 \\ 0 & -1 \end{bmatrix}, \sqrt{2}\begin{bmatrix} 0 & 1 \\ 1 & 0 \end{bmatrix}, \sqrt{2}\begin{bmatrix} 0 & -j \\ j & 0 \end{bmatrix} \right\} \tag{2.36}$$

The complex vector connected to Pauli's basis is the following:

$$\mathbf{k}_P = \frac{1}{\sqrt{2}}[S_{hh} + S_{vv}, S_{hh} - S_{vv}, S_{hv} + S_{vh}, j(S_{vh} - S_{hv})]^T \tag{2.37}$$

Constant 2 in Eq. (2.34), like as $\sqrt{2}$ in Eq. (2.36), are used because the module of the scattering vector $\mathbf{k}$ must be proportional to the backscattering power; the following equation must be satisfied:

$$|\mathbf{k}|^2 = \mathbf{k}_P^{*T} \cdot \mathbf{k}_P = \mathbf{k}_B^{*T} \cdot \mathbf{k}_B = (|S_{hh}|^2 + |S_{hv}|^2 + |S_{vh}|^2 + |S_{vv}|^2) = span[\mathbf{S}] \tag{2.38}$$

independently from the choice of the basis.

2.1.12 Pauli Decomposition

One of the first approach to the analysis of polarimetric data is the [**S**] coherent matrix decomposition. The basic idea is to express the matrix of Eq. (2.25) like a linear combination of elementary scattering matrices, strictly related to well known scattering mechanisms. Pauli decomposition, like as the Krogager and the Cameron decompositions, can be only employed to characterize coherent scatterers. A resolution cell in a SAR images is formed by the coherent addition of the responses of the elementary contained scatterers. In those cases in which there is no a dominant scatterer, the statistic of the response is given by the complex Gaussian scattering model, giving rise to the so-called speckle. Nevertheless, the resolution cell can present a point target, which dominates the response of the resolution cell. In this case, the scattering response is due to the coherent combination of two components:

- the dominant scatterer;
- the coherent combination due to the clutter, which is given by the complex Gaussian scattering statistics model.

The statistics of the resulting combination receives the name of Rician model. In Fig. 2.8 the response with and without the presence of a point scatterer within the resolution cell are compared.

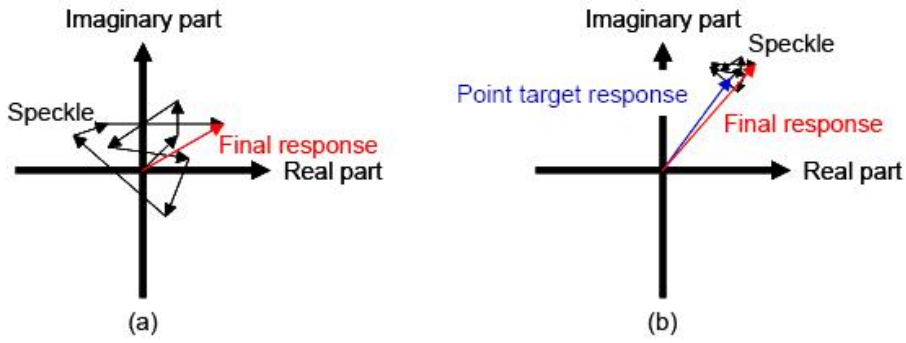

Figure 2.8: Coherent response of a given resolution cell (a) without a dominant scatterer, (b) with a dominant scatterer [69].

Eq. (2.36), that represent *Pauli Basis*, can be used also for the backscattering signal decomposition, because the matrices that compose the basis can be referred to deterministic scattering mechanisms. [**S**] matrix can be express as a linear combination of the backscattering mechanism described by Pauli's matrices, weighed by appropriate coefficients. The following formula represents Pauli decomposition applied to a scattering matrix [**S**]:

$$[\mathbf{S}] = \begin{bmatrix} a+b & c-jd \\ c+jd & a-b \end{bmatrix} = a \begin{bmatrix} 1 & 0 \\ 0 & 0 \end{bmatrix} + b \begin{bmatrix} 1 & 0 \\ 0 & -1 \end{bmatrix} + c \begin{bmatrix} 0 & 1 \\ 1 & 0 \end{bmatrix} + d \begin{bmatrix} 0 & -j \\ j & 0 \end{bmatrix} \tag{2.39}$$

where a, b, c and d are proportional to the complex components of the scattering vector $\mathbf{k}_P$ (Eq. (2.37)). The fourth matrix in Eq. 2.39 can be not considered in backscattering processes because of the reciprocity theorem (Sect. 2.1.13). The other three matrices identify the scattering processes showed in Tab. 2.1.

In general, coherent decomposition theories are exposed to problems due to speckle, so they are not appropriate when applied to radar remote sensing of natural random targets like vegetation. Nonetheless, they are still suitable when the scene is dominated by a single scattering element,

Pauli's Matrix	*Type of Scattering*	*Interpretation*
$\begin{bmatrix} 1 & 0 \\ 0 & 1 \end{bmatrix}$	odd-bounce	plane, sphere
$\begin{bmatrix} 1 & 0 \\ 0 & -1 \end{bmatrix}$	even-bounce	dihedral
$\begin{bmatrix} 0 & 1 \\ 1 & 0 \end{bmatrix}$	$\pi/4$ even-bounce	$\pi/4$ dihedral

Table 2.1: Pauli's matrices and their interpretation in the $\{\mathbf{e}_h, \mathbf{e}_v\}$ basis.

or a few of them and, under certain specific conditions, a radar with high resolution is employed [58].

2.1.13 Non deterministic Scatterers

In the previous section deterministic scatterers have been analyzed that can be completely defined by the scattering matrix [**S**] or by the complex scattering vector **k**. The concept of deterministic scatterer is not appropriate for radar remote sensing analysis, because the resolution cell is bigger of the used wavelength, for this reason contains more than a single scattering center, each one represented by a scattering matrix [**S**]. The scattering matrix connected to a determinate resolution cell consists in the sum of all the [**S**] matrices associated to the distribute scattering centers contained in the cell itself. For a complete study of the effects connected to non deterministic scatterers it is useful to introduce the concepts of cohovariance and coherence matrices ([42], [123], [124]). Polarimetric matrix of cohovariance can be calculted by means of the complex scattering vector $\mathbf{k}_B$ (Eq. (2.35)) [123]:

$$[\mathbf{C}]_{4\times4} = \langle \mathbf{k}_B \mathbf{k}_B^{\dagger} \rangle = \begin{bmatrix} \langle |S_{hh}|^2 \rangle & \langle S_{hh} S_{hv}^* \rangle & \langle S_{hh} S_{vh}^* \rangle & \langle S_{hh} S_{vv}^* \rangle \\ \langle S_{hv} S_{hh}^* \rangle & \langle |S_{hv}|^2 \rangle & \langle S_{hv} S_{vh}^* \rangle & \langle S_{hv} S_{vv}^* \rangle \\ \langle S_{vh} S_{hh}^* \rangle & \langle S_{vh} S_{hv}^* \rangle & \langle |S_{vh}|^2 \rangle & \langle S_{vh} S_{vv}^* \rangle \\ \langle S_{vv} S_{hh}^* \rangle & \langle S_{vv} S_{hv}^* \rangle & \langle S_{vv} S_{vh}^* \rangle & \langle |S_{vv}|^2 \rangle \end{bmatrix} \tag{2.40}$$

where $\mathbf{k}_B^{\dagger}$ is the transpose conjugate of $\mathbf{k}_B$ and $\langle \ldots \rangle$ is the mean of the random predominant scatterers. In the same manner, if the complex scattering vector $\mathbf{k}_P$ is considered, polarimetric coherence matrix $[\mathbf{T}]_{4\times4}$ can be calculated [123]:

$$[\mathbf{T}]_{4\times4} = \langle \mathbf{k}_P \mathbf{k}_P^{\dagger} \rangle \tag{2.41}$$

Cohoerence and covariance matrices have the same real positive eigenvalues but different eigenvectors [107]. It is easier to analyze scattering mechanisms if cohoerence matrix is used. If Eq. (2.36) is considered, stating the properties of the reciprocity theorem $S_{hv} = S_{vh} = S_X$, the fourth term of the scattering vector $\mathbf{k}_P$ is null and the following equation can be obtained:

$$\mathbf{k}_{P3} = \frac{1}{\sqrt{2}}[S_{hh} + S_{vv}, S_{hh} - S_{vv}, 2S_x]^T \tag{2.42}$$

Without any loss of information, a three-dimensional space can be taken in account instead of a four-dimensional space. Taking advantage of $\mathbf{k}_{P3}$ a new polarimetric coherence matrix $[3 \times 3]$ can be defined:

$$[\mathbf{T}]_{3\times3} = \langle \mathbf{k}_{P3} \mathbf{k}_{P3}^{\dagger} \rangle = \frac{1}{2} \begin{bmatrix} \langle |A|^2 \rangle & \langle AB^* \rangle & \langle AC^* \rangle \\ \langle A^*B \rangle & \langle |B|^2 \rangle & \langle BC^* \rangle \\ \langle A^*C \rangle & \langle B^*C \rangle & \langle |C|^2 \rangle \end{bmatrix} \; where \begin{cases} A = S_{hh} + S_{vv} \\ B = S_{hh} - S_{vv} \\ C = 2S_x \end{cases} \tag{2.43}$$

In Eq. (2.43) all information about variance and correlation among the complex elements of [**S**] are contained.

2.1.14 Eigenvector-Eigenvalue based and H/A/α–Wishart decompositions

The eigenvector-eigenvalue based decomposition is based on the eigen–decomposition of the coherency matrix $[\mathbf{T}]_{3\times3}$ (Eq. (2.43)). According to the eigen–decomposition theorem, the $[3 \times 3]$ Hermitian matrix $[\mathbf{T}]_{3\times3}$ can be decomposed as follows:

$$[\mathbf{T}]_{3\times3} = [\mathbf{U}]_{3\times3}[\Lambda]_{3\times3}[\mathbf{U}]_{3\times3}^{-1} \tag{2.44}$$

The $[3 \times 3]$, real, diagonal matrix $[\Lambda]_{3\times3}$ contains the eigenvalues of $[\mathbf{T}]_{3\times3}$:

$$[\Lambda]_{3\times3} = \begin{bmatrix} \lambda_1 & 0 & 0 \\ 0 & \lambda_2 & 0 \\ 0 & 0 & \lambda_3 \end{bmatrix} \tag{2.45}$$

where $\infty > \lambda_1 > \lambda_2 > \lambda_3 > 0$.

The $[3 \times 3]$ unitary matrix $[\mathbf{U}]_{3\times3}$ contains the eigenvectors $\mathbf{u}_i$, for i=1,2,3, of $[\mathbf{T}]_{3\times3}$:

$$[\mathbf{U}]_{3\times3} = [\mathbf{u}_1 \;\; \mathbf{u}_2 \;\; \mathbf{u}_3] \tag{2.46}$$

The eigenvectors $\mathbf{u}_i$, for i=1,2,3, of $[\mathbf{T}]_{3\times3}$ can be formulated as follows:

$$[\mathbf{U}]_{3\times3} = \left[\cos\alpha_i \;\; \sin\alpha_i \cos\beta_i e^{j\delta_i} \;\; \sin\alpha_i \cos\beta_i e^{j\gamma_i}\right] \tag{2.47}$$

Considering Eq. (2.45) and Eq. (2.46), the eigen–decomposition of $[\boldsymbol{T}]_{3\times3}$ (Eq. (2.44)) can be written as follows:

$$[\boldsymbol{T}]_{3\times3} = \sum_{3}^{j=1} \lambda_i \boldsymbol{u}_i \boldsymbol{u}_i^{*T} \tag{2.48}$$

where the symbol ^{*T} stands for complex conjugate. As Eq. (2.48) shows, the rank 3 matrix $[\mathbf{T}]_{3\times3}$ can be decomposed as the combination of three rank 1 coherency matrices formed as:

$$[\boldsymbol{T}]_{3\times3_i} = \boldsymbol{u}_i \boldsymbol{u}_i^{*T} \tag{2.49}$$

which can be related to the pure scattering mechanisms given in Eq. (2.47). The eigenvalues (Eq. (2.45)) and the eigenvectors (Eq. (2.46)) are considered as the primary parameters of the eigen–decomposition of $[\mathbf{T}]_{3\times3}$. In order to simplify the analysis of the physical information provided by this eigen–decomposition, three secondary parameters are defined as a function of the eigenvalues and the eigenvectors of $[\mathbf{T}]_{3\times3}$:

- Entropy:

$$H = -\sum_{i=1}^{3} p_i \log_3(p_i); \;\; where \;\; (p_i) = \frac{\lambda_i}{\sum_{k=1}^{3} \lambda_k} \tag{2.50}$$

where p_i, also called the probability of the eigenvalue λ_i, represents the relative importance of this eigenvalue respect to the total scattered power, stating:

$$SPAN = |S_{hh}|^2 + |S_{vv}|^2 + 2\,|S_{hv}|^2 = \sum_{k=1}^{3} \lambda_k \tag{2.51}$$

- Anisotropy:

$$A = \frac{\lambda_2 - \lambda_3}{\lambda_2 + \lambda_3} \tag{2.52}$$

- Mean Alpha angle:

$$\alpha = \sum_{i=1}^{3} p_i \alpha_i \tag{2.53}$$

The eigen–decomposition of the coherency matrix is also referred as the H/A/α decomposition [11]. The interpretation of the information provided by the eigen–decomposition of the coherency matrix must be performed in terms of the eigenvalues and eigenvectors of the decomposition or in terms of H/A/α. Nevertheless, both interpretations have to be considered as complementary. The interpretation of the scattering mechanisms given by the eigenvectors of the decomposition, $\mathbf{u}_i$, for i=1,2,3 ((Eq. 2.47)), is performed by means of a mean dominant mechanism which can be defined as follows:

$$\mathbf{u}_0 = \sqrt{\boldsymbol{\lambda}} \left[\cos \boldsymbol{\alpha} \quad \sin \boldsymbol{\alpha} \cos \boldsymbol{\beta} e^{j\boldsymbol{\delta}} \quad \sin \boldsymbol{\alpha} \cos \boldsymbol{\beta} e^{j\boldsymbol{\gamma}} \right]^T \tag{2.54}$$

where the remaining average angles are defined in the same way as α:

$$\beta = \sum_{i=1}^{3} p_i \beta_i; \quad \delta = \sum_{i=1}^{3} p_i \delta_i; \quad \gamma = \sum_{i=1}^{3} p_i \gamma_i \tag{2.55}$$

The mean magnitude of the mechanism is obtained as:

$$\lambda = \sum_{i=1}^{3} p_i \lambda_i \tag{2.56}$$

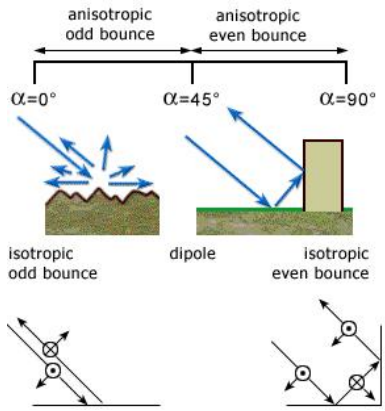

Figure 2.9: Interpretations of α angle [69].

The study of the mechanism given in Eq. (2.54) is mainly performed through the interpretation of the mean alpha angle, since its values can be easily related with the physics behind the scattering process. The next list reports the interpretations of α:

- $\alpha \to 0$: the scattering corresponds to single-bounce scattering produced by a rough surface;
- $\alpha \to \pi/4$: the scattering mechanism corresponds to volume scattering;
- $\alpha \to \pi/2$: the scattering mechanism is due to double-bounce scattering.

The second part in the interpretation of the eigen-decomposition is performed by studying the value of the eigenvalues of the decomposition. A given eigenvalue corresponds to the associated scattered power to the corresponding eigenvector. Consequently, the value of the eigenvalue gives the importance of the corresponding eigenvector or scattering mechanism. The ensemble of scattering mechanisms is studied by means of the entropy H and the anisotropy A. The entropy H determines the degree of randomness of the scattering process, which can be also interpreted as the degree of statistical disorder. In this way:

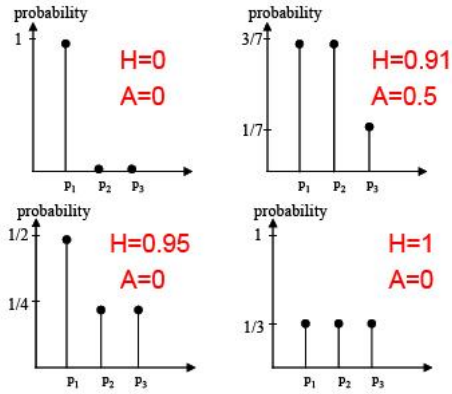

Figure 2.10: Entropy (H) and Anisotropy (A) values for four different configurations of the eigenvalues [69].

- $H \to 0$:

$$\lambda_1 = SPAN, \;\; \lambda_2 = 0, \;\; \lambda_3 = 0 \tag{2.57}$$

Consequently, the scattering matrix $[\mathbf{T}]_{3\times3}$ presents rank 1 and the scattering process corresponds to a pure target.

- $H \to 1$:

$$\lambda_1 = SPAN/3, \;\; \lambda_2 = SPAN/3, \;\; \lambda_3 = SPAN/3 \tag{2.58}$$

In this situation, the scattering matrix $[\mathbf{T}]_{3\times3}$ presents rank 3, that is, the scattering process is due to the combination of three pure targets. Consequently, $[\mathbf{T}]_{3\times3}$ corresponds to the response of a distributed target.

- $0 < H < 1$: In this case, the final scattering mechanism given by $[\mathbf{T}]_{3\times3}$ results from the combination of the three pure targets given by $\mathbf{u}_i$, for i=1,2,3, but weighted by the corresponding eigenvalue.

In Fig. 2.10 four different configurations of the eigenvalues and the corresponding entropy values are showed. The anisotropy A, Eq. (2.52), is

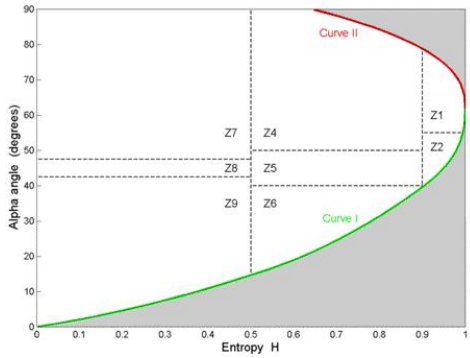

Figure 2.11: H/α plane [69].

a parameter complementary to the entropy. The anisotropy measures the relative importance of the second and the third eigenvalues of the eigen–decomposition. From a practical point of view, the anisotropy can be employed as a source of discrimination only when $H > 0.7$. The reason is that for lower entropies, the second and third eigenvalues are highly affected by noise. Consequently, the anisotropy is also very noisy. According to [11], a H/α and H/A/α planes can be developed (H/A/α plane corresponds to a double H/α plane; one for $A < 0.5$ and the other for $A > 0.5$). Each plane can be subdivided in different zones according to the values of H/α or H/A/α. For each zone a predetermined class is assigned. In order to perform H/α or H/A/α classification, for each pixel of the input polarimetric image, the two/three values of H, α or H, A, α must be calculated. In this way each pixel can be associated with one zone in the H/α or H/A/α plane.

The classes interpretation showed in Fig. 2.11 is as follows:

- class Z1: Double bounce scattering in a high entropy environment;
- class Z2: Multiple scattering in a high entropy environment (e.g. forest canopy);
- class Z3: Surface scattering in a high entropy environment (not a feasible region in H/α plane);

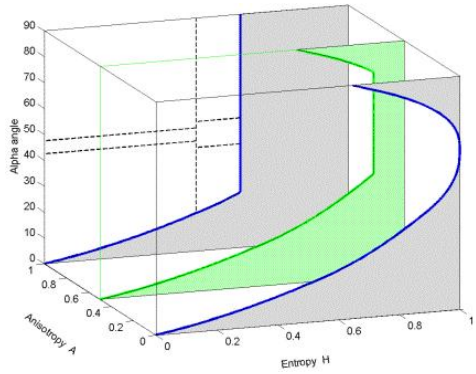

Figure 2.12: H/A/α plane [69].

- class Z4: Medium entropy multiple scattering;
- class Z5: Medium entropy vegetation (dipole) scattering;
- class Z6: Medium entropy surface scattering;
- class Z7: Low entropy multiple scattering (double or even bounce scattering);
- class Z8: Low entropy dipole scattering (strongly correlated mechanisms with a large imbalance in amplitude between HH and VV);
- class Z9: Low entropy surface scattering (e.g. Bragg scatter and rough surfaces).

The H/A/α–Wishart decompositions can be seen as an improvement of the H/A/α classification.

In 1994, J.S. Lee et al. [125] developed a supervised algorithm based on the complex Wishart distribution for the polarimetric covariance matrix. This algorithm is statistically optimal in that it maximizes the probability density function of pixels' covariance matrices. However, as for all supervised methods, training sets have to be selected in advance. These training sets, require from the user an *a–priori* knowledge of the test–site.

In 1999, J.S. Lee et al. [13] proposed an unsupervised classification method that uses the two-dimensional H/α classification plane to initially classify the polarimetric SAR image. The initial classification map defines training sets for classification based on the Wishart distribution. The classified results are then used as training sets for a new iteration using the Wishart method. The classification procedure stops when a termination criterion (maximum number of pixels that switch class, maximum number of iterations or both), defined by the user, is met. With this method significant improvement in each iteration has been observed. In order to further improve the capability to distinguish between different classes, the combined Wishart classifier was extended and complemented with the introduction of the anisotropy (A) information. The H/A/α–Wishart algorithm is nowadays one of the most widely used for classification of polarimetric data. It was mandatory to take it into account in order to test the algorithms developed in this Thesis. In the following chapters will refer to this algorithm with a H/A/α–W label.

2.1.15 Polarimetric classification preserving polarimetric scattering characteristics

The H/α plane is divided into eight zones and eight classes. The physical scattering characteristics associated with each zone provide information for terrain type assignment. The deficiency of this approach is that the classification result lacks details, because of the preset zone boundaries in the H and α plane. Clusters may fall on the boundaries and more than one cluster may be enclosed in a zone [14]. A combined use of physical scattering characteristics and statistical properties for terrain classification is desirable. That kind of algorithm has been proposed by Lee [13], which applied the Cloude and Pottier decomposition scheme for initial classification, followed by iterated refinement using the complex Wishart classifier (H/A/α–W, Sect. (2.1.14)). But, in both algorithms, the final classification can be substantially different from initial classified results, and pixels of different scattering mechanisms could be mixed together, because the Wishart iteration is based only on the statistical characteristics of each pixel. Thus, the physical

scattering characteristics are ignored for pixel reassignment during iterations. In addition, Lee, Ainsworth, Grunes and Du in a series of recent papers ([13], [62], [126], [127]), have demonstrated that the Cloude and Pottier "*Unsupervised POL-SAR Image Feature H/α Polarimetric Classification scheme*" is highly sensitive to image speckle deterioration. In this case, in fact, the entropy H (Eq. (2.50)) may increase and the number of distinguishable classes identifiable from polarimetric observations is reduced. As shown in Fig. 2.11, the feasible region of the H/α classification plane is rapidly shrinking for high values of entropy ($H = 0.9$), where α parameter reaches the limited value of 60^0. For this reason the use of a robust polarimetric speckle filter is mandatory [13].

Unlike previous algorithms that classify pixels statistically and ignore their scattering characteristics, the new Lee's approach [14] not only uses a statistical classifier, but also preserves the purity of dominant polarimetric scattering properties for all pixels in a class. This algorithm uses a combination of a scattering models based decomposition developed by Freeman and Durden and the maximum likelihood classifier based on the complex Wishart distribution. The first step is to apply the Freeman and Durden decomposition to divide pixels into three scattering categories: surface scattering, volume scattering and double bounce scattering. To preserve the purity of scattering characteristics, pixels in a scattering category are restricted to be classified with other pixels in the same scattering category. A initialization scheme is also devised to initially merge clusters from many small clusters in each scattering category by applying a merge criterion developed based on the Wishart distance measure. Then the iterative Wishart classifier is applied. The stability in convergence of this algorithm is much superior to that of the previous algorithm using the H/A/α–W classifier. The entire unsupervised classification procedure is as follows:

- **Initial Clustering**

    1. Filtering of the polarimetric SAR data using a filter [128] specifically designed for polarimetric SAR images, if the original data do not have sufficient averaging in the number of looks. All elements of the $[3 \times 3]$ covariance or coherence matrix should be

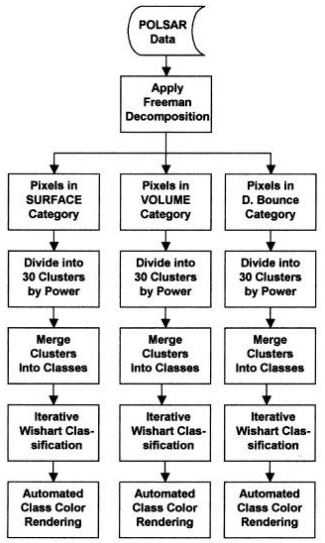

Figure 2.13: Flowchart of the algorithm [69].

filtered simultaneously to reduce speckle and retain resolution as much as possible. It has been shown that speckle filtering improves clustering. However, excessive filtering would reduce spatial resolution.

2. Decompose each pixel by Freeman and Durden decomposition, and compute P_{DB}, P_V and P_S (P_X, pixels belonging X class). Label each pixel by the dominant scattering mechanism as one of three scattering categories: Double Bounce (DB), Volume (V) and Surface (S).
3. Divide the pixels of each category into 30 or more small clusters with approximately equal number of pixels.

- **Cluster Merging**

1. The averaged covariance matrix for each cluster is computed.

2. Within each category, the initial clusters are merged based on the between-cluster Wishart distance. Two clusters are merged if they have the shortest distance and are in the same scattering category.
3. Merge the initial clusters to a desirable number of classes, N_d, required in the final classification. To prevent a class from growing too large and overwhelming the other classes, a limitation to the size of classes could respect next rule:

$$N_{max} = 2N/N_d \tag{2.59}$$

where N the total number of pixels in the image. In addition, small clusters are merged first, and only clusters in the same scattering category can be merged to preserve the purity of scattering characteristics. In terrain classification, the number of pixels dominated by double bounce is much smaller than those with surface and volume scattering. For better separation of pixels in the double bounce category with smaller number of pixels, merging must be limited to, at least, three final clusters (classes) for each scattering category.

- **Wishart Classification**

1. Averaged covariance matrices must be computed starting from the N_d classes and used as class centers. All pixels are reclassified based on their Wishart distance measure from class centers. Pixels labeled as "DB", "V" or "S" can only be assigned to the classes with the same label. This ensures the classes are homogeneous in scattering characteristics. For example, a double bounce dominated pixel will not be assigned to a surface scattering class even if the Wishart distance is the shortest.
2. Wishart classifier is iteratively applied for 2 to 4 iterations with the category restriction for better convergence.

- **Automated Color Rendering**

The classes are color-coded according to their scattering label. After

the final classification, the color selection for each class is automatically assigned: blue colors for the surface scattering classes, green colors for volume scattering classes, and red colors for double bounce classes. In the surface scattering classes, the class with highest power will be assigned color white to designate the near specular scattering class.

The previous algorithm is based on the Freeman–Durden scattering model decomposition [7]. This limits the applicability of this algorithm in discriminating man–made targets, rough surface, forest species and crop types [14]. Limitation in applications can be summarized as follow:

- *Roll invariance.*
  The Freeman and Durden decomposition was developed under the assumption of reflection symmetry that makes its results not roll invariant. Variations of targets orientations with respect to the radar look direction may cause misclassification. Buildings not aligned facing the radar look direction do not induce double-bounce returns and they are categorized as volume scattering in the Freeman–Durden decomposition because of higher HV returns.

- *Rough Surface Misclassified as Volume Scattering.*
  Freeman–Durden decomposition has intrinsic difficulty separating very rough surface from volume scatterers. Rough surface scattering by non vegetated surface can cause significant depolarization and produces high cross–polar levels that can appear as volume scattering in the Freeman and Durden decomposition, especially, at higher radar frequencies, such as C-band and X-band. Consequently, a rough surface will be classified as a volume class, and could be misinterpreted as vegetation.

- *Vegetated Areas Misclassified as Surface Scattering.*
  Some vegetated areas can appear as surface scatterers in the Freeman-Durden decomposition. Freeman and Durden assume randomly distributed thin cylindrical scatterers for the volume scattering. This model may work well for coniferous forest, but, for other forest species,

the model of randomly distributed oblate spheroids is more appropriate, in which cases, surface scattering may become dominate.

Some techniques can be applied to reduce previous limitations. For example, to properly classify buildings, interferometric data may be required to separate buildings from vegetation. Buildings tend to have much higher interferometric coherence than vegetation. The described algorithm is considered, according to many researchers, the best method for the classification of polarimetric SAR images. Therefore, this algorithm has been considered, together with the H/A/α–W algorithm, to test the algorithms developed in this Thesis.

2.2 Self-organizing Maps background

2.2.1 Introduction

There are two different purposes justifying the developing of artificial intelligence. The original one is an attempt to describe biophysical phenomena that take place in real biological neurons, whereby it may be expected that some primitives or basic elements of information processing by the brain could be isolated and identified. Another one is a direct attempt to develop new devices based on heuristically conceived, although biologically inspired simple components such as threshold-logic units or formal neurons [23]. Human brain is being studied by many researchers, in order to develop algorithms able to reproduce its computational and adaptive characteristics. The performance of that organ are surprising: if brain is intended as computational machine, it is able, in a few steps, to identify and recognize any danger in order to make decisions that may be vital. It is possible to note that the processing speed - number of operations per second - is not the decisive feature in the explanation of properties human brain; computers perform a number of operations per second that are significantly higher. The secret of the brain computing ability is that the in central nervous system the synapses exploit neural growth factor for cable in configurations that make the organ best suited to maintaining its balance towards the environment,

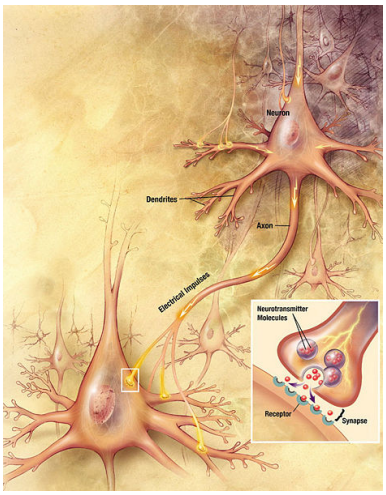

Figure 2.14: Chemical synapse scheme.

finding internal capabilities to make this reconfiguration. The learning ability of the human brain it is difficult to reproduce by computer, given its complexity that is characterized by an interaction of organic elements whose number is estimated to 10^{11} neurons and 10^{15} synaptic connections. Two different approaches have been implemented in order to obtain a learning neural network based algorithm. In the first approach a set of examples (training set) are provided to the net under human supervision. This is the case of Multi-Layer Perceptron technique. The distinctive feature of Self-organizing Maps [23], also named Kohonen's neural networks, is the ability to learn without human supervision. This reason makes SOM a important tool for analyzing complex problems, like as classification of SAR data for remote sensing purposes.

2.2.2 Neural Networks Model

An artificial neural network may be viewed as a mathematical model composed of non-linear computational elements, named neurons, operating in

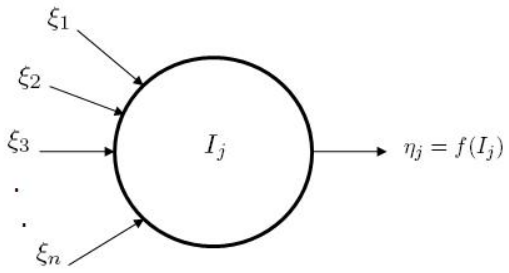

Figure 2.15: Statistic nonlinear generic model for a neuron. Here $f(.)$ is some monotonic function that has low and high saturation limit.

parallel and connected by links characterized by different weights [129]. NNs models are mainly specifed by:

- neuron structure;
- training or learning rules;
- net topology;

Up to this time, most neural network models, especially the feed-forward network have assumed neurons similar to those introduced over 40 years ago, named multiple-input, single-output static elements that form a weighted sum of input signal values ξ_i called I_j, and then amplify I_j in a non linear circuit into η_j. A single neuron structure is shown in Fig. 2.15.

Usually there are three different way to define the training or learning rules:

- Supervised Delta Role;
- Unsupervised Hebbian model;
- Competitive, both supervised and unsupervised.

In order to understand the difference between the previous methods Fig. 2.16 must be considered. In figure it shown a single processing unit of a

generic net that receives inputs from other neurons or directly from the environment (stimuli). On the connections are present synaptic weights that refer to the strength of the connection. All that signals are fed, together with internal threshold of the neuron, inside the net_j. The output is calculated by means of the activation function $g(net_j)$. The neuron is characterized, therefore, by weight vector and the difference in the learning rules exclusively regards the way how the weights are updated. If Hebb rule is used, the variation of the weights directly depends form the output of the neuron:

$$\Delta w_{ij} = \eta x_i y_j \tag{2.60}$$

otherwise, of Delta Rule is considered, the learning rule is based in the output error δ_j connected to a specified input pattern:

$$\Delta w_{ij} = \eta x_i \delta_j \tag{2.61}$$

In case of competitive learning method, the upgrading of the weights depends on the neuron that responds better to stimulus. Kohonen networks (SOM) are unsupervised and competitive. That nets try to imitate nervous system, for this reason it is important to understand the learning process of the brain. For this purpose, a geometric approach can be used. Both stimulus and output are characterized by a indefinite number of components, that, if represented in a n–dimensional space, correspond to a point. The learning process is the the geometric process that transforms the stimulus (input), represented by a point in the inputs–space, in the output, represented by a point in the outputs–space. The dimension of the outputs space is usually smaller respect the dimension of the inputs space, because the stimulus contains information able to active many simultaneous processes. For this reason this geometric transformation consists, at least in a latent way, in a reduction of redundancy, in other words in a compression of input data, that is another way to describe the classification of satellite images. Both in the input and in the output space, typical regions are created where the information are represented. The mechanisms that controls the information transferring must identify this regions and ensure the connection. The operation that consists in the data grouping, in order to create the regions,

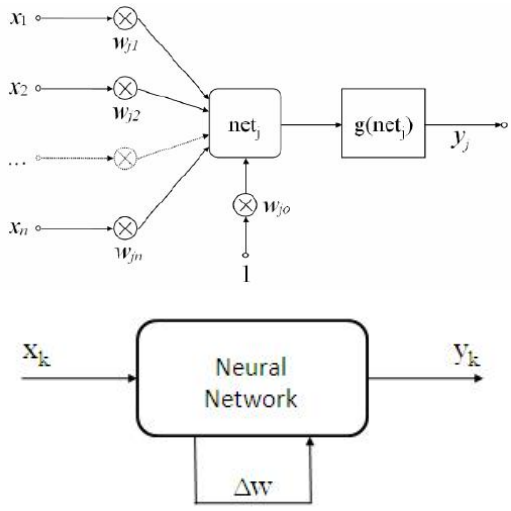

Figure 2.16: Reference Neuron Model (*up*) and the unsupervised learning schema (*down*).

can be identified as the acquisition of the experience. Kohonen's networks are able to preform the operations of grouping and reduction of redundancy in a unsupervised way.

2.2.3 Mathematical Model

It is estimated that the human brain is composed of 10^{11} neurons and each neuron can create from 10^3 to 10^4 synaptic connections. Each area of the brain is dedicated to the decodification of particular stimuli. When an external input is received, neurons are activated in groups, according to their specialization and the type of input. That phenomena can be interpreted as "bubble" of activity, due to a collective activity of specialized neurons. The bubble can be viewed as an round area where there is "activity" surrounded by a flat inactive surface. The evolution of that phenomena can be modeled by means of non-linear differential equations. In particular the model of leaky integrator can be used. In mathematics, a leaky integrator equation is a specific differential equation, used to describe a component or system that takes an input but gradually leaks a small amount of input over time. The equation is of the form:

$$dx/dt = C - Ax \tag{2.62}$$

where C is the input and A is the rate of the "leak".

Referring to Fig. 2.15 and Eq. (2.62), the equation that describe the activity of the j_{th} neuron is [23]:

$$d\eta_j/dt = I_j - \gamma(\eta_j), \eta_j \geq 0 \tag{2.63}$$

The neuron, then, acts like a leaky integrator, and the leakage effect in this model is nonlinear. In a similar way as in many other simple models, considering the synaptic weights (Fig. 2.18), the input activation I_j may be approximated by:

$$I_i = \sum_{j=1}^{n} \mu_{ij} \xi j \tag{2.64}$$

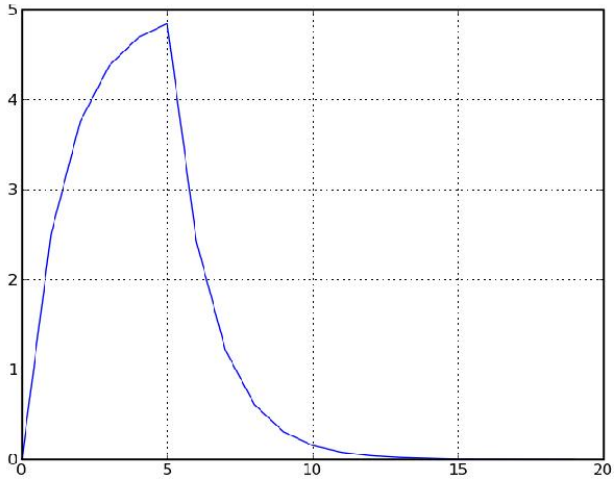

Figure 2.17: A graph of a leaky integrator.

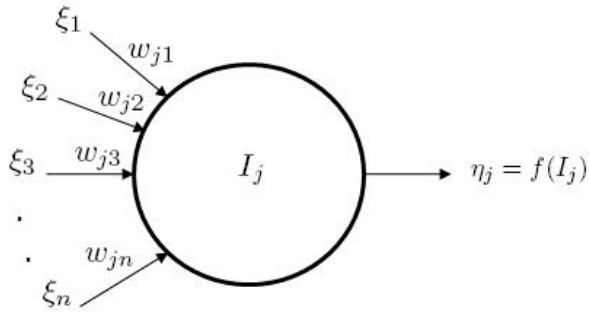

Figure 2.18: Nonlinear dynamic model for a neuron.

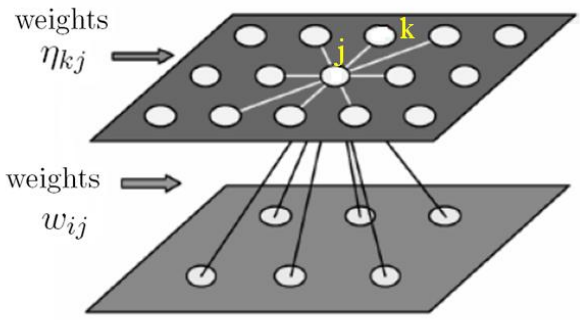

Figure 2.19: Kohonen Neural Network.

considering Eq. (2.63) together with Eq. (2.64) and two layers network (Fig. 2.19):

$$d\eta_j/dt = \sum_{i=1}^{n} w_{ji}\xi_i - \gamma(\eta_j) + \sum_{k\neq j}^{n} \mu_{kj}\eta_{kj} \tag{2.65}$$

where

- η_j is the activity of j_{th} neuron;
- ξ_i is the i_{th} component of the input and n is the total number of inputs;
- w_{ji} is the weight of the connection between the j_{th} neuron and the i_{th} input (synapse);
- γ is a term that considers the leaks of the process;
- η_{kj} is the connection between j_{th} and k_{th} neurons.

It can be shown that Eq. (2.65), if all neurons that constitute the net are considered, is able to model the bubble model. With this model the

information contained in the inputs are transferred to the synapses and their variation is regulate by the following differential equation:

$$dw_{ji}/dt = \alpha\eta_j\xi_i - \beta(\eta_j)w_{ji} \tag{2.66}$$

where α check the velocity of learning and $\beta(\eta_j)$ the "forgetfulness". It is possible to note that the temporal evolution of synapses depends on the activity of the neurons and relative connection. That is different depending on whether the neuron is in the bubble or outside the bubble, two cases may be distinguished:

- Neuron inside the bubble. In this case the neuron is in the maximum of the activity ($\eta_j \approx 1$). If the other terms in Eq. (2.66) are normalized in order to obtain $\alpha\eta_j \approx \beta(\eta_j)$:

  $$dw_{ji}/dt = \alpha(\xi_i - w_{ji}) \tag{2.67}$$

  where it is possible to note that the synapse changes tying to balance the corresponding input;

- Neuron outside the bubble. This neurons have a negligible activity, for this reason $\eta_j \approx 0$. Eq. (2.66) become:

  $$dw_{ji}/dt = 0 \tag{2.68}$$

  synapses of this neurons are not modified.

2.2.4 SOM Structure

The Kohonen neural network consists in a series of inputs and in a n-dimensional grid of neurons. Each input is connected to all neurons of the grid: the resulting matrix of weights is used to propagate the inputs of the network to the neurons on the map. An example in monodimensional space it is shwon in Fig. 2.20.

Considering Fig. 2.20 the mathematical formulation that describes the net is:

$$y_j = \sum_{n}^{i=1} w_{ji}x_i \tag{2.69}$$

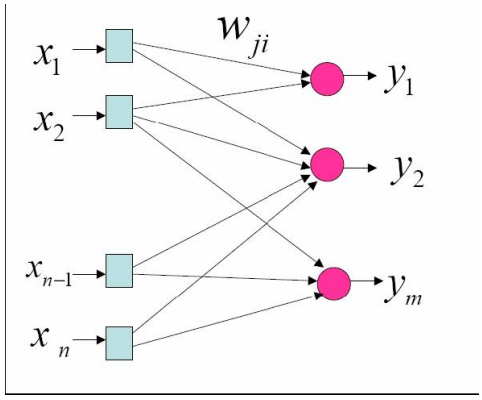

Figure 2.20: Example of a mono-dimensional network, on the left input neurons that are fully connected to the output neurons on the right.

where w_{ji} indicates the weight of the connection between the neuron j_{th} and the input i_{th} and vectors $\mathbf{x}$, $\mathbf{w}$ and $\mathbf{y}$ are defined as:

$$\mathbf{x} = [x_1, x_2, \cdots, x_n]^T \tag{2.70}$$

$$\mathbf{w}_j = [w_{j1}, w_{j2}, \cdots, w_{jn}]^T \tag{2.71}$$

$$\mathbf{y} = [y_1, y_2, \cdots, y_m]^T \tag{2.72}$$

where $j = 1, 2, \cdots, m$ and m is the total number of the neurons in the net.

The phenomenon of the bubble, resulting in the only change of neurons contained in it, is simulated through the introduction of the concept of neighborhood of a neuron. The neuron that wins the competition (winner neuron) is chosen with a strategy that take account of the outputs of all neurons. Normally is selected the neuron that shows the maximum output or the neuron whose vector of weights is closer to the input. In the first case it is necessary to normalize the vectors, in the second case it is not. If the second case is considered, the winner neuron can be mathematically:

$$c = \arg\min_j \{d(x, w_j)\} \tag{2.73}$$

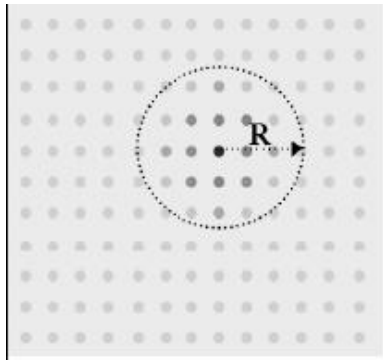

Figure 2.21: Radius of interaction, $R = r_c - r_j$.

If the distance $d(x, w_j)$ is is considered Euclidean, Eq. (2.73) become:

$$c = \arg\min_j \{\|x, w_j\|\} \tag{2.74}$$

The interaction that the winning neuron has with its neighbors is defined according to a *neighborhood function* , which normally takes value between 0 and 1. This interaction determines a modification of the weights dependent on neighborhood function and the response of the neuron. It can be used for this purpose Gauss's function:

$$\lambda_{cj} = e^{-\frac{\left|\mathbf{r}_c - \mathbf{r}_j\right|^2}{2\sigma^2}} \tag{2.75}$$

where $\mathbf{r}_c$ is the position vector of the winning neuron, $\mathbf{r}_j$ is the position vector of the j_{th} neuron of the map and σ is named *proximity parameter*. When the process starts the σ parameter has a high value, thus the area over which the bubble acts is wide. During the learning phase the previous area is gradually decreased so that only the neurons closer to the more activated neuron are affected and it is possible the convergence of the algorithm. The weights of the neurons in the bubble are, therefore, updated according to the following formula:

$$w_j(t+1) = w_j(t) + \eta\lambda_{cj}(x(t) - w_j(t)) \tag{2.76}$$

where η is the *learning rate* and decreases gradually during the learning phase.

2.2.5 Parameters Setting

Different parameters must be defined in order to synthesize a SOM. The parameters are: dimension, learning rate, neighborhood function and training cycles. In the following subsection a description of these parameters will be given.

2.2.5.1 Dimension

SOM networks normally grow in the plane or in space. Three-dimensional configuration does not give a substantial advantage during the elaboration of information and usually causes a complication in the management of the map itself. A bi-dimensional configuration is usually preferred. The number of neurons can change from a few to many. The choice may be influenced by the complexity of the input data.

2.2.5.2 Learning Rate

The choice of the trend of η parameter as a function of the time must follow simple rules: in the early 1000 cycles its value should be ≈ 1 and then decreased until it reaches its minimum value. A possible formulation is:

$$\eta = \eta_{max} \left(\frac{\eta_{min}}{\eta_{max}} \right)^{\frac{t}{t_{max}}} \quad with \quad \begin{cases} \eta_{min} = 0 \\ \eta_{max} = 1 \end{cases} \tag{2.77}$$

2.2.5.3 Neighborhood Function

The type of neighborhood does not have much influence, however, it is important to choose opportunely the parameter σ: if it is too small network could, after the training phase, not be ordered globally. It is possible to avoid this problem by assigning to that variable a value greater than the half of the diameter of the network. During the training cycle, σ must change to

reduce the neighborhood in order to obtain the winning neuron ($\sigma = 0.5$). Neighborhood function can be defined as:

$$\sigma = \sigma_{max} \left(\frac{\sigma_{min}}{\sigma_{max}} \right)^{\frac{t}{t_{max}}} \tag{2.78}$$

where t_{max} is the parameter that represents the training cycles.

2.2.5.4 Training Cycles

The training process is a stochastic process, so the final accuracy depends on the number of steps made in the phase of convergence that must be rather long. A empiric rule for an acceptable accuracy, is to select 500 training cycles for each neuron of the network.

2.2.6 Learning Process

The learning process of a SOM is based on three basic properties:

- **Competition**: every time that an input is fed in the net only the "stronger"neuron is activated and becomes the winner.
- **Cooperation**: the winning neuron is connected to its neighbors, and defines the center of an area in which the input will cause a change the weights of the neurons.
- **Upgrading of synapses**: weight vectors of winner vector and of and its neighbors will be updated according to learning algorithm.

The cycle that defines the learning process of the Kohonen neural networks can then schematized in this way:

1. Selection of basic parameters;
2. Initialization of the weights of the map: random values are chosen, avoiding that the weights of two different synapses are the same;
3. Selection of the input vector in a random or cyclically way;

4. Selection of the winning neuron;
5. Upgrading of the weights of the map;
6. Decreasing of σ and η parameters;
7. Restarting from step 3.

The algorithm ends when σ becomes minor of a predetermined value or when the weights of the map have a stable value. When the learning process ends, after that the synapses are frozen, for each input vector $\mathbf{x}$ SOM assign an output considering the position or the synapses of the winning neuron. The output space is discrete, represented only by n points arranged in a two-dimensional grid. The input-output elaboration performed by Kohonen network has many properties, the most important is the "Organization" of the neurons, form which its name: Self-Organizing Maps. Finally, when the network is used referring to the synapses vector, it implements an vector encoder.

2.2.7 SOM characteristics

After the learning phase, SOM is able to preform several tasks closely related to its characteristics, as described in the following.

2.2.7.1 Codification of input Space

The input $\mathbf{x}$ which is sent to the the neural network is represented by a point in the N-dimensional inputs space. In this area there are characteristics regions of the analyzed context in which is associated the information of the process that is under examination. These regions play an important role in signals elaboration and there are algorithms that try to locate them. One of the most important applications of these algorithms is the encoding, that concerns in the connection of that regions with a particular point, named "centroid", which is the representative value (prototype) of the entire region. The objective of a coder is to minimize the error that is committed replacing the input $\mathbf{x}$ with its prototype , calculated on the entire space and taking

into account the density of probability of **x**. Kohonen's network behave like an encoder. Each neuron is connected to the input and its synapses (weights) represent a point in the input space. To that neuron corresponds also a region in the input space, that is the region of inputs x that make the neuron winner.

Therefore, the network divides the space into regions, each associated with a neuron, with the corresponding centroid coinciding with the vector of its synapses. In order to consider Kohonen network like and encoder, the following steps are required:

1. Elaboration of **x** input;

2. Determination of the winner neuron;

As a result of the vector encoding must be considered the synapses of winner neuron.

2.2.7.2 Organization

The discretized output space of the Kohonen network is characterized by organized topology in the sense that the position of a neuron in the map corresponds to a specific information. Considering a two-dimensional network and input data related on two orthogonal variables named δ and ϵ. It can be shown that after the learning phase neurons on the rectangular grid correspond, if the two orthogonal direction are considered, to the two variables. In that case the grid represents a coordinated plane with abscissa δ and ordinate ϵ. In the case that the variables are more than two, still considering a two-dimensional network, the organization evolves respect the two variables that affect implied more. The final order then appears more disturbed as much as the influence of other secondaries variables. When this property is used, the Kohonen's network appears like a map divided into regions each of which is associated with a particular information.

2.2.7.3 Approximation of data density of probability

The SOM reflects the statistical of input data and tends to recreate their density of probability. With this behavior the net shows a greater sensitivity on the data most recurrent neglecting those rare. In some situations this could be useful, but for classification purposes can be a disadvantage because the aim is to recognize all classes, even those few present in the image.

2.2.8 SOM visualization: The U-matrix

The neural network is interpreted as a set of points in n-dimensional space, with n number of components of the input vector. After the training phase, these points arrange in a organized manner in the map, so can be useful to visualize them. The problem is how to represent a set of multidimensional data in a 2–D space. Is then useful the **U**-matrix visualization method, which is a simple way for display the distances between different neurons of the map. The **U**-matrix construction is quite easy, to each neuron n in the map is associated a value given by the following formula:

$$Umtx(n) = \sum_{m \in NN(n)} d(w(n), w(m)) \tag{2.79}$$

where:

- $d(w(n), w(m))$ refers to the distance operator, used during the training of the net, that acts on the m_{th} and the n_{th} vectors;
- NN(n) defines the set of neurons neighboring with the n_{th};

Then, starting form a SOM having $n \times n$ dimension, when Eq. (2.79) is used it is possible to obtain a $n \times n$ **U**-matrix, as shown in Fig. 2.22.

2.2.9 SOM Clustering

Trained SOM can be seen as a classifier, every time that an input vector is fed in to the net, a neuron is activated and defines the class for the considered input vector, but the problem is that in very large networks the number of

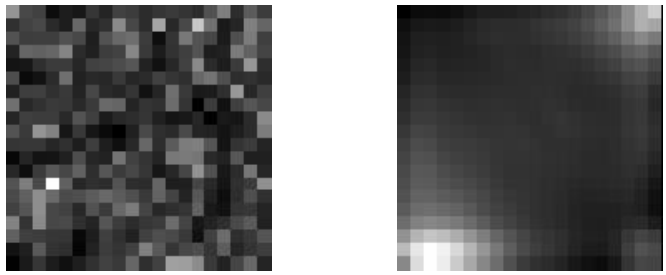

Figure 2.22: **U**-matrix of a SOM $n \times n$ before and after the training phase. It is possible to note, in the figure on the right, the achieved organization of the SOM.

output classes is high. In addition, two or more neighboring neurons are often very close in terms of Euclidean distance, for this reason they may not belong to separate classes. For the previous reason it is important to perform a clustering of the elements of the trained SOM. Considering Fig. 2.22, on the right is shown the SOM after the training. Three brighter areas are visible, which may represent three different clusters. The methods used for this second processing may be different: hierarchical method or divisive (like K-means). Another method is the re-use of the SOM algorithm. In this Thesis two SOMs are used: the neurons of the first bigger trained network are classified (clustered) with smaller second SOM (Sect. 2.2.9.3).

2.2.9.1 Hierarchical approach

The hierarchical methods follow two different strategies: bottom-up and top-down. The steps of the approach are:

1. Initialization: each input is connected to a different class;
2. Analysis of the distance among the clusters;
3. Merging of the nearest clusters;
4. Algorithm repetition from step 2 until only one cluster is obtained.

The process result is a data grouping in order to form a hierarchical tree. The resulting dendogram does not permit a unique data clustering; as shown in Fig. 2.23 there are three different way to perform a 3-clusters grouping.

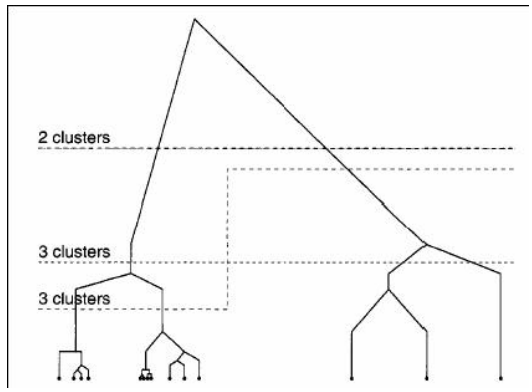

Figure 2.23: Dendogram of 14 points in a 1-D space.

2.2.9.2 K-Means approach

The k-Means based clustering algorithms divide the data in n clusters and try to minimize a defined error function. Usually the number of clusters is previously defined. The algorithm may be summarized as follows:

1. Determination of the number of the clusters;
2. Initialization of the scattering centers;
3. Analysis of data distribution;
4. Analysis and modification in the allocation of scattering centers;
5. If the clusters do not change, there is the convergence of the algorithm and the process ends. Otherwise the algorithm must be repeated from step 3.

The K-means approach is often preferred to the hierarchical, but usually utilizes assumption like as circular shape of the clusters. In addition, the learning process is stochastic and the results may differ among themselves.

2.2.9.3 SOM based re-clustering approach

As described, SOM can be used as classifier or encoder. In the first case, the class is determined by the winner neuron , while in the other case, for each input, it is estimated the winner neuron and its vector of weights is considered for the output. It may be useful to perform a first data encoding and a subsequent classification. The first biggest trained network becomes itself input for another smaller SOM which performs the classification of the encoded data. The algorithm may be summarized as follows:

1. Setting of the parameters related to the first SOM;
2. Initialization of the weights in the first SOM with the input data;
3. Selection of a input vector to fed in the first SOM;
4. Winning neuron determination in the first SOM;
5. Upgrading of the weights of the first SOM;
6. Decreasing of σ and η parameters in the first SOM;
7. Algorithm repetition from step 3 until σ and η of the first SOM reach a value lower of a priori determined threshold;
8. Setting of the parameters related to the second SOM;
9. Initialization of the weights in the second SOM with the vectors of the first SOM;
10. Selection, from the first SOM, of a input vector to fed in the second SOM;
11. Winning neuron determination in the second SOM;

12. Upgrading of the weights of the second SOM;
13. Decreasing of σ and η parameters in the second SOM;
14. Algorithm repetition from step 10 until σ and η of the second SOM reach a value lower of a priori determined threshold;

After the phase previously described, it is possible to start with the classification of the data:

1. Selection of the input vector to fed in the first trained SOM (e.g. the first pixel of an image);
2. Selection of the winning neuron in the first SOM;
3. Elaboration of the weights vector related to the winning neuron in the first SOM (step 2) by the second trained SOM;
4. Selection of the winning neuron in the second SOM and storing of the relative output;
5. Algorithm repetition from step 1 until all pixel are classified.

In Fig. 2.24(a) is shown a $[10 \times 10]$ **U**-matrix and in Fig. 2.24(b), 2.24(c) its clustering by means of a $[2 \times 2]$ and $[2 \times 1]$ SOM respectively.

After the clustering procedure performed with the $[2 \times 2]$ SOM, four regions are identified (0, 1, 2, 3), whereas when a $[2 \times 1]$ SOM is used only two classes are identified.

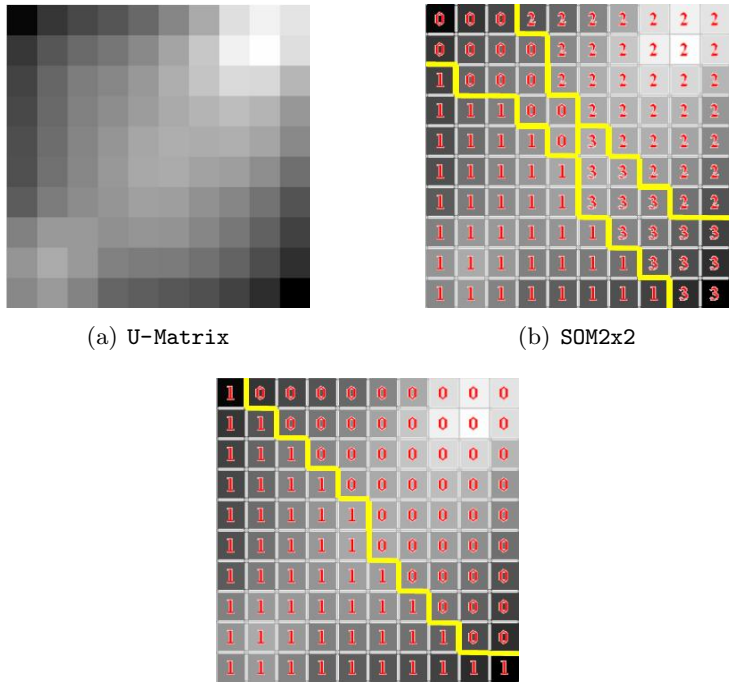

(a) `U-Matrix` (b) `SOM2x2`

(c) `SOM2x1`

Figure 2.24: SOM based re-clustering.

Chapter 3

PolSOM and TexSOM in Polarimetric SAR Classification

Two novel methods of unsupervised classification of polarimetric SAR data are now proposed and critically discussed by comparing their performance with those of other approaches, in particular with H/A/α–W algorithm (Sect. 2.1.14) and with Lee's category–preserving (Freeman–Durden) algorithm (Sect. (2.1.15)), which are currently the most widely used methods for classifying this type of data (Sect. (1)).

The developed neural network algorithms are named PolSOM and TexSOM, since both methods are based on the Self-Organizing Map (SOM) unsupervised neural networks. From a certain point of view, TexSOM can be considered an evolution of PolSOM. The SOM approach in this work is independent of the sensor, has a modular structure and is able to provide real–time results. The developed algorithms have been tested on both airborne and space borne polarimetric SAR data acquired at L–band by AirSAR and at C–band by RADARSAT-2.

3.1 Introduction

The potential of SAR in discriminating different kinds of surfaces and objects has been widely analyzed. Extensive experimental SAR polarimetry was essentially fostered by the AirSAR and SIR systems. Part of the polarimetric data used in the following were acquired by the JPL/NASA airborne AirSAR (Fig. 3.11) on a hilly area in Tuscany (Sect. (3.2.1.1)). The others were acquired by the RADARSAT-2 SAR on the Colli Albani Area in Latium (Sect. (3.2.2.2)). Ground truth has been obtained by

Figure 3.1: JPL Airsar.

both *in–situ* inspections and by careful photo–interpretation of very–high resolution optical images, in order to assess the classification results by reliable confusion matrices.

3.2 Data Set

3.2.1 NASA/JPL AIRSAR

The P–, L–, and C– band data from AirSAR were delivered in compressed Stokes matrix format, with 10 bytes per pixel, and calibrated to represent the normalized radar cross section σ^0 (m^2/m^2). In particular, the used data are PolSAR CM products, generated by v3.56 processor. Each CM frame product contains three files, one for each frequency and data storing uses a compressed Stokes matrix procedure. Details on AirSAR data compression and decompression are in Appendix A.

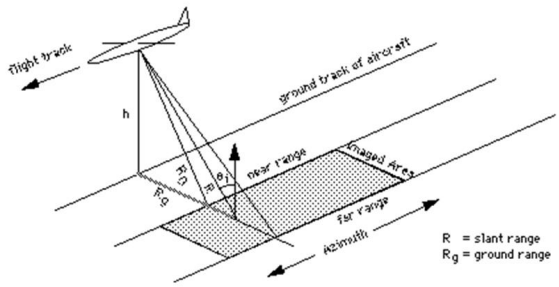

Figure 3.2: Airsar acquisition geometry.

3.2.1.1 Montespertoli Test Site and Ground Truth

Many test sites have been used for the analysis of polarimetric SAR data. The Flevoland test site in the Netherlands has probably been the most intensively observed [78], [91]. The Foulum Danish EMISAR test site, Denmark, is also worth citing [130]. The preceding sites are in relatively flat areas, with fairly regular and relatively large homogeneous fields. Less frequent are the results for undulating, heterogeneous and fragmented landscapes, where classification can become quite challenging. The new SOM algorithms where tested on this kind of complex landscape, typical of Central Italy.

One of the Italian test sites for the Multi-sensor Airborne Campaign (MAC-Europe), which took place in the summer of 1991 in several European countries, was located near Montespertoli [111], a rural area in south-west of Florence (Fig. 3.3), which well represents the Thyrrenian-Appenine complex landscape: the area is dominated by hills with average elevation around 250 meters and, in the remaining part, mainly in the river Pesa valley, is rather flat and intensively cultivated. More than half of the Montespertoli site has hilly woodland, vineyards, olive groves, pastures, and some urbanization. The flat area has irregular fields with sunflower, corn, sorghum, colza, wheat, and alfalfa. The ground data, collected in correspondence of the flights [73], include information like tree height, forest density, crop type and stage of

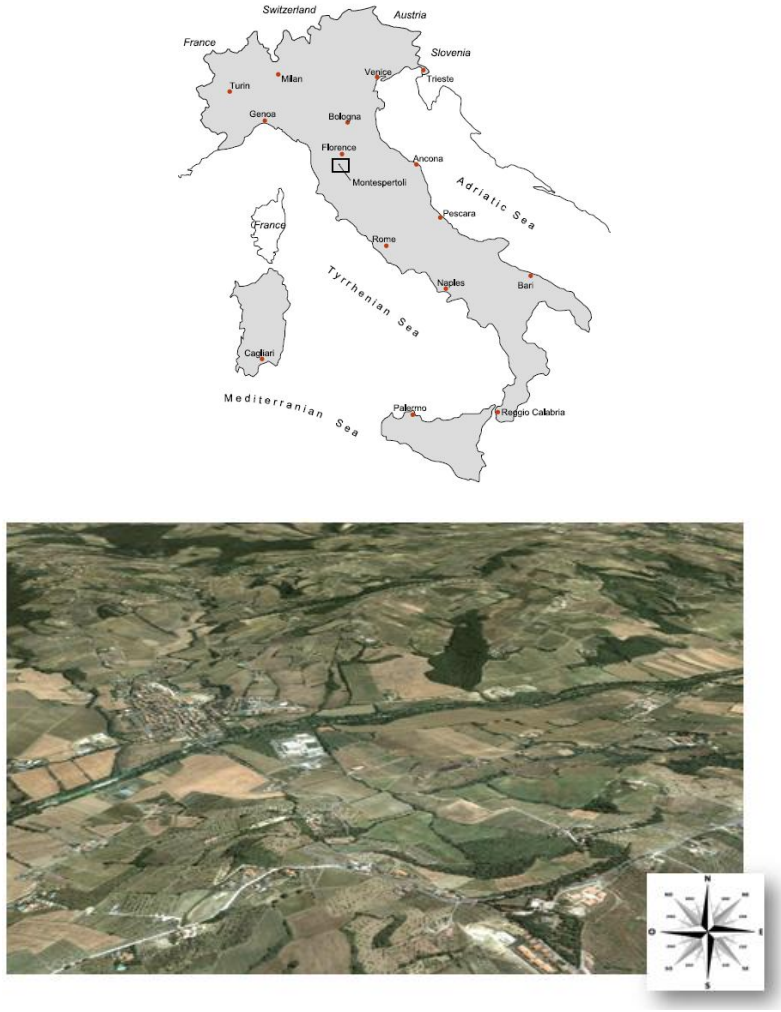

Figure 3.3: AirSAR Test Site.

development and, for a significant set of fields, significant soil and vegetation parameters, such as Leaf Area Index (LAI), Plant Water Content (PWC), dimensions of leaves and stalks, soil moisture content (SMC) and roughness. Forests are dominated by pubescent oak and European turkey oak species, with a limited presence of European hornbeam and Italian cypress. Forests are dense, with basal areas (i.e., normalized trunk base areas) in the range of 70–150 m^2/ha, trunk densities in the range of $2000 - 8000$ ha^{-1}, while tree heights are in the range $10 - 20$ m. Olive groves basal areas are ≈ 10 m^2/ha for all selected fields, densities are 300 ha^{-1} , while tree heights are ≈ 3 m. The AirSAR data were acquired between 22 June 1991 and 14 July 1991. The Plant Water Content (in kg/m^2) was $\approx 0.5 - 5.0$ for sunflower, $\approx 0.2 - 1.5$ for corn, $\approx 0.2 - 1.0$ for sorghum and $\approx 0.2 - 3.0$ for alfalfa. Wheat and colza were in their ripening stage at the time of the middle flights. The density of sunflower and corn plant is < 10 m^{-2}, their stalk diameter is around 1-3 cm, and their average leaf area around 10-40 cm^2 . Colza, wheat, and alfalfa have plant density in the range 80-500 m^{-2}, stalk diameter about 0.2-1.2 cm and leaves of length <1 cm or absent. Fig. 3.4 shows the ground truth map of the Montespertoli area. The polarimetric data set has been extracted from the database created by the Tor Vergata led ERA-ORA European project ("http://eraora.disp.uniroma2.it/").

3.2.1.2 Montespertoli data overview

Tab. 3.1 lists the analyzed Montespertoli AirSAR polarimetric data. As detailed in the table, the considered data where acquired on 22 June 1991, 29 June 1991 and 14 July 1991. On each date, three look angles where used for all acquisition bands, so that a set of 27 images was collected. The acquisitions are 16-look with 1279 rows and 1024 columns. The ground resolution is about 12 m.

Out of the available images, the one of 22 June 1991 at 50° was chosen and analyzed in detail (image label: CM3151).

Fig. 3.5 displays an RGB combination of images at P– L– and C– band, respectively, where the R channel corresponds to σ^0_{HH}, G channel to σ^0_{HV} and B channel to σ^0_{VV}.

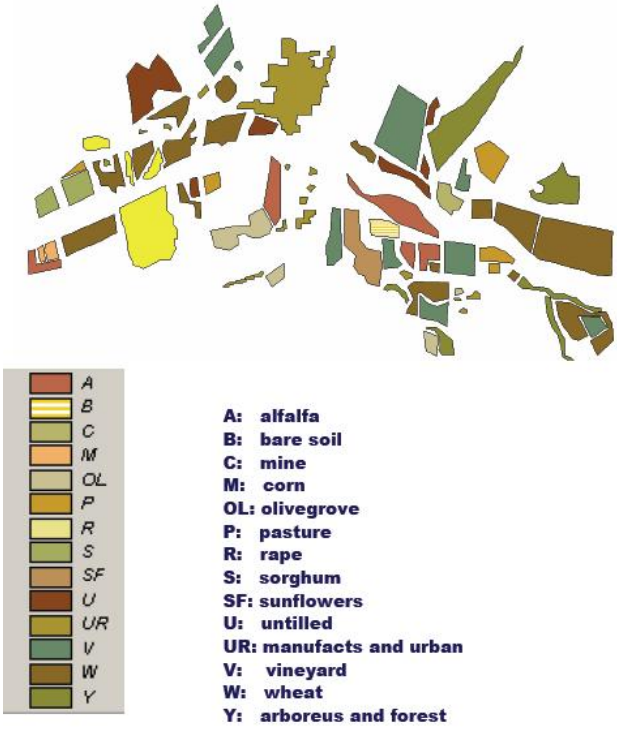

Figure 3.4: Ground Truth.

File Name	CCT ID	Band	Date	Target look angle
F11	CM3151P	P	22 Jun 91	50^0
F21	CM3151L	L	22 Jun 91	50^0
F31	CM3151C	C	22 Jun 91	50^0
F41	CM3166P	P	22 Jun 91	35^0
F51	CM3166L	L	22 Jun 91	35^0
F61	CM3166C	C	22 Jun 91	35^0
F71	CM3196P	P	22 Jun 91	20^0
F81	CM3196L	L	22 Jun 91	20^0
F91	CM3196C	C	22 Jun 91	20^0
G11	CM3292P	P	29 Jun 91	50^0
G21	CM3292L	L	29 Jun 91	50^0
G31	CM3292C	C	29 Jun 91	50^0
G41	CM3314P	P	29 Jun 91	35^0
G51	CM3314L	L	29 Jun 91	35^0
G61	CM3314C	C	29 Jun 91	35^0
G71	CM3326P	P	29 Jun 91	20^0
G81	CM3326L	L	29 Jun 91	20^0
G91	CM3326C	C	29 Jun 91	20^0
H11	CM3355P	P	14 Jul 91	50^0
H21	CM3355L	L	14 Jul 91	50^0
H31	CM3355C	C	14 Jul 91	50^0
H41	CM3380P	P	14 Jul 91	35^0
H51	CM3380L	L	14 Jul 91	35^0
H61	CM3380C	C	14 Jul 91	35^0
H71	CM3396P	P	14 Jul 91	20^0
H81	CM3396L	L	14 Jul 91	20^0
H91	CM3396C	C	14 Jul 91	20^0

Table 3.1: Analyzed data.

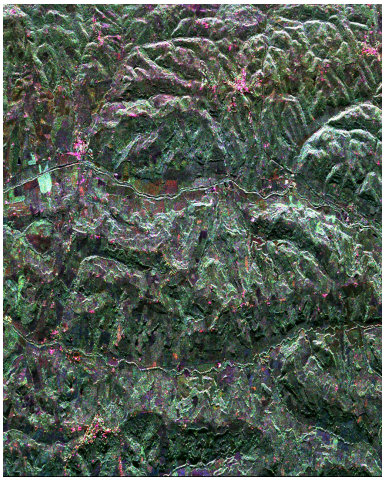

(a) CM3151C

(b) CM3151L

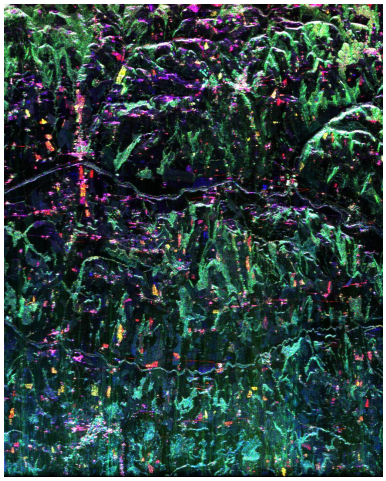

(c) CM3151P

Figure 3.5: RGB representation of σ^0: R, σ^0_{HH}; G, σ^0_{HV}; B, σ^0_{VV}, measured on 22 June 1991 at 50^0.

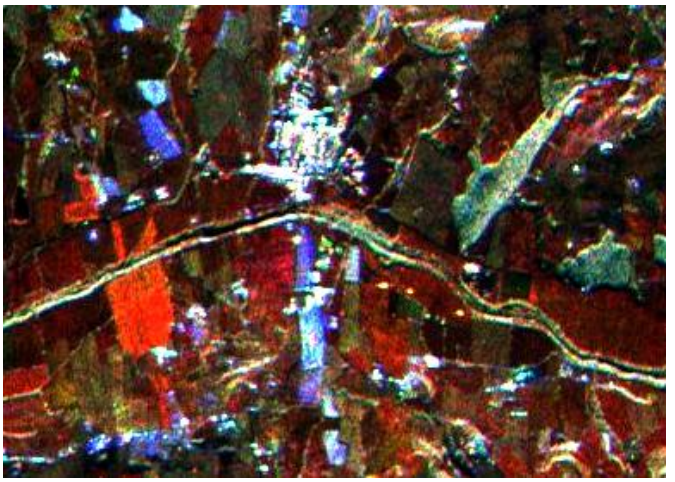

Figure 3.6: Multi-band total power image: R, C-band; G, L-band, B, P-band total power.

A multi-band image has been generated from the total power images of each band, by the average co- and cross polarized power:

$$X_{TP} = \frac{1}{4}(\sigma^0_{X_{HH}} + 2\sigma^0_{X_{HV}} + \sigma^0_{X_{VV}}) \tag{3.1}$$

where $(X = C, L, P)$. The C-band total power C_{TP} is fed in the red channel, and L_{TP} and P_{TP} in the green and blue, respectively, to produce the multi-band total power image shown in Fig 3.6.

A subset of the data relative to the area for which the ground truth data had been collected has been considered in the classification exercise. This sub-area, of 274 pixels by 385 pixels is shown in Fig. 3.7 with the superimposed ground truth.

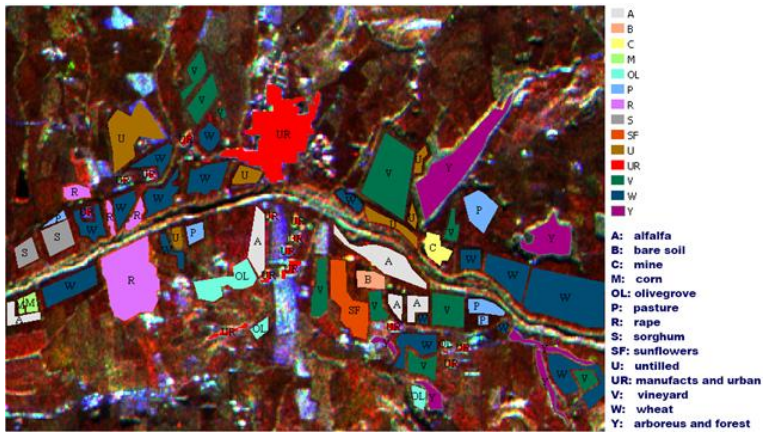

Figure 3.7: The sub-area considered for classification with superimposed ground truth.

3.2.2 RADARSAT-2

A set of images acquired in a full polarimetric mode by the C–band RADARSAT-2 on the Tor Vergata Colli Albani test site was provided through MDA Geospatial Services Inc. by the Canadian Space Agency within the Science and Operational Application Research for RADARSAT-2 program. A time series of 10 images of the site were collected in the last 5 months of 2008. An image subset was selected for testing the developed classification algorithms.

3.2.2.1 Tor Vergata Colli Albani Test Site and Ground Truth

The Colli Albani area and the contiguous Tor Vergata University campus are in the outskirts of Rome, Italy, and form an interesting land cover study site, given their heterogeneity and high urbanistic dynamics. Cereals and vegetables fields are encountered together with extended vineyards and olive groves, mixed with woodland, recent and historic residential areas, isolated buildings of various dimensions and ages, industrial and commercial

Figure 3.8: Tor Vergata Colli Albani Area.

complexes and miscellaneous artificial surfaces. The study area, shown in Fig. 3.8 includes also part of the city of Rome for an overall extension of about 800 square kilometers (6194 × 3248 pixels).

The ground truth was manually edited (Fig. 3.9), since the area is well known, several metric-resolution optical image are availble and *in-situ* inspections were also performed for ground truth validation.

3.2.2.2 Tor Vergata Colli Albani data analysis

The selected image over which the classification exercise was performed is an SLC fine resolution Quad–polarization, with a resolution of about 10 m in slant range geometry. Radar measurements are recorded in GeoTIFF format, one file for each polarization. Calibration files are also provided in

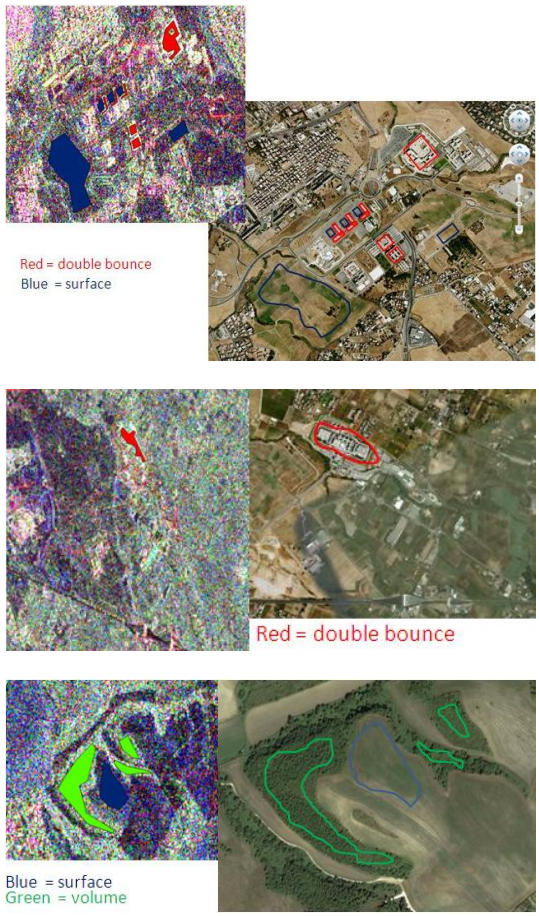

Figure 3.9: Tor Vergata Colli Albani ground truth .

```
RS2_OK2289_PK28135_DK31855_FQ14_20080908_051754_HH_VV_HV_VH_SLC
|    BrowseImage.tif
|    DFAIT_RS2 Single User License.pdf
|    imagery_HH.tif
|    imagery_HV.tif
|    imagery_VH.tif
|    imagery_VV.tif
|    lutBeta.xml
|    lutGamma.xml
|    lutSigma.xml
|    product.xml
|
|___schemas
         rs2prod_attitudeAngles.xsd
         rs2prod_attitudeInformation.xsd
         rs2prod_chirp.xsd
         rs2prod_chirpQuality.xsd
         rs2prod_dataTypes.xsd
         rs2prod_dopplerCentroid.xsd
         rs2prod_dopplerRateValues.xsd
         rs2prod_ellipsoidParameters.xsd
         rs2prod_generalProcessingInformation.xsd
         rs2prod_geodeticCoordinate.xsd
```

Figure 3.10: RADARSAT–2 image foder tree.

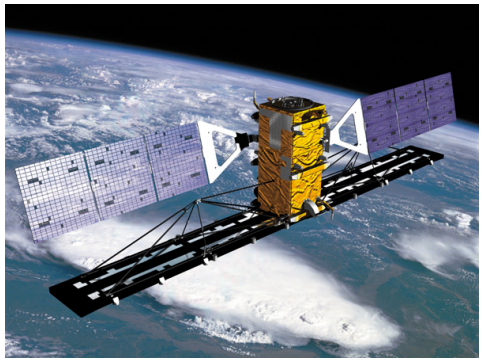

Figure 3.11: RADARSAT–2.

.xml format. A folder tree of the image is shown in Fig. 3.11.

The image was acquired on 8 September 2008 in a descending pass. All information is contained in the product.xml file. The three files lutBeta.xml, lutGamma.xml and lutSigma.xml contain the look–up tables for the con-

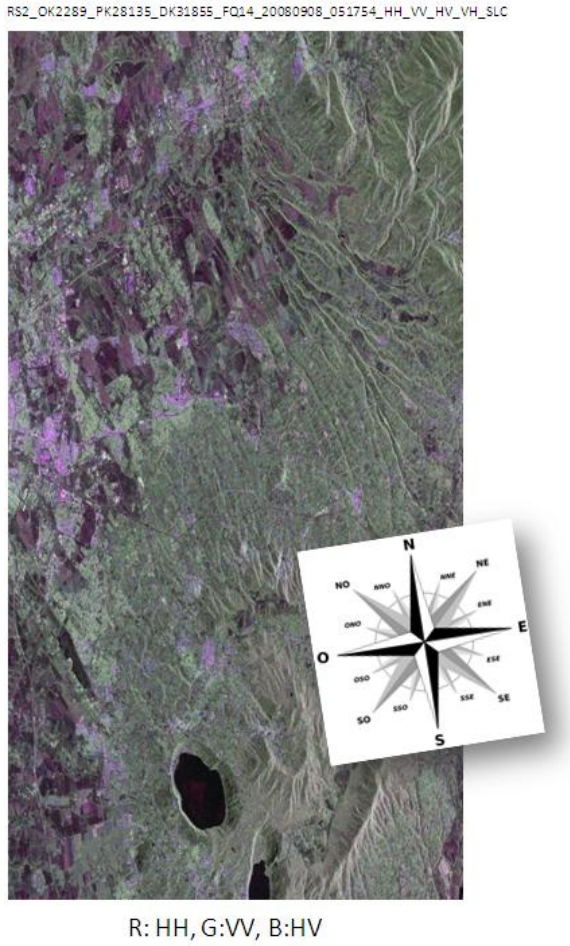

Figure 3.12: Tor Vergata Colli Albani RADARSAT–2 image.

version digital number to β, γ or σ rispectively. In Fig. 3.12 the selected RADARSAT–2 image is shown.

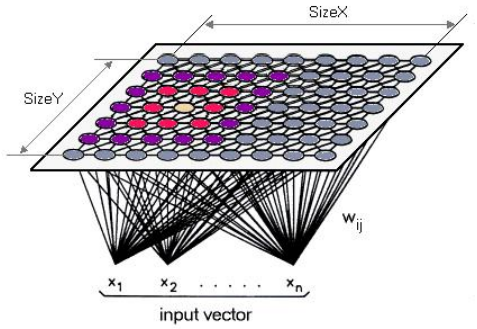

Figure 3.13: Typical architecture of a SOM network.

3.3 PolSOM

3.3.1 Introduction

Neural networks have some advantageous features, including non-linear input–output mapping, ability to adaptive learning and endurance to corrupted inputs. An interesting property is their ability in handling (e.g., classify) multiple data with different or unknown distributions [131]. However, main disadvantages of neural networks derive from the unknown set of rules for their topology and parameter setting. This leads to many implementation uncertainties, including the initialization of the weight values, the selection of the appropriate learning algorithm, etc. [131].

A new approach in designing the neural network is proposed in this work to overcome the above difficulties. The first objective, indeed, was to understand how the network behaves and evolves during the classification process. This analysis has allowed to avoid the commonly used random initialization of weights and to manage the net in a controlled way. The activities that have been carried out are outlined in Tab. 3.2 and detailed in the next sections.

	Activity description	*Reference Section*
1.	PolSOM IDL code developing	3.3.2
2.	Input data pre–processing	3.3.3
3.	New SOM Training technique	3.3.4
4.	AirSAR C–, L– and P–band polarimetric data classification with POLSOM	3.3.5
5.	Comparison among PolSOM classification results obtained with different AirSAR bands	3.3.5
6.	AirSAR C–, L– and P–band polarimetric data H/A/α–W classification	3.3.6
7.	Comparison between PolSOM algorithm and H/A/α–W algorithm	3.3.6
8.	RADARSAT-2 PolSOM classification	3.3.7
9.	RADARSAT-2 classification preserving polarimetric scattering characteristics	3.3.8
10.	Comparison between PolSOM algorithm and Lee's algorithm	3.3.8

Table 3.2: PolSOM development scheme.

3.3.2 PolSOM IDL code developing

The first version of a PolSOM IDL code was developed in 2005 and used to classify a SAR polarimetric image, as detailed in [132]. That release was not optimized and its use was not easy. A new release of the software was implemented by Marco Del Greco in 2006 during his Master Thesis [133]. Both versions had no graphical interface and worked through command line. A new software release is being currently implemented, in which some bugs are fixed and a new graphical user interface is provided. The ongoing PolSOM release is schematized in Fig. 3.14.

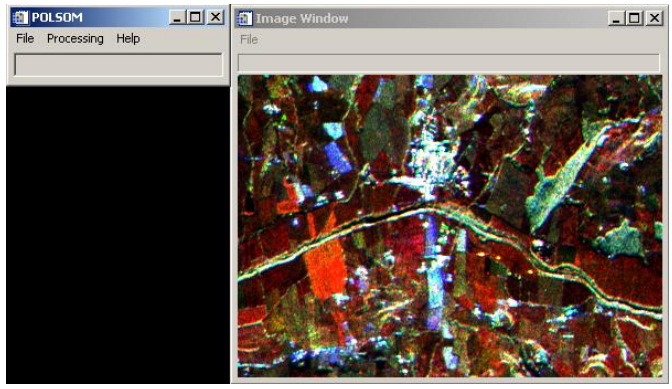

Figure 3.14: PolSOM Graphical User Interface.

3.3.3 Input data pre–processing

Fig. 3.15 shows the backscattering coefficients at the principal polarizations, together with the phase difference (HH-VV) of the selected CM3151 L-band AirSAR data acquisition.

The power color-composite Fig. 3.16 suggests that the backscattering of particular regions is mainly contributed by a single polarization (e.g., HH polarization in parts of the urban area, HV in woodland, VV in some fields), while different scattering mechanisms (Fig. 3.18) generally coexist over the imaged area.

The $HH - VV$ phase (Fig. 3.17), in turn, shows a typical behavior in peculiar regions, like the urban area (Fig. 3.19), where it is frequently close to π.

Hoekman [134] demonstrated that the polarimetric properties of a target can also be expressed by nine independent single–polarization observables. The property suggests the use of the scattering intensities at the 9 principal polarizations instead of the scattering matrix, without loss of information and with the advantage of requiring non–polarimetric segmentation software [134]. Following the approach, a 9–components vector was synthesized for each pixel from the data for each band. The principal polarizations are: HH,

(a) `HH`

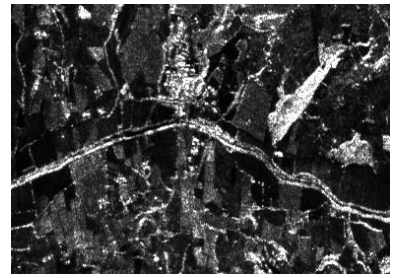

(b) `HV`

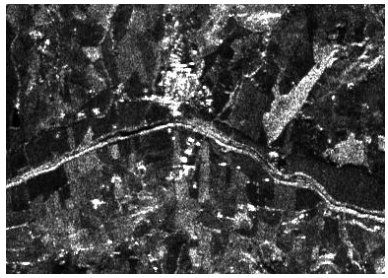

(c) `VV`

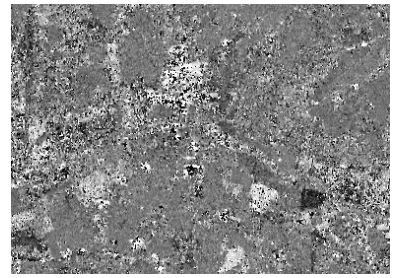

(d) `phase`

Figure 3.15: Input data.

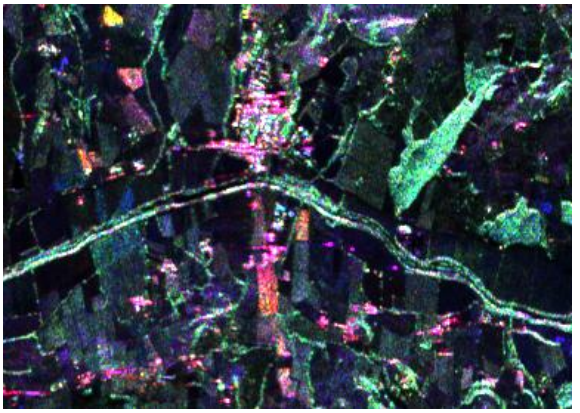

Figure 3.16: L–band composited image: R, σ^0_{HH}; G, σ^0_{HV}; B, σ^0_{VV}.

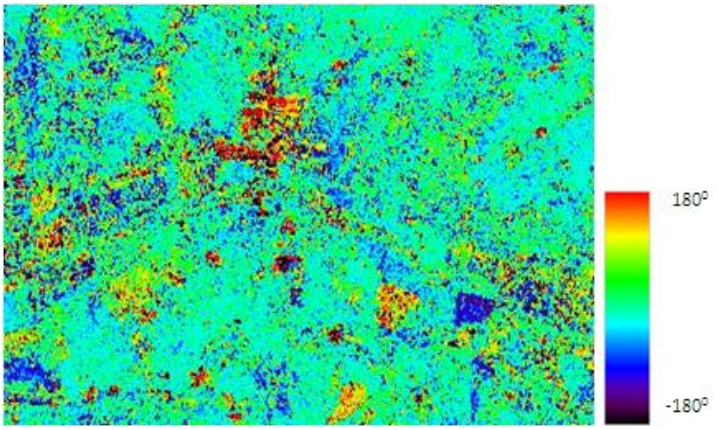

Figure 3.17: $HH - VV$ phase color-coded image.

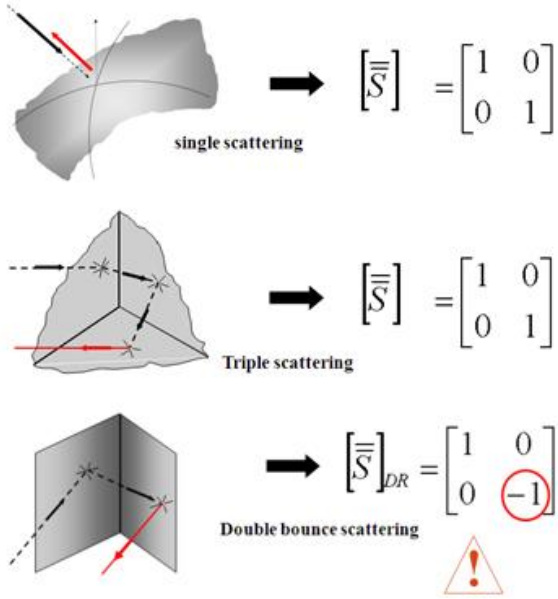

Figure 3.18: Scattering mechanisms and associated scattering matrices.

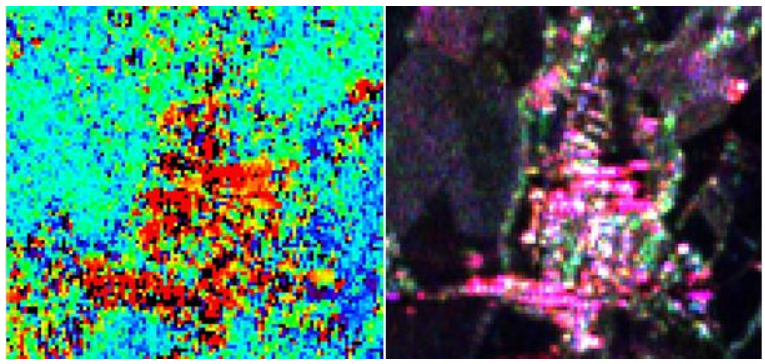

Figure 3.19: Urban area: principal polarizations power RGB composite (right) and $HH - VV$ phase color image (left).

HV, VV, RR, RL, LL, $Lin45^0Lin45^0$, $Lin45^0Lin135^0$, $Lin135^0Lin135^0$, where R is for right-hand circular polarization, L for the left one and Lin for linear polarization.

The images in Fig. 3.20 suggests how the different polarizations put into evidence the L–band different features of targets, thus allowing a polarimetric analysis.

3.3.4 New SOM Training technique

Given their concept and implementation, SOM networks do not need training and for this reason they are suited for unsupervised classification. However, as explained in Sect. (2.2), this kind of network is sensitive to the probability density functions of the input data. Such a feature can be an advantage for some applications, but could become a disadvantage for remote sensing purposes, because classes represented with fewer pixels could be underestimated.

Consider a set of points, ranging between 0 and 100, in the bi-dimensional plane, having a exponential density of probability (Fig. 3.21).

If these points are classified using a $[6 \times 6]$ SOM, the network topology approximates an exponential function.

Each point of Fig. 3.22 represents the weights vector for each neuron of the $[6 \times 6]$ SOM. Note that the neurons tend to reproduce the probability function of the input data: in fact the neurons gather in the area where the input values cluster. The same conclusions can be reached if a U–matrix is used. U–matrix representation is the way to visualize the network status for more than the two-dimensional case (more than 2 inputs). As explained in Sect.2.2.8, U–Matrix data visualization does not depend on the number of inputs of the net. Each neuron, with associated coordinate (i, j), is characterized by a vector of weights whose dimension depends on the number of inputs. For each neuron, the values of distances from its neighbors can be added and the result divided by their number. This mean value is stored in the U–matrix at the same coordinate of the considered neuron. This procedure leads to a graphic representation of the relations between the neurons: the dark areas on the map correspond to closely

(a) HH

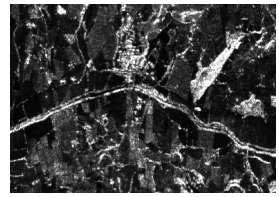

(b) HV

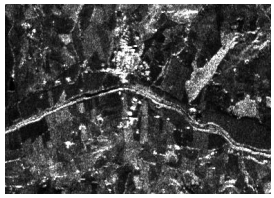

(c) VV

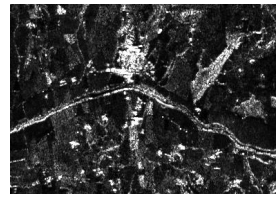

(d) RR

(e) RL

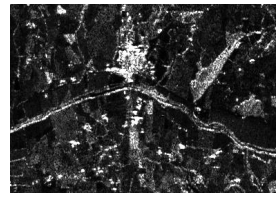

(f) LL

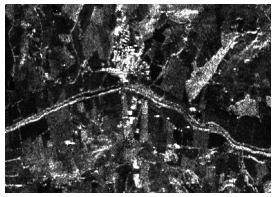

(g) Lin4545

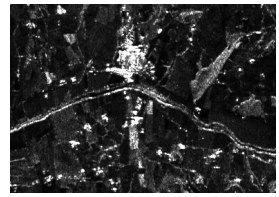

(h) Lin45135

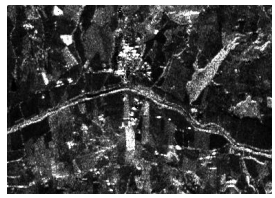

(i) Lin135135

Figure 3.20: Intensity images at the 9 principal polarizations.

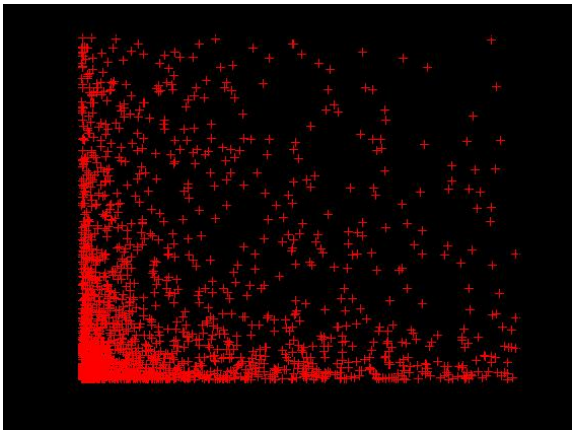

Figure 3.21: Simulated set of points.

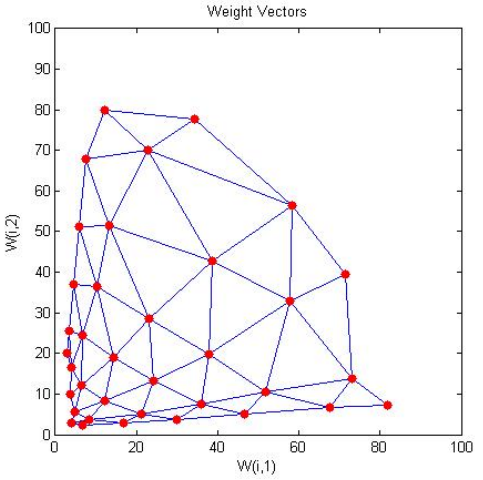

Figure 3.22: Weights of a 6×6 SOM classifier of the data set in Fig. 3.21.

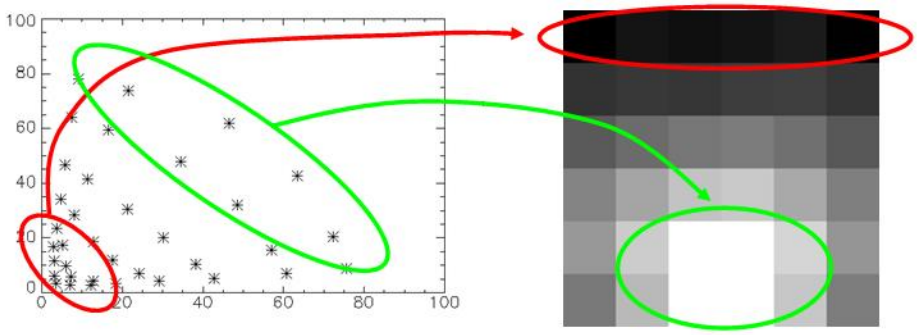

Figure 3.23: Comparison between weights vector diagram (left) and U-matrix representation (right) for the 6×6 SOM classifier of the data set in Fig. 3.21.

packed neurons, while the clear areas correspond to sparse neurons.

Now it should be clear that a SOM classifier needs a proper preparation for optimally receiving the data. This procedure can be seen as a training of the net that can be performed in a supervised (Sect. (3.3.4.1.2)) or unsupervised Sect. (3.3.4.2)) way. In the starting phase a supervised procedure was implemented to observe the expected improvements. In the subsequent phase, an unsupervised training method was implemented and tested. A procedure common to both methods has been the use of the 9-dimensional vectors corresponding to the principal polarizations (3.3.3).

3.3.4.1 Supervised Training

Polarimetric images are often visualized by Pauli decomposition and subsequent RGB representation of the three components. The red channel represents $|HH - VV|$, the green $|HV|$ and the blue $|HH + VV|$. The AirSAR image used in the classification exercise has been first decomposed, both for a proper understanding of its information content and for a better comprehension of the SOM classification procedure. Pauli decomposition–based images for C–, L– and P–band of the considered CM3151 data are

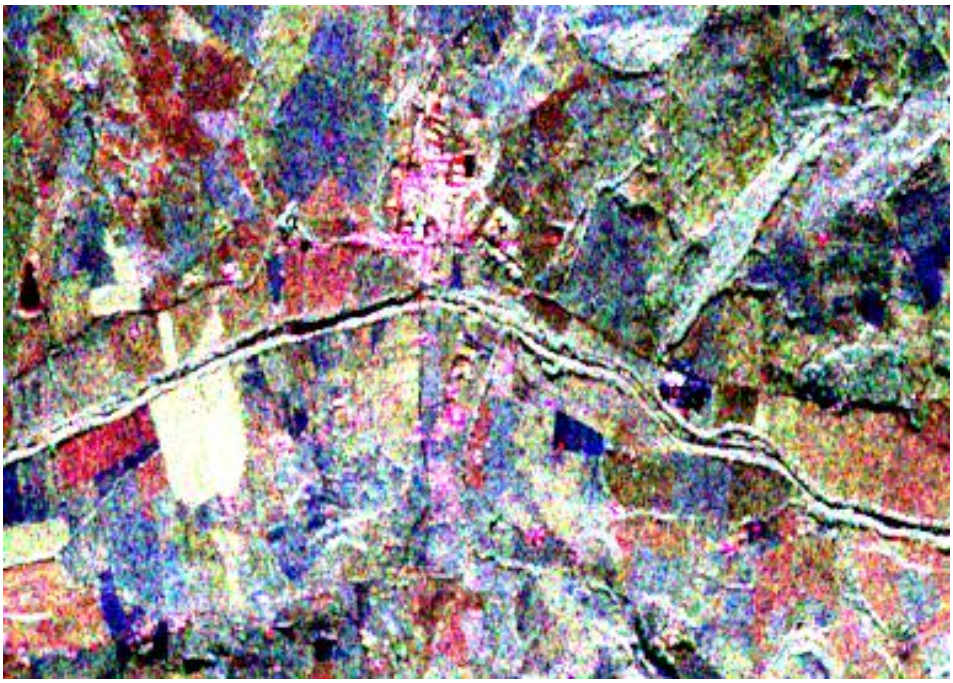

Figure 3.24: Pauli decomposition for C band (CM3151).

shown in Fig. 3.24, Fig. 3.25 and Fig. 3.26 respectively.

A $[10 \times 10]$ SOM was used, based on an empirical approach, since a direct relation between number of neurons and accuracy of the result is difficult to establish. One hundred neurons represent a compromise between processing time and result accuracy. Since a $[10 \times 10]$ SOM cluster the image in 100 classes, a second $[16 \times 1]$ SOM was used to reduce the number of classes to 16 (Fig. 3.27). The input of the second network coincides with the output of the first network. Hence 16 classes were considered in the preliminary analysis to have a direct comparison with other methods.

The first classification result for a random weight initialization is shown in Fig. 3.28. Urban and forest, even if characterized by different scattering

Figure 3.25: Pauli decomposition for L band (CM3151).

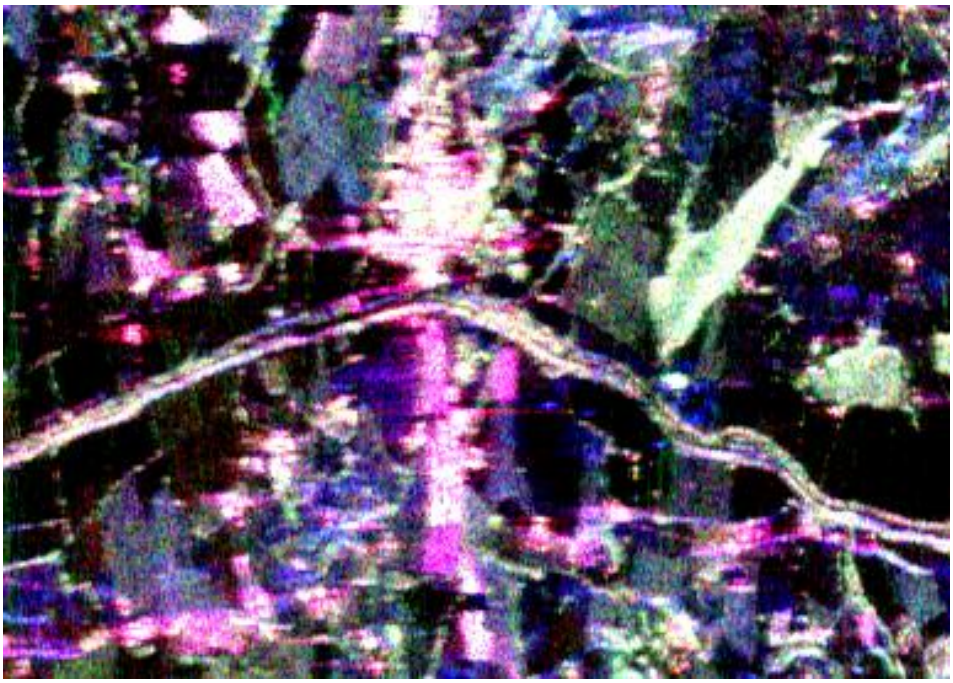

Figure 3.26: Pauli decomposition for P band (CM3151).

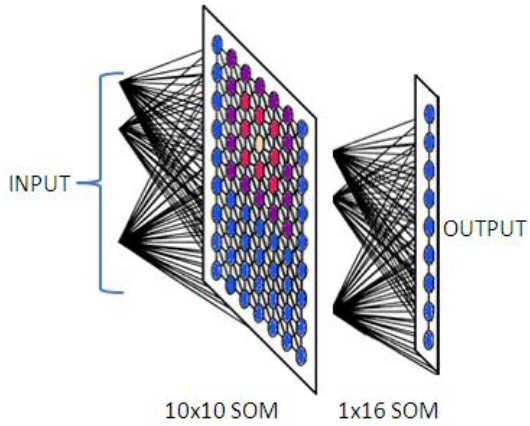

Figure 3.27: PolSOM scheme.

properties, are assigned to the same class. Arable land and permanent crops are discriminated, with a better sensitivity in separating colza and vineyard.

The next step consisted in a supervised training to make the net more apt to polarimetric data processing. Pixels clearly characterized by double-bounce, surface and volume scattering mechanisms have been singled out and mixed together to built the training set. The selection of the pixels has been performed with two different criteria.

To this end, the polarimetric signatures have first been computed, and the subsequent pixel selection carried out as follows:

- One pixel for the double bounce scattering mechanism, in the urban area (Fig. 3.29), having:
  1. phase–difference (HH–VV) value=π;
  2. high values of HH.
- One pixel for surface scattering mechanism, in the bare soil area (see Fig. 3.30), having:

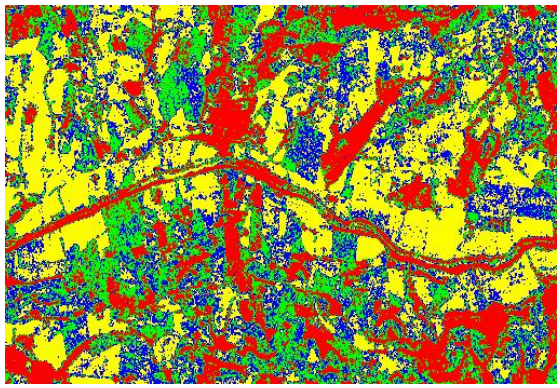

(a) `L-Band_SOM_Classification`

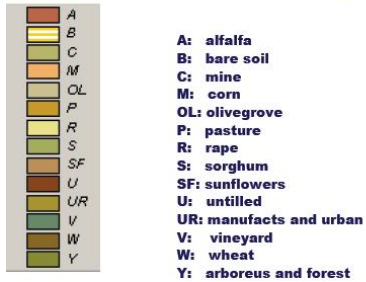

(b) `Ground_Truth`

Figure 3.28: L-Band SOM classification with random weight initialization. .

1. phase–difference (HH–VV) value≈ 0;
2. low values of HV.

- Six pixels (to be averaged) for volume scattering mechanism, in the forest area (see Fig. 3.31), having:
  1. phase–difference (HH–VV) value≈ 0;
  2. high values of HV.

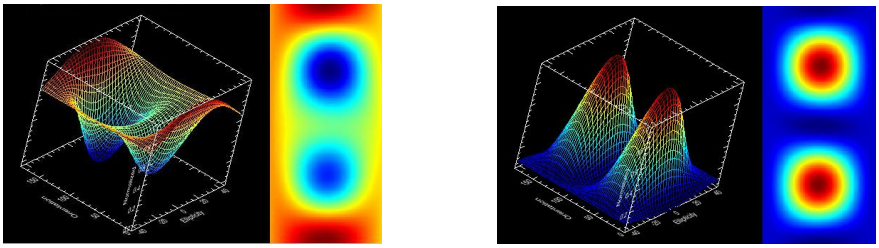

(a) `UR_co` (b) `UR_cross`

Figure 3.29: Urban polarimetric signature at L-Band.

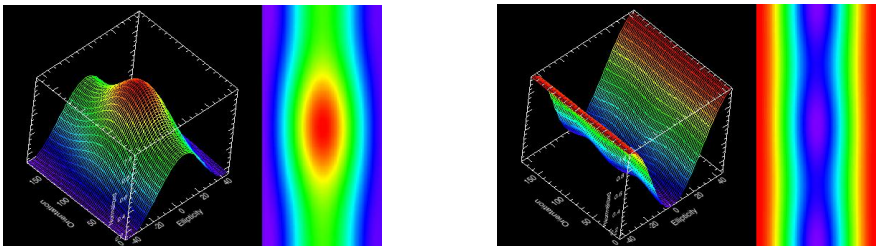

(a) `BS_co` (b) `BS_cross`

Figure 3.30: Bare Soil polarimetric signature at L-Band.

The selection was performed at C–, L– and P–band, so that three 9-components (Sect. (3.3.3)) representative vectors (Fig. 3.32) were synthesized (one with the intensity values of the double-bounce pixel, the second

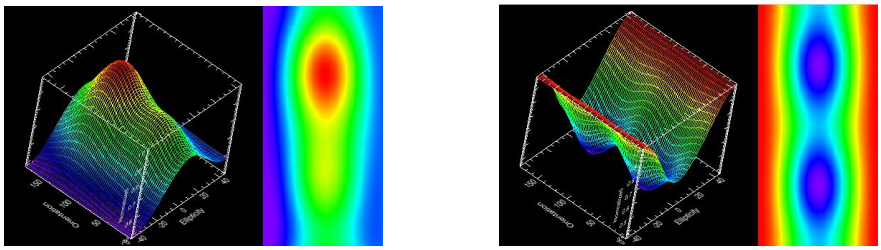

(a) `Fo_co` (b) `Fo_cross`

Figure 3.31: Forest polarimetric signature at L-Band.

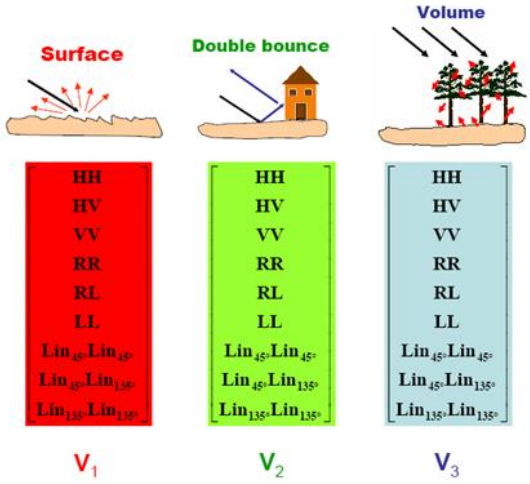

Figure 3.32: 3 Input vectors with 9 components.

with the surface pixel values and the last one with the average values of the forest pixels) to construct the training set for each frequency.

3.3.4.1.1 Gaussian training data set. Gaussian noise was then added to the three representative vectors in Fig. 3.32, resulting in the trained

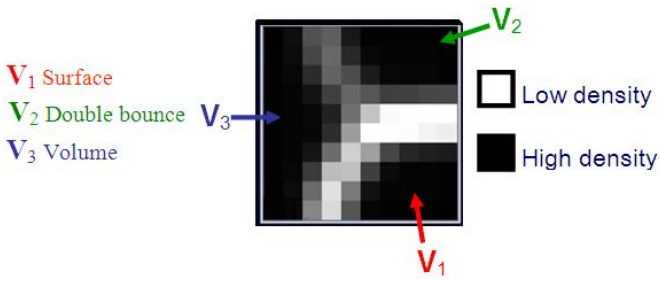

Figure 3.33: U-Matrix after Gaussian training.

U-Matrix corresponding to the [10 × 10] SOM shown in Fig. 3.33.

Note that the portion of U-Matrix referring to surface scattering is clearly separated from the others. The double bounce and the volume scattering show less separation. This first analysis hints at a more difficult discrimination between the latter two mechanisms compared to the first.

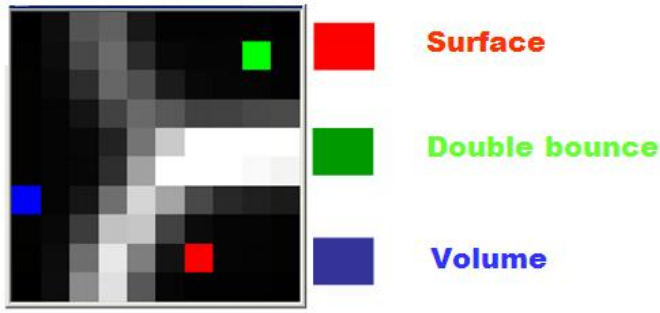

Figure 3.34: U-Matrix and representative vectors.

Fig. 3.34 displays the neurons activated by the representative vectors synthesized by the procedure of Sect. (3.3.3). The vectors are not placed at their maximum respective distance; however, they are well separated and the network has allocated a high number of neurons for each principal mechanism (dark areas, i.e., high neuron density).

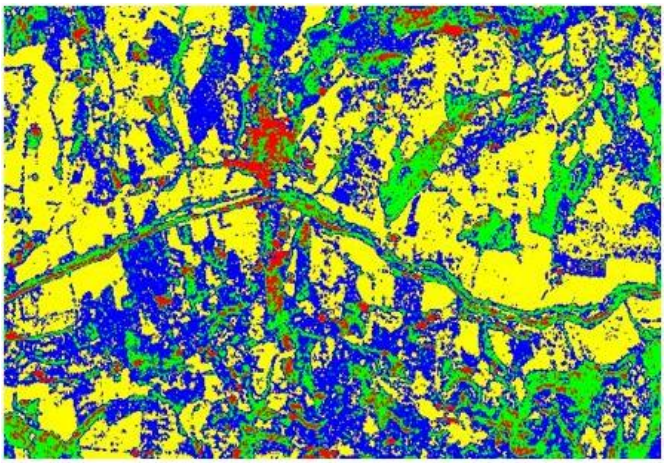

Overall Accuracy = (13926/16787) 82.96%
Kappa Coefficient= 0.74

	Ground Truth			
Class	**Forest**	**Vineyards & Rape**	**Crops**	**Urban**
Forest	80.38	4.76	1.30	25.51
Vineyards & Rape	7.16	78.86	10.17	2.48
Crops	0.00	16.38	88.51	0.00
Urban	12.45	0.00	0.02	72.01

Figure 3.35: Four classes L–band classification using Gaussian training: red, urban; green, forest; blue, rapeseed and vineyards; yellow, crops.

The PolSOM implemented as described by the above procedure has finally classified the chosen L-band image, obtaining the result shown in Fig. 3.35. The overall accuracy is higher than the one of the first classification (Fig. 3.28), but there is still some confusion between urban and forest, as previously suggested by the analysis of the U-Matrix.

3.3.4.1.2 Mixed Training data set. Especially at decametric spatial resolution, very few targets are characterized by pure scattering mechanisms, hence a new way to train the SOM is needed. The scheme is based on the generation of a mixed training data set starting form the three pure scattering mechanisms. To this aim, appropriate combinations of pure mechanisms have been formed by adding weighted pairs of the three representative vectors, as shown in Fig. 3.36.

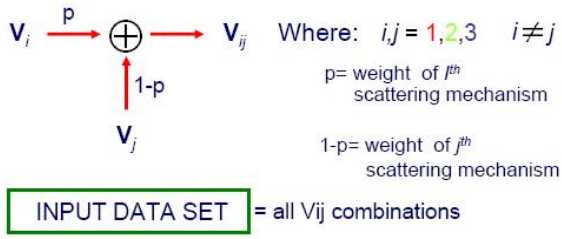

Figure 3.36: Mixed training data set synthesis.

An interesting exercise consists in the U–Matrix visualization of the status of the network during the training process. The evolution of the network with progressing training (i.e., with increasing p parameter) is shown in Fig. 3.37. The network progressively adapts to recognize mixed

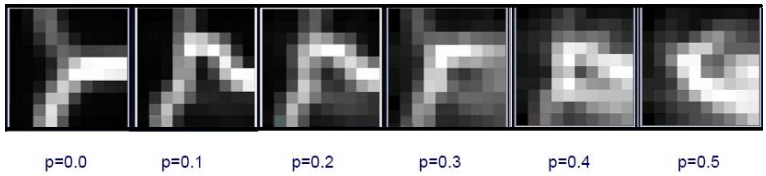

Figure 3.37: Evolution of U-Matrix in the course of mixed training.

mechanisms, allocating less neurons for the identification of pure mechanisms. The evolution of the three original pure-mechanism representative vectors can be also visualized on the U-Matrix (Fig. 3.38). It is important to note that the distance among the pure-scattering representative vectors has

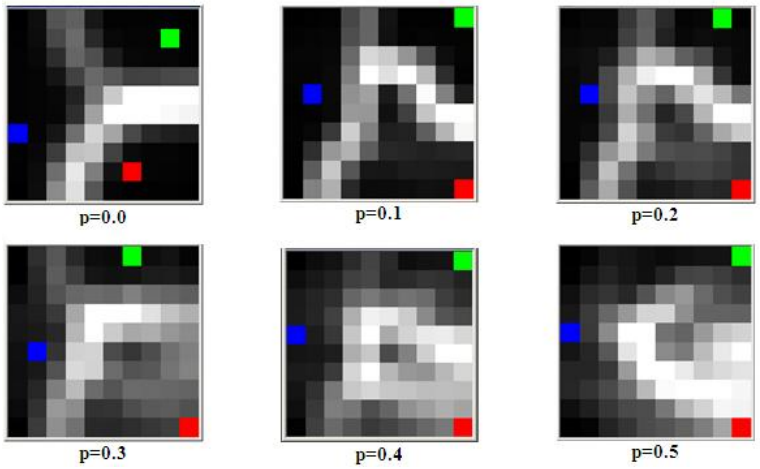

Figure 3.38: Pure-scattering vectors on the U-Matrix as mixed training progresses.

an increasing trend as training progresses and, at the end of the process, the vectors are placed at the maximum relative distances. This means that the PolSOM is "better prepared" to accept the input data, in terms of separation among different scattering mechanisms. The result of the classification obtained after this mixed training procedure is shown in Fig. 3.39 and compared with that obtained by Gaussian training: the overall accuracy has increased by about 3%, and now exceeds 85%.

3.3.4.2 Unsupervised Training

To make further automatic the method, an unsupervised procedure has been developed for selecting the pixels from which the 9-components representative vectors can be synthesized. The Pauli decomposition is used to this purpose, as detailed in the following scheme:

- Double–bounce scattering mechanisms: the training set includes pixels having, at the same time, high values of Pauli's double-bounce

component and low values of volume component;

- Surface scattering mechanisms: a percentage of pixels having predominant Pauli surface component;

- Volume scattering mechanisms: the procedure is reciprocal to the double-bounce.

The SOM trained by the unsupervised method has classified the polarimetric L–band image with the results shown in Fig. 3.40 for a three-class discrimination[1].

To compare the results of Fig. 3.40 with those of Fig. 3.40, this latter has to be reclassified in three classes: the loss of accuracy caused by the automatic training is $\approx 4\%$. As expected, automatism causes a loss of performance, which is "the price to pay" to achieve a fully automatic real-time classification.

At the end, it is worth pointing out that, even if the selection of the appropriate pixels for synthesizing the 9-components representative vectors is performed in a supervised way, the classification method may be still considered unsupervised. Indeed, the selection of pixels is manual, but based on objective basis like the electromagnetic theory (polarimetric signatures, Pauli decomposition, etc.).

Examples of fully automatic classification methods for general polarimetric data are not found in literature, probably because the filter window size or some other parameters (i.e., number of reclustering cycles, percentage of pixels that change class between a reclustering cycle and the subsequent, etc.) are difficult to compute *a-priori*. The aim of this study is to design a new classification algorithm and to compare the obtained results with those obtained by commonly used methods, hence the Mixed Training method is used in the following. The PolSOM fully automatic classification capability can be seen as a further advantage of this algorithm compared with others.

[1] As the procedure is evolving, three classes were considered instead of four, because the starting main purpose is to optimize the method, focusing on the three principal scattering mechanisms.

3.3.5 AirSAR C–, L– and P–band polarimetric data classification with PolSOM

The best-performing PolSOM, i.e., the one obtained by the "mixed training" method has been employed to classify the selected AirSAR C– and P–band polarimetric images. Given the dependence of the backscattering of different types of surface on frequency, P–band data were separated into three classes only, while the C–band images into four classes. The classification of L-band data has already been considered in Sect. 3.3.4.1.2 and is recalled here just for a convenient comparison with the other bands.

P–band overall accuracy on three classes is 93.8 %, as shown in Fig. 3.41. Indeed, P–band is not able to discriminate between crops and vineyard. However, the three elemental scattering mechanisms (double-bounce, surface and volume) connected with the urban, crops and forest classes are well identified and correctly classified. As seen, L–band accuracy is 85.4 % on four classes. The confusion matrix was not computed for C–band since the accuracy is visibly low. In this case only rapeseed fields are clearly recognized, while other crop classes are confused. According to results in literature, e.g., [69], and the present PolSOM analysis, L–band fully polarimetric SAR data appear the best for land classification.

3.3.6 AirSAR C–, L– and P–band polarimetric data H/A/α–W classification and comparison

The AirSAR CM3151–L, –C and –P images have been classified also by the H/A/α–W method [11], outlined in Sect. (2.1.14). From an inspection of Figs. 3.44, 3.45 and 3.46 and of the corresponding confusion matrices it appears that the results yielded by the PolSOM technique are in each case at least comparable with those by the H/A/α–W method. It is also confirmed that the L–Band performs better for both classification methods.

As a final comment to this analysis, the neural algorithm trained by an electromagnetics-based methodology seems to perform consistently and looks a reliable tool for analyzing Earth Observation data.

3.3.7 RADARSAT-2 PolSOM classification

The RADARSAT–2 image was classified by the the same technique adopted for the AirSAR image, to confirm that PolSOM can process polarimetric data independently from the location (air or space) of the sensor platform.

As before, a mixed data set was synthesized from the polarimetric analysis of the image, which is in SLC format. No multilooking was applied to preserve the phase information [2]. RADARSAT–2 data are at C–band, which, as shown before, is not the best choice for complex landscapes classification. For that reason classification is limited to the three fundamental classes of double–bounce, surface and volume scattering. Fig. 3.47(b) shows a subset of RADARSAT–2 PolSOM classification result together with the Pauli image of the same area (Fig. 3.47(a)). The region of interest includes the Engineering Faculty of Tor Vergata University, Rome, Italy. Even if the speckle is very pronounced in the SLC image and affects the classification results, the overall three-class accuracy exceeds 69%. The spekle was not filtered because it was interesting to assess the classification accuracy in almost real-time situations, when filtering procedures are not easily performed.

3.3.8 RADARSAT–2 classification preserving polarimetric scattering characteristics and comparison with PolSOM

The RADARSAT–2 image has then been classified by the algorithm proposed by Lee in [14] and previously described in Sect. 2.1.15). Lee's algorithm preserves the purity of dominant polarimetric scattering properties for all pixels using a combination of scattering models based on the Freeman-Durden decomposition. After the first step, for each scattering category (double–bounce, volume and surface), a second classification is performed, but pixels in a scattering category are constrained to be classified together with other pixels in the same scattering category. This implies that the final classification accuracy is strongly dependent on the first step. The number

[2] In AirSAR MLC format case, multilooking was directly applied by JPL on data during the L1 processing phase, hence phase information was preserved

of classes is limited to three as before, for suitable comparison.

Fig. 3.48 reports a comparison between the two algorithm, including the respective accuracy matrices. PolSOM overall accuracy is 69.55% while Lee's algorithm overall accuracy is 68.83%. Again, as in the case of AirSAR, the results of the two methods are comparable. PolSOM perform similarly to well consolidated and used algorithms.

Gaussian Training

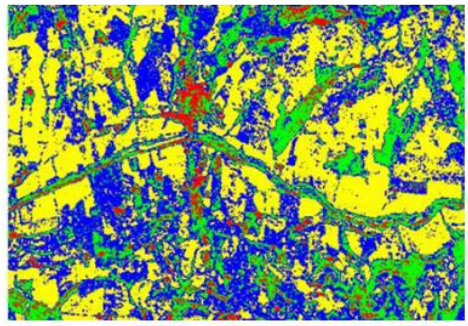

Overall Accuracy = (13926/16787) 82.96% Kappa Coefficient= 0.74				
	Ground Truth			
Class	Forest	Vineyards & Rape	Crops	Urban
Forest	80.38	4.76	1.30	25.51
Vineyards & Rape	7.16	78.86	10.17	2.48
Crops	0.00	16.38	88.51	0.00
Urban	12.45	0.00	0.02	72.01

(a) `Gaussian_Training`

Mixed Training

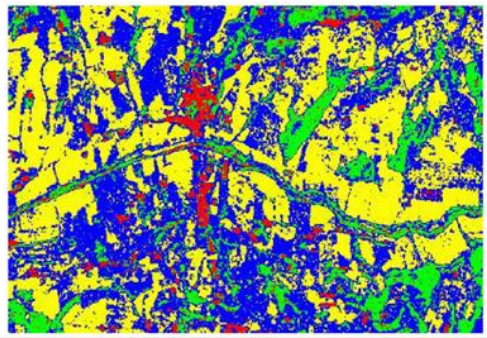

Overall Accuracy = (14338/16787) 85.4% Kappa Coefficient= 0.77				
	Ground Truth			
Class	Forest	Vineyards & Rape	Crops	Urban
Forest	84.02	2.67	0.41	18.95
Vineyards & Rape	12.77	84.81	10.60	8.26
Crops	0.00	12.51	88.93	0.00
Urban	3.22	0.00	0.06	72.78

(b) `Mixed_Training`

Figure 3.39: Comparison between accuracies obtained with Gaussian Training and Mixed Training.

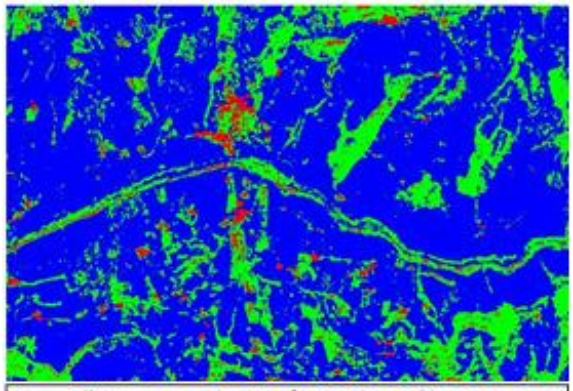

Overall Accuracy = (15679/16787) 93.4%
Kappa Coefficient= 0.82

	Ground Truth		
Class	**Crops**	**Forest**	**Urban**
Crops	97.61	9.13	7.77
Forest	2.38	86.77	21.98
Urban	0.01	4.10	70.25

Figure 3.40: L-Band Classification with automatic training.

P-Band

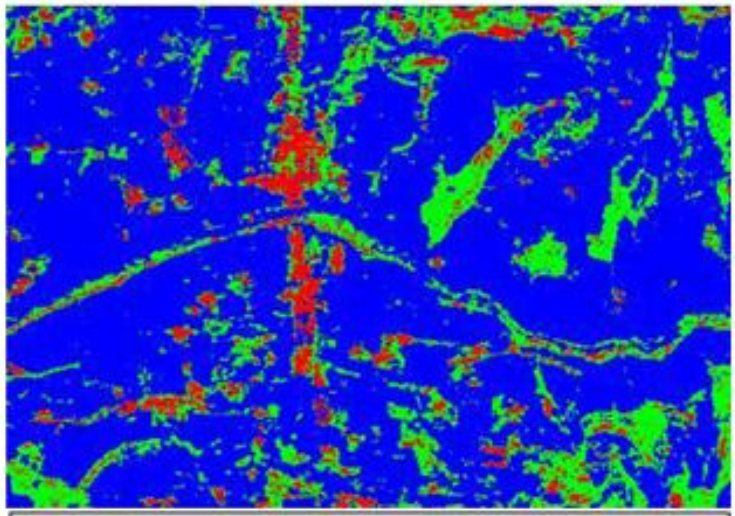

Overall Accuracy = (15746/16787) 93.8%
Kappa Coefficient= 0.83

	Ground Truth		
Class	**Forest**	**Crops**	**Urban**
Forest	82.93	0.44	19.06
Crops	5.09	98.38	8.15
Urban	11.99	1.18	72.78

Figure 3.41: P-Band PolSOM classification.

L-Band

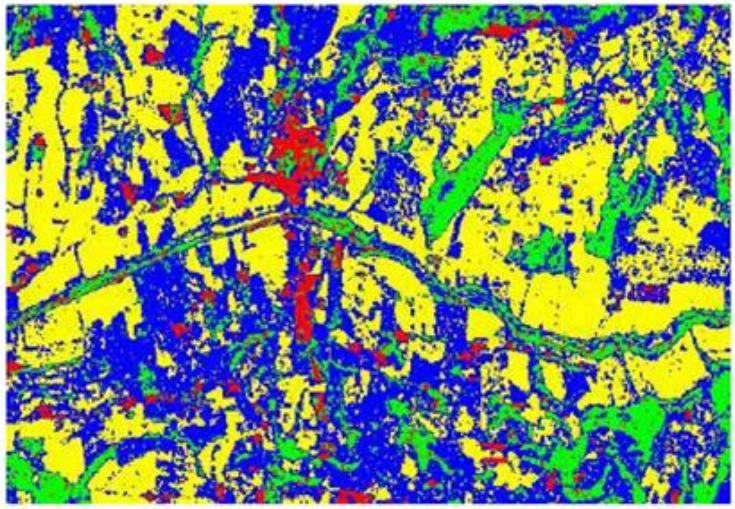

Overall Accuracy = (14338/16787) 85.4%
Kappa Coefficient= 0.77

	Ground Truth			
Class	**Forest**	**Vineyards & Rape**	**Crops**	**Urban**
Forest	84.02	2.67	0.41	18.95
Vineyards & Rape	12.77	84.81	10.60	8.26
Crops	0.00	12.51	88.93	0.00
Urban	3.22	0.00	0.06	72.78

Figure 3.42: L-Band PolSOM classification.

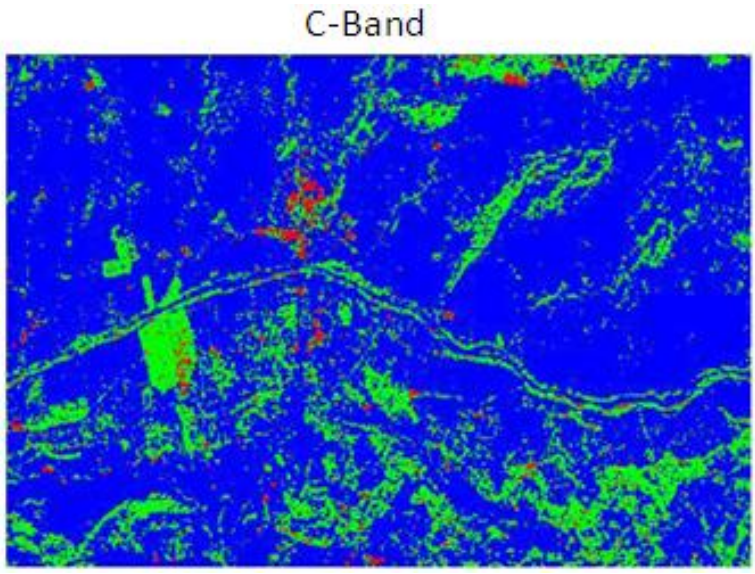

Figure 3.43: C–band SOM classification.

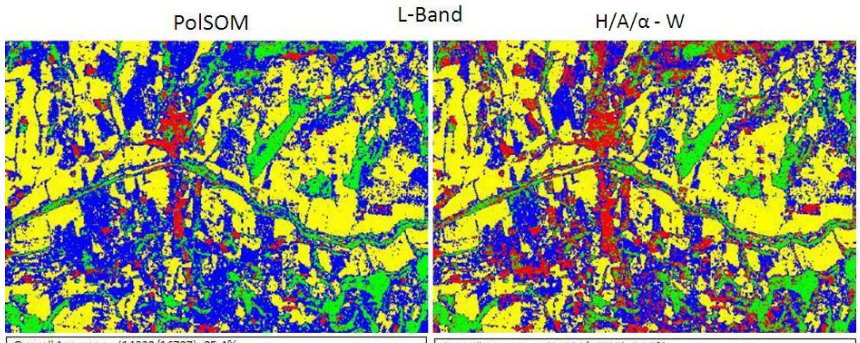

Overall Accuracy = (14338/16787) 85.4%
Kappa Coefficient= 0.77

	Ground Truth			
Class	Forest	Vineyards & Rape	Crops	Urban
Forest	84.02	2.67	0.41	18.95
Vineyards & Rape	12.77	84.81	10.60	8.26
Crops	0.00	12.51	88.93	0.00
Urban	3.22	0.00	0.06	72.78

Overall Accuracy = (14056/16787) 83.7%
Kappa Coefficient= 0.75

	Ground Truth			
Class	Forest	Vineyards & Rape	Crops	Urban
Forest	85.31	4.66	0.37	23.75
Vineyards & Rape	4.41	77.51	8.38	0.72
Crops	0.00	12.19	88.98	0.00
Urban	10.26	5.65	2.27	75.54

Figure 3.44: L–band PolSOM classification vs. H/A/α–W.

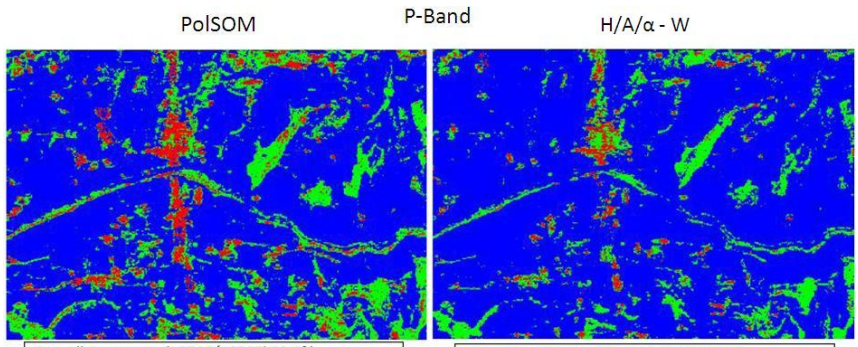

Overall Accuracy = (15746/16787) 93.8%
Kappa Coefficient= 0.83

	Ground Truth		
Class	**Forest**	**Crops**	**Urban**
Forest	82.93	0.44	19.06
Crops	5.09	98.38	8.15
Urban	11.99	1.18	72.78

Overall Accuracy = (15427/16787) 91.9%
Kappa Coefficient= 0.77

	Ground Truth		
Class	**Forest**	**Crops**	**Urban**
Forest	75.51	0.12	40.06
Crops	22.21	99.88	8.04
Urban	2.28	0.00	51.90

Figure 3.45: P-Band PolSOM classification vs. H/A/α–W.

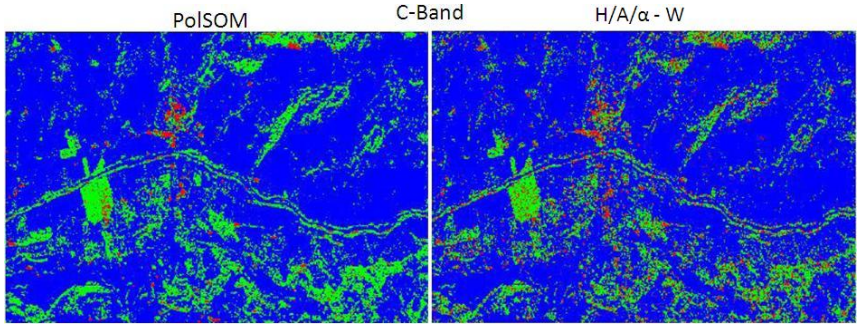

Figure 3.46: C-Band PolSOM classification versus H/A/α–W classification.

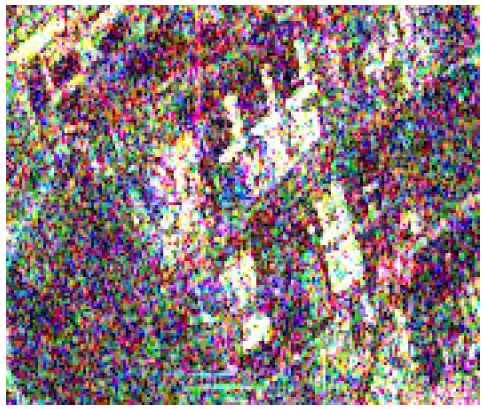

(a) `Pauli`

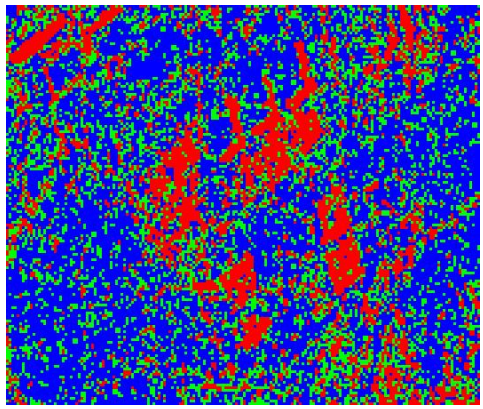

(b) `PolSOM_Classification`

Overall Accuracy = (5520/7937) 69.55% Kappa Coefficient= 0.45			
	Ground Truth		
Class	**Double Bounce**	**Surface**	**Volume**
Double Bounce	90.33	4.93	26.38
Surface	1.83	74.28	37.55
Volume	7.84	20.79	36.07

(c) `Confusion_Matrix`

Figure 3.47: RADARSAT–2 PolSOM Classification of the Engineering Faculty area of Tor Vergata University, Rome, Italy.

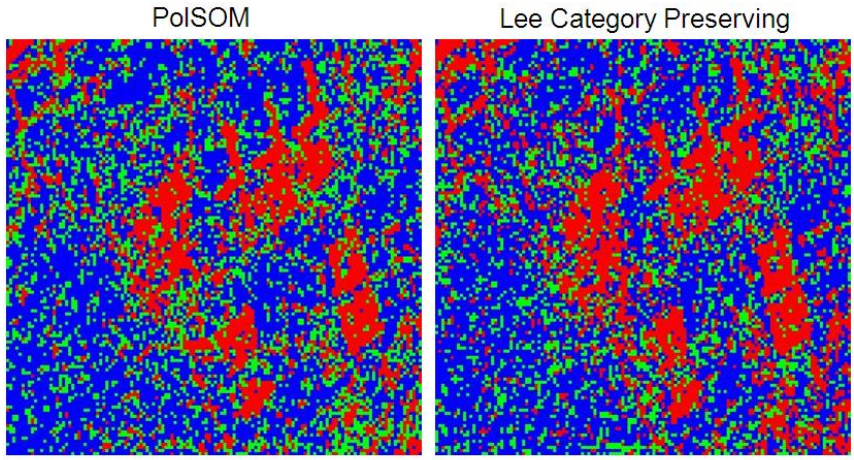

Overall Accuracy = (5520/7937) 69.55%
Kappa Coefficient= 0.45

	Ground Truth		
Class	**Double Bounce**	**Surface**	**Volume**
Double Bounce	90.33	4.93	26.38
Surface	1.83	74.28	37.55
Volume	7.84	20.79	36.07

Overall Accuracy = (5463/7937) 68.83%
Kappa Coefficient= 0.43

	Ground Truth		
Class	**Double Bounce**	**Surface**	**Volume**
Double Bounce	91.83	5.26	32.17
Surface	2.50	75.53	41.25
Volume	5.67	19.21	26.58

Figure 3.48: PolSOM RADARSAT–2 classification versus Lee category preserving classification (Freeman–Durden).

3.4 TexSOM

3.4.1 Introduction

With the term TexSOM we define a PolSOM using textural information, derived from the textural analysis of the polarimetric data. The term *textural information*, in the framework of TexSOM algorithm, assumes a wider meaning. Textural information, indeed, can be pixel based, like as other polarimetric approaches ([91]) or contextual. In this last case information is derived from data itself, mixing, at the same time, pixels and *objects*. The contextual analysis and the idea to mix together pixels and objects represents a new approach in polarimetric SAR data analysis, so far not yet proposed in the literature, at least at the writer's knowledge. The TexSOM approach is made possible by the peculiar ability of neural networks both in performing parallel computations and in jointly processing heterogeneous data. The modular approach followed in designing the TexSOM algorithm, also, does not impose restrictions on the number of input data and their nature. A TexSOM algorithm can classify a single polarimetric SAR scene, like others algorithms, or can process, without any need of substantial change in the algorithm, vectorial data, interferometric coherence data, etc.. From an application point of view, these characteristics provide substantial advantages, also because results of external processing and/or data from different sensors, can be integrated into a global polarimetric analysis.

In the following only AirSAR and RADARSAT–2 data are used and all other additional inputs are calculated starting from the images themselves. The aim is to compare the performances of TexSOM with PolSOM, and, in an indirect way, with presently used algorithms. However, it should be considered that, in general, multi–sensor or multi–data polarimetric processing can be performed by a TexSOM.

The activities pertaining to the TexSOM development are outlined in Tab. 3.3 and detailed in the next sections.

	Activity description	*Reference Section*
1.	AirSAR L–Band data pre–processing	3.4.2
2.	AirSAR L–Band data classification with TexSOM	3.4.3
3.	PolSOM and TexSOM AirSAR classification results comparison	3.4.5
4.	RADARSAT–2 data pre–processing and classification with TexSOM	3.4.5
5.	PolSOM and TexSOM RADARSAT–2 classification results comparison	3.4.6

Table 3.3: TexSOM activity scheme.

Figure 3.49: Shape discrimination.

3.4.2 AirSAR L–Band data pre–processing

Pixel–based and object–based information is used in the TexSOM polarimetric classification of AirSAR L–band data, as described in the following.

3.4.2.1 Object–Oriented methodology

When a skilled human operator analyses remote sensing data, he does not look only at the pixels, but also at the way they are organized.

An example of contextual information is given in Fig. 3.49. In a single-channel radar image, as an example, with roads, burned forest and burned fields, pixels with close values are associated with single objects. It is difficult

to classify single pixels in three separate classes, but the human brain readily recognizes the three different targets, since the objects are viewed in their totality and not one pixel at a time. To exploit the information provided by the object–based analysis, some rules must be found to create objects from the image and to take advantage from contextual information.

An *object* is defined as a set of adjacent pixels with common characteristics. The object can be distinguished from the others because there is a variation in the value associated with the pixels positioned on the boundaries of the object. The procedure that identifies the contours of the objects is the *image segmentation*. There are different algorithms that perform segmentation, a common technique consisting in growing filters that highlight pixels with common statistical characteristics. The growing procedure is more effective if the image is homogeneous with well delineated edges. Usually this is not the case of a radar image, where speckle affects both the contiguity of the edges and the homogeneity of the objects.

The segmentation of the image, hence the creation of objects, can be seen as an image processing for enhancing contrasts to better identify the edges. For this reason, some filtering was carried out on the AirSAR image before segmentation.

3.4.2.2 Refined Lee filtering

Lee filtering may be defined as a standard–deviation based filtering that processes data according to statistics computed within individual filter windows. Unlike a typical low–pass smoothing filter, the Lee filter preserves image sharpness and detail while reducing noise. The filtered pixel is replaced by a value calculated using the surrounding pixels [135]. The problem of Lee filtering of polarimetric images is that the window operates on a group of pixels, hence several scattering mechanisms are averaged in the resulting filtered pixel. This results in an increase of depolarization and, in turn, of the entropy (Sect. (2.1.14)) and of the height of the pedestal (Sect. (2.1.5)).

The Enhanced Lee filter [3] [62] is an adaptation of Lee filter and similarly

[3] [128] reports that speckle reduction is optimized if averaging over neighboring pixels

uses local statistics (coefficient of variation) within individual filter windows. Each pixel is assigned to one out of three classes, which are defined as [136]:

- Homogeneous: the pixel value is replaced by the average over the filter window;
- Heterogeneous: the pixel value is replaced by a weighted average;
- Point target: the pixel value is not changed.

Enhanced Lee filtering requires a damping factor and two cut–off parameters of the coefficient of variation . The damping factor inversely defines the extent of the exponential damping in the weighted average for the heterogeneous class, so that a larger damping factor produces less averaging. Value of 1 is suitable for most radar images. The coefficient of variation is inversely related to the square root of the number of looks of the original image. The cut–off parameters can be calculated by

$$C_u \cong \frac{0.523}{\sqrt{N}} \tag{3.2}$$

$$C_{max} \cong \sqrt{1 + \frac{2}{N}} \tag{3.3}$$

The Enhanced Lee filter was used to pre-process the AirSAR image, adopting a $[5 \times 5]$, which was found to be the best for this purpose.

The following parameters where used:

- Window size: 5×5;

(filtering window), yields a mean covariance matrix 2.40 in section 2.1.13 with Wishart distribution. This propriety is not possessed by the 4-look or 16-look CM3151 MLC images provided by JPL, since a polarimetric image should be, at least, 25–look averaged. In the development of PolSOM, experiments were carried out with filtered images, but without noting appreciable increase of accuracy. The reason is that neural networks perform parallel processing, hence they are more robust to noisy and corrupted data [23]. Therefore, it was decided to avoid filtering before PolSOM classification, also to design an algorithm as automatic as possible.

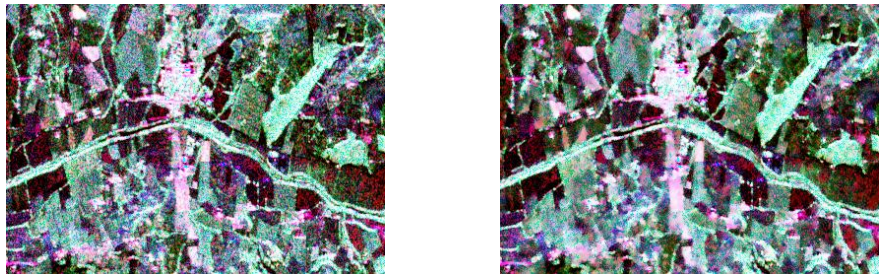

(a) `PauliImage` (b) `PauliFilteredImage`

Figure 3.50: Comparison between unprocessed Pauli image and Enaced–Lee filtered Pauli image.

- Dumping Factor: 1;
- $C_u = 0.138$;
- $C_{max} = 1.06$;

As an example, Fig. 3.50 shows a comparison between the Pauli image synthesized from unprocessed data and the Pauli image synthesized from filtered data. The 9-dimensions (principal polarizations) filtered image is the input to the segmentation algorithm.

3.4.2.3 Segmentation

First major progress in object–oriented feature extraction is found in sea–ice studies [137], coastline extraction [138] and certain approaches to data compaction [139]. As shown in Sect. 3.3.3) the full polarimetric radar properties can be expressed by the backscattering intensities at nine principal polarizations. This approach has the advantage that segmentation can be performed by using non–polarimetric algorithms [134]. For this reason, TexSOM implements the general–purpose algorithm described in [140].

The algorithm, a multi–resolution segmentation [141] which basically combines different procedures, requires a scale parameter, related to the

dimension of the objects, hence to the classification scale. The segmentation procedure starts at any point in the image with *one-pixel objects*. In the subsequent steps, smaller objects are merged into bigger ones according to some parameters (Color, Shape, Smoothness and Compactness) and the common statistical properties of the objects. The clustering procedure ends when the growth of the objects exceeds a threshold defined by the scale parameter. Color, Shape, Smoothness and Compactness are connected together in the pairs Color-Shape and Smoothness-Compactness, respectively, with the property that if, for example, the Color parameter is increased, then Shape correspondingly decreases. The success of segmentation relies on the correct setting of the parameters. However, their optimization is not a problem when radar images are at hand, since, given the highly fragmented nature of SAR images, Shape must assume its maximum value and, consequently, Color the minimum. On their side, the setting of Smoothness-Compactness does not dramatically affect the result. The scale parameter was determined by considering the scale of interest, based on the results obtained by PolSOM on the same area[4].

Fig. 3.51 reports the result of the segmentation. It turns out that the pixel information is lost and the original raster input file transforms into a vectorial one. The colors refer to the identification number of the objects in the related attribute table discussed in the next section.

3.4.2.4 Object–based information

The segmentation procedure creates a *polygon* vector file in which each polygon is associated with an object, a row corresponds to the polygon and each field of that row represents a feature of the object. In this way an attribute table is created, in which rows denote objects and columns identify features.

An important point is understanding which features contained in the vector file carry pieces of information that can improve the SOM accuracy.

[4]The scale parameter, or growth threshold, must be set in most clustering algorithms. Indeed, H/A/α–W algorithm uses a cluster threshold in the Wishart clustering procedure (Sect. 2.1.14).

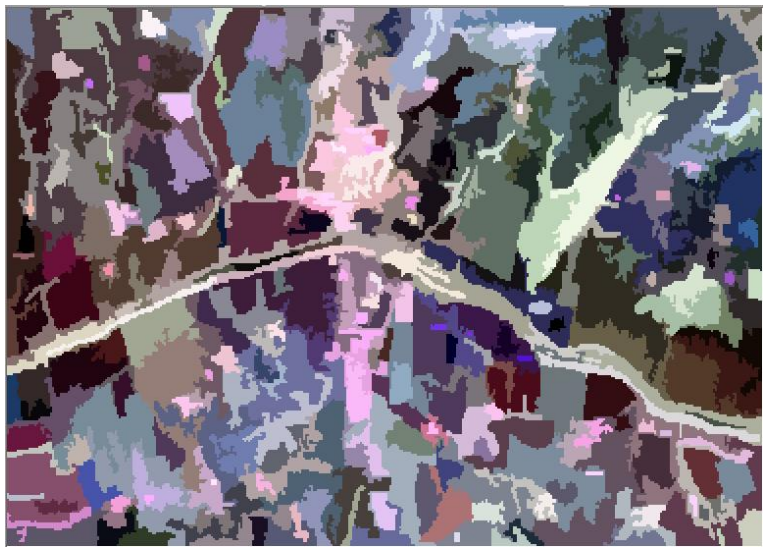

Figure 3.51: Segmentation result.

Many features can be computed, but those strictly affected by the kind of image under analysis should be avoided. The used optimization procedure takes into account the following constraints:

- processing time;
- independence from the image under analysis;
- features independence.

Four features were identified, three based on shape parameters and one on textural information.

3.4.2.4.1 Shape–based features. An example of sets of pixels having the same value but ordered differently in space was shown in Fig. 3.49. When the geometry is associated with an object, discrimination among objects is feasible from the shape properties. As an example, the geometry

of a road is quite different from that of a field. Both objects are represented by rectangles, but a road has the "width" to "length" ratio with very low or very high values, according to its orientation in the image. A field, on the contrary, has width of the same order of its length. As a further example, in a forest stand, the border is more fragmented than that of a building or of a field.

The shape–based features selected for the TexSOM implementation are:

- Area: this feature represents the area of the image object itself, be it the real area in square meters or the number of the pixels contained in the object.

- Length/width: a bounding box is constructed around the object, from which the ratio of length to width is calculated.

- Shape index: it describes the smoothness of the image object border. The more fractal an object appears, the higher its shape index is. Mathematically, the shape index is the length of the border e divided by four times the square root of its area A

$$SI = e/4\sqrt{A} \tag{3.4}$$

  where the border length e is defined as the sum of the lengths of the edges of the object .

Fig. 3.53 shows a simple example of shape–based feature values for two different objects[5]. Note that the number of pixels in the area is the same for both objects, hence discrimination cannot be based on this single parameter. If the vector–to–raster procedure is applied, two different four–elements vectors are obtained. All pixels of one object are characterized by the same feature vector, hence, the discrimination between the entire objects is straightforward.

[5]The area was computed as the number of pixels.

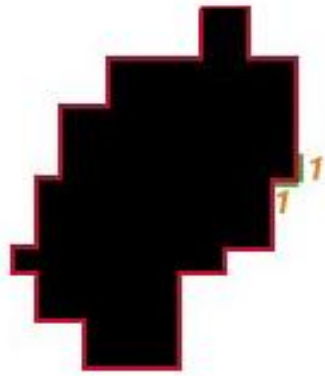

Figure 3.52: Border length.

Figure 3.53: Shape–based features.

3.4.2.4.2 Texture–based feature. The approach to textural features calculation is quite different. Textural information is computed through the occurrence–based filter on a single image file [142]. The chosen image was the AirSAR L–Band total power Image (Eq. 3.1) [6]. The computation was performed using only pixels surrounded by the border of the each object, In particular, the mean occurrence–based filter was used [142] with a $[3 \times 3]$ window, since the data are MLC. At the end, the sum of the values of the pixels belonging to each object was assigned to it.

3.4.3 AirSAR L–Band data classification by TexSOM

The peculiar design of TexSOM makes the algorithm able to jointly process polarimetric and textural information, without particular limitations to the kind or number of inputs. TexSOM can be defined as a multi–neural network algorithm, which enhances the parallel–calculation properties of the net. As mentioned before, only a limited selection of images was used in this work, to be able to compare the TexSOM results against those of other methods, but, thanks to its modular design, the algorithm is indeed able to process a variety of images.

[6] The quantities in Eq. (3.1) are related to power, hence the Total Power image can be also regarded as the image of the *SPAN* of the $[\mathbf{T}]_{3\times3}$ matrix of Eq. (2.43). Ideed, since $[\mathbf{T}]_{3\times3}$ is an Hermitian positive semidefinite matrix,

$$[\mathbf{T}]_{3\times3} = \lambda_1 \mathbf{e}_1 \cdot \mathbf{e}_1^{*T} + \lambda_2 \mathbf{e}_2 \cdot \mathbf{e}_2^{*T} + \lambda_3 \mathbf{e}_3 \cdot \mathbf{e}_3^{*T} \tag{3.5}$$

The *SPAN* can be defined as the total backscattered power contributed by the three scattering mechanism in $[\mathbf{T}]_{3\times3}$:

$$SPAN = \lambda_1 + \lambda_2 + \lambda_3 \tag{3.6}$$

The sum of the eigenvalues in Eq. (3.6) is the trace of the coherency matrix $[\mathbf{T}]_{3\times3}$ [72]; hence, the *SPAN* can be also defined as:

$$SPAN = T_{11} + T_{22} + T_{33} \;\; where \;\; \begin{cases} T_{11} = |S_{hh} + S_{vv}|^2 \\ T_{22} = |S_{hh} - S_{vv}|^2 \\ T_{33} = |2S_x|^2 \end{cases} \tag{3.7}$$

with T_{ii} (i=1,2,3) the principal diagonal elements of the coherency matrix $[\mathbf{T}]_{3\times3}$.

A first problem in managing heterogeneous data derives from the statistics of the different inputs, which can span quite different ranges. The procedure commonly followed consists in scaling the data to obtain range–controlled inputs statistics. This procedure cannot be applied to polarimetric data, because inter–channel polarimetric information would be lost. The second problem comes from the object–based data, that require pre–processing before feeding the network. As mentioned before, this latter problem was solved by implementing a raster–to–vector conversion. To solve the first problem, a new net architecture was designed.

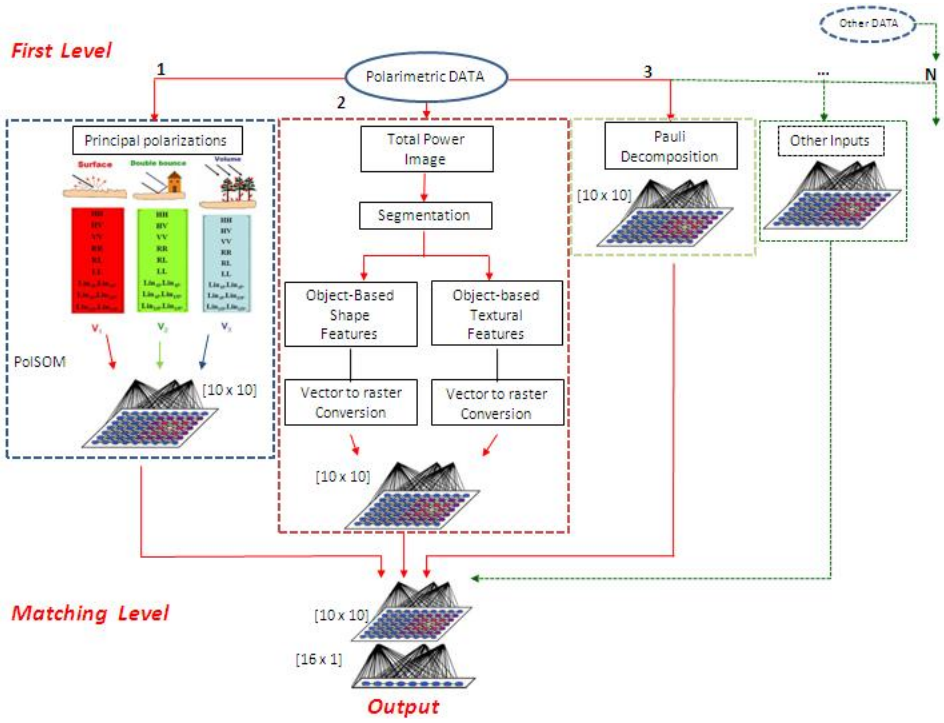

Figure 3.54: TexSOM layout.

The scheme in Fig. 3.54 shows the assemblage of different SOMs for

the classification process. A first polarimetric input enters a PolSOM, as described in Sect. (3.3)). The second input carries object–based information, i.e., the total power image synthesized and subsequently segmented and vector–to–raster converted. As noted, the number of inputs to a TexSOM is theoretically unlimited and for this reason other inputs were considered. We tested several configurations with up to six primary inputs, like the diagonal elements of the covariance matrix $[T]_{3\times3}$, H/A/α–W parameters, Freeman–Durden decomposition, etc.. By comparing the overall accuracy matrices, it turned out that the best result was obtained using a three first–level SOM configuration with inputs including, in addition to polarimetric intensities and total power, the Pauli decomposition. All the first–level SOMs are $[10 \times 10]$, since the results of the tests indicate this configuration as the best trade off among accuracy, processing times and independence of the number of neurons from the input[7].

The outputs from all first–level SOMs are fed into a matching–level SOM, which represents the *core* SOM. Indeed, this is the SOM that performs the classification of heterogeneous information. All the inputs fed into core SOM range in a $[0, 99]$ interval, since they are originated by $[10 \times 10]$ SOMs, but the inter–channel polarimetric information is not lost, because, in the first step, homogeneous information are processed in independent SOMs.

The output of the $[10 \times 10]$ core SOM is a 100 class segmentation. To reduce this unreasonably high number of classes and grouping together pixels belonging to close or to the same class, a further 16×1 SOM is used, whose output is the final output of the algorithm.

Fig. 3.55 reports the result obtained in classifying the L-band AirSAR image already used for PolSOM classification. The overall accuracy now exceeds 89%, with an apparent improvement in the separability of particular classes, such as urban and forest, vineyards/rapeseed and other crops. Again, the neural networks have provided an optimal algorithm for managing

[7] Up to 100 classes can be discriminated by a $[10\times10]$ SOM. This number is substantially over sized, considering the number of classes usually present in an image, for this reason the same SOM topology can be applied regardless of the input image. On the other hand, $[10 \times 10]$ topology represents the smallest configuration needed to correctly monitor the network evolution by U-Matrix.

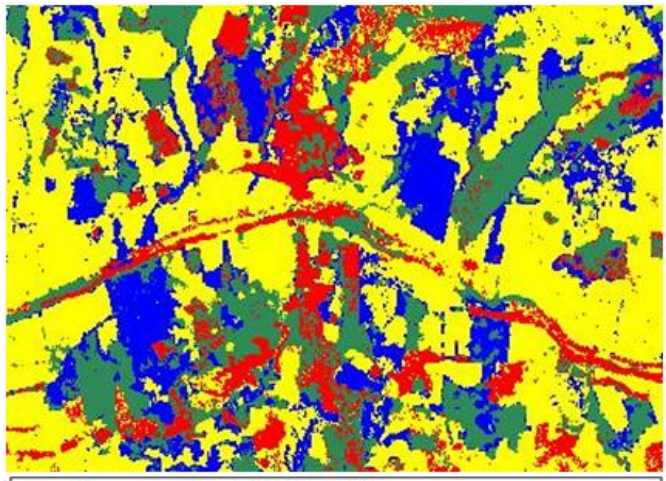

Overall Accuracy = (14991/16787) 89.3%
Kappa Coefficient= 0.83

	Ground Truth			
Class	**Forest**	**Vineyards & Rape**	**Crops**	**Urban**
Forest	86.45	3.12	0.77	12.42
Vineyards & Rape	7.68	84.84	5.98	4.06
Crops	1.08	12.04	93.02	0.38
Urban	4.79	0.00	0.23	83.14

Figure 3.55: TexSOM Classification result.

heterogeneous data in classification.

3.4.4 PolSOM and TexSOM AirSAR classification: results comparison

If the results in classifying the AirSAR polarimetric L–band data yielded by TexSOM are compared with those by PolSOM (Fig. 3.56), the following considerations hold. TexSOM yielded an improvement of 3.9% over PolSOM: this increase of accuracy is particularly significant, given the high absolute value. It was also noted that, in particular, TexSOM benefits from the relatively stable information provided by the "object–based" input.

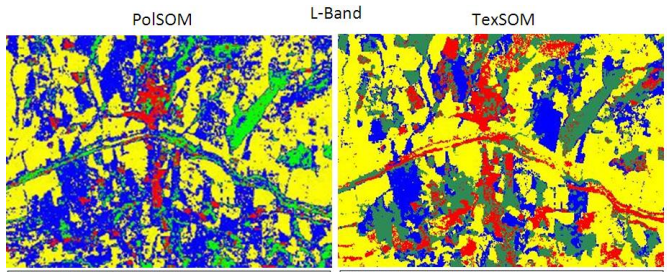

Overall Accuracy = (14338/16787) 85.4%
Kappa Coefficient= 0.77

	Ground Truth			
Class	Forest	Vineyards & Rape	Crops	Urban
Forest	84.02	2.67	0.41	18.95
Vineyards & Rape	12.77	84.81	10.60	8.26
Crops	0.00	12.51	88.93	0.00
Urban	3.22	0.00	0.06	72.78

Overall Accuracy = (14991/16787) 89.3%
Kappa Coefficient= 0.83

	Ground Truth			
Class	Forest	Vineyards & Rape	Crops	Urban
Forest	86.45	3.12	0.77	12.42
Vineyards & Rape	7.68	84.84	5.98	4.06
Crops	1.08	12.04	93.02	0.38
Urban	4.79	0.00	0.23	83.14

Figure 3.56: PolSOM and TexSOM results comparison.

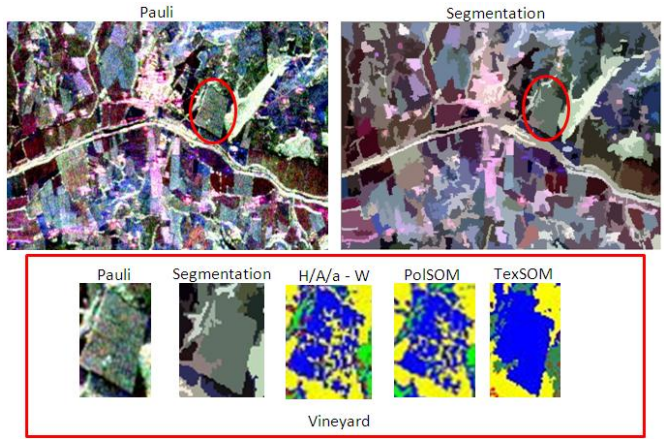

Figure 3.57: Object–based contribution in vineyard classification.

At this purpose, the particular vineyard area highlighted on the image shown in Fig. 3.57 can be considered. The five sub–images refer to (starting form the left): the Pauli image, the segmentation result, the H/A/α–W classification, the PolSOM classification and TexSOM classification. It can be noted that in vineyard classified by TexSOM, thanks to "object–based"

inputs, noise is reduced and the accuracy increased.

3.4.5 RADARSAT–2 data pre–processing and classification

As explained in Sect. 3.3.7 the classification of RADARSAT–2 data was performed on three scattering classes: double–bounce, surface, and volume. The TexSOM scheme used for this classification is shown in Fig. 3.58. In

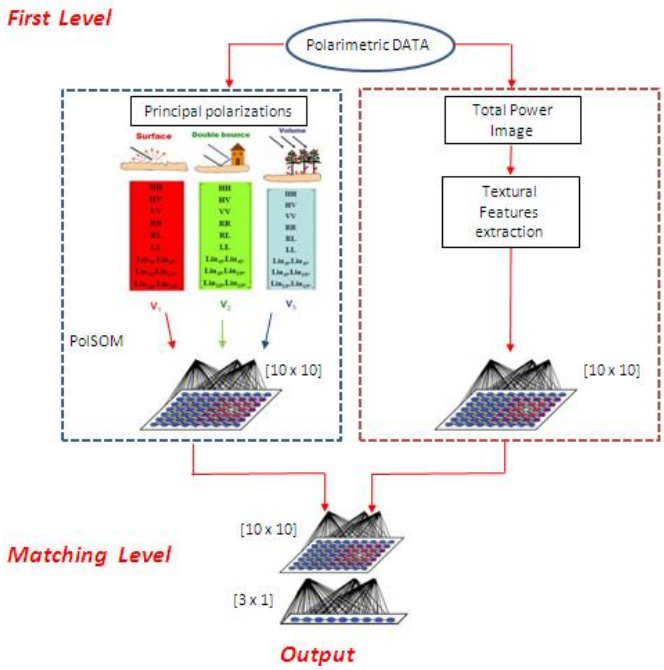

Figure 3.58: TexSOM RADARSAT–2 scheme.

channel 2, from the total power image, a pixel–based textural information has been computed by $[3 \times 3]$, $[5 \times 5]$ and $[7 \times 7]$ filtering windows. As before, textural informations is processed by a dedicated SOM whose output feeds the core SOM jointly with the output of the channel 1 PolSOM unit. Unlike the AirSAR classification, in this case the object–based information has not

been used, since the RADARSAT–2 image is SLC in slant-range geometry.

(a) `Pauli`

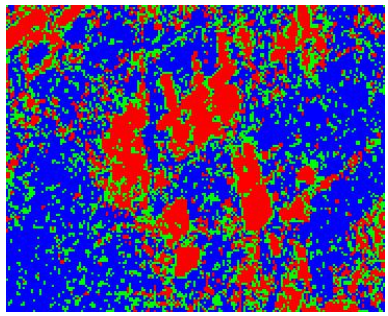

(b) `TexSOM_Classification`

Overall Accuracy = (6012/7937) 75.75%
Kappa Coefficient= 0.54

	Ground Truth		
Class	**Double Bounce**	**Surface**	**Volume**
Double Bounce	99.08	2.57	29.81
Surface	0.00	82.10	35.73
Volume	0.92	15.33	34.45

(c) `Confusion_Matrix`

Figure 3.59: RADARSAT–2 TexSOM classification of the Tor Vergata University Engineering area, Rome, Italy.

The classification result is shown in Fig. 3.59, with the corresponding accuracy matrix.

3.4.6 PolSOM and TexSOM RADARSAT–2 classification: results comparison

Fig. 3.60 shows a comparison between the PolSOM and TexSOM performances in classifying the selected Tor Vergata area, including the accuracy matrices. TexSOM increases the accuracy by 6.2% over PolSOM. In particular, it is worth noticing how the use of texture features reduces the classification fragmentation that strongly affects the segmentation of such an unfiltered SLC image.

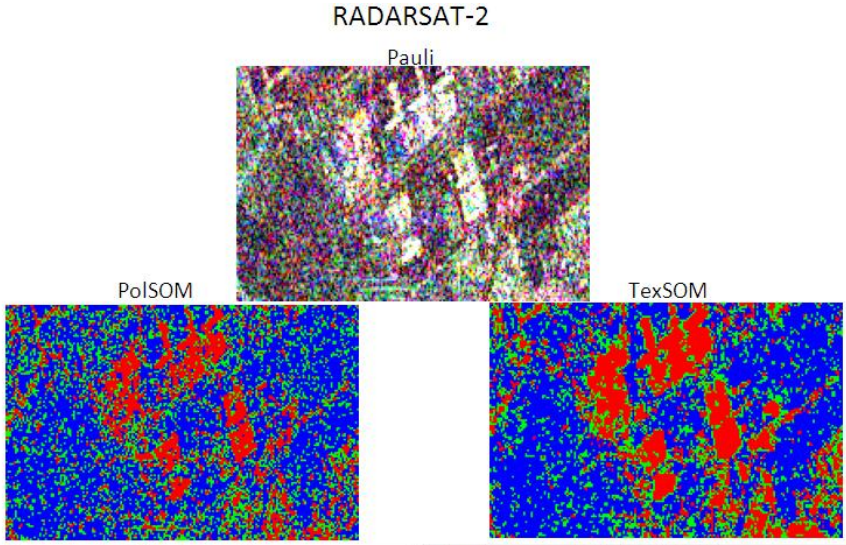

Overall Accuracy = (5520/7937) 69.55%
Kappa Coefficient= 0.45

	Ground Truth		
Class	**Double Bounce**	**Surface**	**Volume**
Double Bounce	90.33	4.93	26.38
Surface	1.83	74.28	37.55
Volume	7.84	20.79	36.07

Overall Accuracy = (6012/7937) 75.75%
Kappa Coefficient= 0.54

	Ground Truth		
Class	**Double Bounce**	**Surface**	**Volume**
Double Bounce	99.08	2.57	29.81
Surface	0.00	82.10	35.73
Volume	0.92	15.33	34.45

Figure 3.60: TexSOM and PolSOM classification results on Engineering Faculty of Tor Vergata University, Rome, Italy.

Chapter 4

Conclusions

Two novel Neural Network algorithms, named PolSOM and TexSOM, based on the Self-Organizing Map (SOM) technique, have been devised, developed and implemented to classify polarimetric radar images in an unsupervised manner. For the first time at the author's knowledge, pixel–based and object–based information has been merged together and jointly used in classification. A Neural Network scheme was instrumental in this major progress, given its natural ability in managing heterogeneous information.

The classification algorithms have been tested on two Italian landscapes, particularly challenging because of the undulating, heterogeneous and fragmented landscapes. Both L-band airborne (AirSAR) and and C-band space borne (RADARSAT-2) fully polarimetric SAR images formed the data set on which the two algorithms were validated. Their performance was also checked against the results yielded by some presently popular classification algorithms, as the Lee's/Freeman–Durden and the Cloude and Pottier H/A/α-Wishart ones.

The obtained confusion matrices show that the accuracies attained by the novel algorithms are at least comparable with those achieved by the methods that are now considered to be the best performers in classifying polarimetric SAR data.

Given their difficult-to-track nonlinear behavior and based on results obtained in the early stage of their implementation, Neural Networks are sometimes considered a kind of occasionally effective, but substantially unreliable black-box algorithms. The experience gained in designing and implementing the algorithms demonstrates that when the topological configuration and the training strategy are driven by essentially physical consideration, the Neural Network algorithm behaves in a controlled fashion and its results are stable.

In the next future, multi-polarization (i.e. Sentinel–1) and optical (i.e. Sentinel–2) European missions are scheduled, which are expected to provide a huge amount of data, also thanks to improved revisit rates. The availability of unsupervised algorithms to automatically exploit the ensemble of satellite data in updating the land cover maps is one of the crucial factors towards consolidating the success of Earth Observation. The ability of the proposed TexSOM algorithm in unsupervised processing SAR data [143], SAR and optical data [144], raster and vectorial data (Sect. (3.4.2)), hints at the versatility of the algorithm, which is not bounded to SAR polarimetry only, like the ones previously considered in this work, and at its potential in possibly contributing to the success of satellite Earth Observation.

Appendix A

AirSAR data compression/decompression equations

Stating the following expression for the Stokes matrix [**M**]:

$$[\mathbf{M}] = \begin{bmatrix} M_{11} & M_{12} & M_{13} & M_{14} \\ M_{21} & M_{22} & M_{23} & M_{24} \\ M_{31} & M_{32} & M_{33} & M_{34} \\ M_{41} & M_{42} & M_{43} & M_{44} \end{bmatrix} \tag{A.1}$$

in the monostatic case, the matrix is real and symmetric, therefore [**M**] contains the following distinct elements:

$$\begin{aligned}
M_{11} &= \tfrac{1}{4}(S_{hh}S_{hh}^* + S_{vv}S_{vv}^* + 2S_{hv}S_{hv}^*) \\
M_{12} &= \tfrac{1}{4}(S_{hh}S_{hh}^* - S_{vv}S_{vv}^*) \\
M_{13} &= \tfrac{1}{2}\Re(S_{hh}S_{hv}^*) + \tfrac{1}{2}\Re(S_{hv}S_{vv}^*) \\
M_{14} &= -\tfrac{1}{2}\Im(S_{hh}S_{hv}^*) - \tfrac{1}{2}\Im(S_{hv}S_{vv}^*) \\
M_{22} &= \tfrac{1}{4}(S_{hh}S_{hh}^* + S_{vv}S_{vv}^* - 2S_{hv}S_{hv}^*) \\
M_{23} &= \tfrac{1}{2}\Re(S_{hh}S_{hv}^*) - \tfrac{1}{2}\Re(S_{hv}S_{vv}^*) \\
M_{24} &= -\tfrac{1}{2}\Im(S_{hh}S_{hv}^*) + \tfrac{1}{2}\Im(S_{hv}S_{vv}^*) \\
M_{33} &= \tfrac{1}{2}(S_{hv}S_{hv}^*) + \tfrac{1}{2}\Re(S_{hh}S_{vv}^*) \\
M_{34} &= -\tfrac{1}{2}\Im(S_{hh}S_{vv}^*) \\
M_{44} &= \tfrac{1}{2}(S_{hv}S_{hv}^*) - \tfrac{1}{2}\Re(S_{hh}S_{vv}^*)
\end{aligned} \tag{A.2}$$

From Eq. (A.1) and Eq. (A.2) following equation can be obtained:

$$M_{11} = M_{22} + M_{33} + M_{44} \tag{A.3}$$

which shows that only nine parameters are needed to derive [**M**] matrix, the tenth is connected to the Eq. (A.3). Storing of previous parameters on magnetic media require, for each 16-look matrix Stokes, the use of 36 bytes, as each parameter needs 4 bytes. But 36 bytes are reduced to 10, using a special compression algorithm, that uses the following rules:

$$byte(1) = INT(\log_2 M_{11}) \tag{A.4}$$

$$byte(2) = INT\left[254\left(\frac{M_{11}}{2^{byte(1)}} - 1.5\right)\right] \tag{A.5}$$

$$byte(3) = INT\left(127\,\frac{M_{12}}{x}\right) \tag{A.6}$$

$$byte(4) = INT\left[127\,SIGN\left(\frac{M_{13}}{x}\right)\sqrt{\frac{M_{13}}{x}}\right] \tag{A.7}$$

$$byte(5) = INT\left[127\, SIGN\left(\frac{M_{14}}{x}\right)\sqrt{\frac{M_{14}}{x}}\right] \tag{A.8}$$

$$byte(6) = INT\left[127\, SIGN\left(\frac{M_{23}}{x}\right)\sqrt{\frac{M_{23}}{x}}\right] \tag{A.9}$$

$$byte(7) = INT\left[127\, SIGN\left(\frac{M_{24}}{x}\right)\sqrt{\frac{M_{24}}{x}}\right] \tag{A.10}$$

$$byte(8) = INT\left(127\,\frac{M_{33}}{x}\right) \tag{A.11}$$

$$byte(9) = INT\left(127\,\frac{M_{34}}{x}\right) \tag{A.12}$$

$$byte(10) = INT\left(127\,\frac{M_{44}}{x}\right) \tag{A.13}$$

where x is a normalization factor:

$$x = \left(\frac{byte(2)}{254} + 1.5\right) 2^{byte(1)} \tag{A.14}$$

The equations needed to reconstruct the elements of the Stokes matrix are:

$$M_{11} = \left(\frac{byte(2)}{254} + 1.5\right) 2^{byte(1)} \tag{A.15}$$

$$M_{12} = byte(3)\,\frac{M_{11}}{127} \tag{A.16}$$

$$M_{13} = SIGN\left[byte(4)\right]\left(\frac{byte(4)}{127}\right)^2 M_{11} \tag{A.17}$$

$$M_{14} = SIGN\left[byte(5)\right]\left(\frac{byte(5)}{127}\right)^2 M_{11} \tag{A.18}$$

$$M_{23} = SIGN\left[byte(6)\right]\left(\frac{byte(6)}{127}\right)^2 M_{11} \tag{A.19}$$

$$M_{24} = SIGN\left[byte(7)\right]\left(\frac{byte(7)}{127}\right)^2 M_{11} \tag{A.20}$$

$$M_{13} = byte(8)\,\frac{M_{11}}{127} \tag{A.21}$$

$$M_{34} = byte(9)\,\frac{M_{11}}{127} \tag{A.22}$$

$$M_{44} = byte(10)\,\frac{M_{11}}{127} \tag{A.23}$$

$$M_{22} = M_{11} - M_{33} - M_{44} \tag{A.24}$$

Bibliography

[1] W. Boerner, A.-Q. Yan, and Y. Yamaguchi, "On the basic principles of radar polarimetry: the target characteristic polarization state theory of kennaugh, huynens polarization fork concept, and its extension to the partially polarized case," in *Proc. IEEE*, vol. 79, pp. 1538–1550, 1991.

[2] J. Van Zyl, "Unsupervised classification of scattering behavior using radar polarimetry data," *IEEE Trans. Geosci. Remote Sensing*, vol. 27, pp. 36–45, 1989.

[3] S. Chandrasekhar, *Radiative Transfer.* Dover, 1960.

[4] J. Huynen, *Phenomenological Theory of Radar Targets.* PhD thesis, University, Delft, The Netherlands, 1970.

[5] W. L. Cameron and L. K. Leung, "Feature motivated polarization scattering matrix decomposition," RECORD IEEE 1990 in Proc. IEEE Int. Radar Conf,, 1990.

[6] E. Krogager, "A new decomposition of the radar target scattering matrix," *Electron. Lett.*, vol. 26, pp. 1525–1526, 1990.

[7] A. Freeman and S. Durden, "A three–component scattering model

for polarimetric SAR data," *IEEE Trans. Geosci. Remote Sensing*, vol. 36, pp. 963–973, 1998.

[8] R. Touzi, "Target scattering decomposition in terms of roll-invariant target parameters," *IEEE Trans. Geosci. Remote Sensing*, vol. 45, pp. 73–84, 2007.

[9] S. R. Cloude, "Group theory and polarisation algebra," *Optik*, vol. 75, pp. 26–36, 1986.

[10] S. R. Cloude, "Lie groups in electromagnetic wave propagation and scattering," *J. Electromag. Waves Appl.*, vol. 6, pp. 947–974, 1992.

[11] S. Cloude and E. Pottier, "An entropy based classification scheme for land applications of polarimetric SAR," *f Trans. Geosci. Remote Sensing*, vol. 35, pp. 68–78, 1997.

[12] E. Pottier, "The H/A/α polarimetric decomposition approach applied to POLSAR data processing," in Proceedings of the PIERS – Workshop on Advances in Radar Methods, 1998.

[13] J. Lee, M. Grunes, T. Ainsworth, L. Du, D. Schuler, and S. Cloude, "Unsupervised classification using polarimetric decomposition and the complex wishart classifier," *IEEE Trans. Geosci. Remote Sensing*, vol. 37, pp. 2249–2258, 1999.

[14] J. Lee, M. Grunes, E. Pottier, and L. Ferro-Famil, "Unsupervised terrain classification preserving polarimetric scattering characteristics," *IEEE Trans. Geosci. Remote Sensing*, vol. 42, pp. 722–731, 2004.

[15] L. Du and J. Lee, "Fuzzy classification of earth terrain covers using multi-look polarimetric SAR image data," *Int. J. Remote Sensing*, vol. 17, pp. 809–826, 1996.

[16] U. Benz, "Supervised fuzzy analysis of single– and multi–channel SAR data," *IEEE Trans. Geosci. Remote Sensing*, vol. 37, pp. 1023–1037, 1999.

[17] P. Kersten, J. Lee, and T. Ainsworth, "Unsupervised classification of polarimetric synthetic aperture radar images using fuzzy clustering and em clustering," *IEEE Trans. Geosci. Remote Sensing*, vol. 43, pp. 519–527, 2005.

[18] S. Park and W. Moon, "Unsupervised classification of scattering mechanisms in polarimetric SAR data using fuzzy logic in entropy and alpha plane," *IEEE Trans. Geosci. Remote Sensing*, vol. 45, pp. 2652–2664, 2007.

[19] A. Baraldi and F. Parmiggiani, "A neural network for unsupervised categorization of multivalued input pattern: an application to satellite image clustering," *IEEE Trans. Geosci. Remote Sensing*, vol. 33, pp. 305–316, 1995.

[20] F. Pacifici, F. Del Frate, C. Solimini, and W. Emery, "An innovative neural-net method to detect temporal changes in high-resolution optical satellite imagery," *IEEE Trans. Geosci. Remote Sensing*, vol. 45, pp. 2940–2952, 2007.

[21] E. Pottier and J. Saillard, "On radar polarization target decomposition theorems with application to target classification, by using neural network method," Seventh International Conference on (IEE) Antennas and Propagation. ICAP 91., 1991.

[22] M. Hellmann, "A new approach for interpretation of SAR-data using polarimetric techniques," Proceedings on Geoscience and Remote Sensing Symposium. IGARSS '98, 1998.

[23] T. Kohonen, *Self-Organizing Maps*. Springer, 2001.

[24] Y. Hara, R. Atkins, S. Yueh, R. Shin, and J. Kong, "Application of neural networks to radar image classification," *IEEE Trans. Geosci. Remote Sensing*, vol. 32, pp. 100–109, 1994.

[25] Y. Ito and S. Omatu, "A polarimetric SAR data classification method using neural networks," IEEE International Geoscience and Remote Sensing Symposium. IGARSS'98, 1998.

[26] E. Pottier, "Radar target decomposition theorems and unsupervised classification of full polarimetric SAR data," IEEE International Geoscience and Remote Sensing Symposium. IGARSS'94, 1994.

[27] K. Khan and Y. Jian, "Unsupervised classification of polarimetric SAR images by Gamma–Correction of features using self organizing map," International Symposium on Microwave, Antenna, Propagation, and EMC Technologies For Wireless Communications, 2007.

[28] W. Boerner, *Polarimetry in radar remote sensing. Basic and applied concepts, in Manual of Remote Sensing: Principles and Applications of Imaging Radar.* F. M. Henderson and A. J. Lewis, eds., vol. 8, ch. 5, Wiley, 3 ed., 1998.

[29] G. Sinclair, "The transmission and reception of elliptically polarized waves," in *Proc. IRE*, pp. 148–151, 1950.

[30] E. Kennaugh, *Polarization properties of radar reflection.* PhD thesis, The Ohio State University, Columbus, OH, USA, 1952.

[31] V. Rumsey, "Part i: Transmission between elliptically polarized antennas," in *Proc. IRE*, pp. 535–540, 1951.

[32] G. Deschamps, "Part ii: Geometrical representation of the polarization of a plane electromagnetic wave," in *Proc. IRE*, pp. 540–544, 1951.

[33] G. Deschamps and P. Mast, "Poincaré sphere representation of partially polarized fields," *IEEE Trans. Antennas Propagat.*, 1973.

[34] M. Kales, "Part III: Elliptically polarized waves and antennas," in *Proc. IRE*, pp. 544–549, 1951.

[35] J. Bohnert, "Part IV: Measurements on elliptically polarized antennas," in *Proc. IRE*, pp. 549–552, 1951.

[36] C. Graves, "Radar polarization power scattering matrix," in *Proc. IRE*, pp. 248–252, 1956.

[37] S. Bickel, "Some invariant properties of the polarization scattering matrix," in *Proc. IEEE*, pp. 1070–1072, 1965.

[38] S. Bickel and R. Bates, "Effects of magneto–ionic propagation on the polarization scattering matrix," Proc. IEEE, 1965.

[39] J. Copeland, "Radar target classification by polarization properties," Proc. IRE, 1960.

[40] O. Lowenschuss, "Scattering matrix application," Proc. IEEE, 1965.

[41] G. Ioannidis and D. Hammers, "Optimum antenna polarizations for target discrimination in clutter," *IEEE Trans. Antennas Propagat.*, vol. 27, pp. 357–363, 1979.

[42] W. Boerner, M. El-Arini, C. Chan, and P. Mastoris, "Polarization dependence in electromagnetic inverse problems," *IEEE Trans. Antennas Propagat.*, vol. 29, pp. 262–271, 1981.

[43] K. Carver, C. Elachi, and F. Ulaby, "Microwave remote sensing from space," Proc. IEEE, 1985.

[44] D. Giuli, "Polarization diversity in radars," Proc. IEEE, 1986.

[45] J. Van Zyl, H. Zebker, and C. Elachi, "Imaging radar polarization signatures," *Radio Science*, vol. 22, pp. 529–543, 1987.

[46] W. Boerner, *Direct and Inverse Methods in Radar Polarimetry.* NATOARW, Kluwer Academic Publishers,, 1992.

[47] F. Ulaby and C. Elachi, *Radar Polarimetry for Geoscience Applications.* Artech House, 1990.

[48] J. Kong, *Polarimetric Remote Sensing.* PIER. Elsevier, 1990.

[49] W. Wiesbeck and D. Kahny, "Single reference, three target calibration and error correction for monostatic, polarimetric free space measurements," Proc. IEEE, 1991.

[50] A. Freeman, Y. Shen, and C. Werner, "Polarimetric SAR calibration experiment using active radar calibrators," *IEEE Trans. Geosci. Remote Sensing*, vol. 28, pp. 224–240, 1990.

[51] A. Freeman, Y. Shen, and C. Werner, "Calibration of Stokes and scattering matrix format polarimetric SAR data," *IEEE Trans. Geosci. Remote Sensing*, vol. 30, pp. 531–539, 1992.

[52] J. Van Zyl, "Calibration of polarimetric radar images using only image parameters and trihedral corner reflector responses," *IEEE Trans. Geosci. Remote Sensing*, vol. 28, pp. 337–348, 1990.

[53] K. Sarabandi and F. Ulaby, "A convenient technique for polarimetric calibration of single–antenna radar systems," *IEEE Trans. Geosci. Remote Sensing*, vol. 28, pp. 1022–1033, 1990.

[54] K. Sarabandi, "Calibration of a polarimetric synthetic aperture radar using a known distributed target," *IEEE Trans. Geosci. Remote Sensing*, vol. 32, pp. 575–582, 1994.

[55] S. Cloude and E. Pottier, "A review of target decomposition theorems in radar polarimetry," *IEEE Trans. Geosci. Remote Sensing*, vol. 34, pp. 498–518, 1996.

[56] E. Krogager, J. Dall, and S. Madsen, "Properties of sphere, diplane and helix decomposition," Proceedings of the 3^{rd} International Workshop on Radar Polarimetry, 1995.

[57] W. Cameron and L. Leung, "Identification of elemental polarimetric scatterer responses in high resolution ISAR and SAR signature measurements," in Proc. 2nd h t . Workshop on Radar Polarimetry (JIPR '92), 1992.

[58] E. Krogager, *Aspects of Polarimetric Radar Imaging.* PhD thesis, Technical University of Denmark, Copenhagen, Denmark,, 1993.

[59] E. Krogager, "Coherent integration of scattering matrices," in Proceedings of Third International Workshop on Radar Polarimetry (JIPR'95), IRESTE, 1995.

[60] E. Krogager and Z. Czyz, "Properties of the sphere, diplahe, helix decomposition," in Proceedings of Third International Workshop on Radar Polarimetry (JIPR'95), IRESTE, 1995.

[61] J. Goodman, "Some fundamental properties of speckle," *J. Opt. Soc. Am.*, vol. 66, pp. 1145–1150, 1976.

[62] J. Lee, I. Jurkevich, P. Dewaele, P. Wambacq, and A. Oosterlinck, "Speckle filtering of synthetic aperture radar images: A review," *Remote Sensing Reviews*, vol. 8, pp. 313–340, 1994.

[63] L. Novak and M. Burl, "Optimal speckle reduction in polarimetric SAR imagery," *Remote Sensing Reviews*, vol. 26, pp. 293–305, 1990.

[64] A. Lopes and F. Sery, "Optimal speckle reduction for the product model on multilook polarimetric SAR imagery and thewishart distribution," *IEEE Trans. Geosci. Remote Sensing*, vol. 35, pp. 632–647, 1997.

[65] M. Mishchenko, "Enhanced backscattering of polarized light from discrete random media: Calculations in exactly the backscattering direction," *J. Opt. Soc. Amer. A*, vol. 9, pp. 978–982, 1992.

[66] M. Mishchenko and J. Hovenier, "Depolarization of light backscatterd by randomly oriented nonspherical particles," *Opt. Lett.*, vol. 20, pp. 1356–1359, 1995.

[67] A. Freeman and S. Durden, "A three component scattering model to describe polarimetric SAR data," *in SPIE, Radar Polarimetry*, vol. 1748, pp. 213–224, 1992.

[68] A. Freeman, S. Durden, and R. Zimmerman, "Mapping sub–tropical vegetation using multi–frequency, multi-polarization SAR data," in Proceedings of the IEEE International Geoscience and Remote Sensing Symposium (IGARSS), 1992.

[69] E. Pottier, J. Lee, and L. Ferro-Famil, *POLSARPRO V3.0 lecture notes advanced concepts.* 2007.

[70] S. R. Cloude, *Lie groups in electromagnetic wave propagation and scattering.* Taylor & Francis, 1995.

[71] E. Rignot, R. Chellapa, and P. Dubois, "Unspervised segmentation of polarimetric SAR data using the covariance matrix," *IEEE Trans. Geosci. Remote Sensing*, vol. 30, pp. 697–705, 1992.

[72] F. Cao, W. Hong, Y. Wu, and E. Pottier, "An unsupervised segmentation with an adaptive number of clusters using the SPAN H/A/α space and the complex wishart clustering for fully polarimetric SAR data analysis," *IEEE Trans. Geosci. Remote Sensing*, vol. 45, pp. 3454–3467, 2007.

[73] P. Ferrazzoli, S. Paloscia, P. Pampaloni, G. Schiavon, S. Sigismondi, and D. Solimini, "The potential of multifrequency polarimetric SARin assessing agricultural and arboreous biomass," *IEEE Trans. Geosci. Remote Sensing*, vol. 35, pp. 5–1t, 1997.

[74] J. Schou and H. Skriver, "Restoration of polarimetric SAR images using simulated annealing," *IEEE Trans. Geosci. Remote Sensing*, vol. 39, pp. 2005–2016, 2001.

[75] S. Fukuda and H. Hirosawa, "A wavelet-based texture feature set applied to classification of multifrequency polarimetric SAR images," *IEEE Trans. Geosci. Remote Sensing*, vol. 37, pp. 2282–2286, 1999.

[76] H. Wang, Y. Pi, and Z. Cao, "Unsupervised classification of polarimetric SAR images based on ICA," Third International Conference on Natural Computation, 2007.

[77] S. Hong and W. Moon, "Application of gaussian markov random field model to unsupervised classification in polarimetric SAR image," Proceedings of Geoscience and Remote Sensing Symposium. IGARSS '03, 2003.

[78] T. Tran, R. Wehrens, L. Buydens, and D. Hoekman, "Initialization of Markov random field clustering of large polarimetric SAR images," Proc. IGARSS 2004, 2004.

[79] J. Yong, Z. Xiao-ling, and S. Jun, "Unsupervised classification of polarimetric SAR image by quad-tree segment and svm," Proceedings of 1st Asian and Pacific Conference on Synthetic Aperture Radar, APSAR 2007., 2007.

[80] C. Lardeux, P. Frison, C. Tison, D. Deleflie, J. Souyris, J. Rudant, and B. Stoll, "Comparison of compact polarimetric with full polarimetric radar data for land use discrimination based on SVM classification," Proc. of the 3rd International Workshop on Science Applications of SAR Polarimetry and Polarimetric Interferometry. PolInSAR 2007, 2007.

[81] N. Rodionova, "A combined use of decomposition and texture for terrain classification of fully polarimetric SAR images," Proc. of the 3rd International Workshop on Science Applications of SAR Polarimetry and Polarimetric Interferometry. PolInSAR 2007, 2007.

[82] H. Hoekman, T. Tran, and M. Vissers, "Unsupervised full-polarimetric segmentation for evaluation of backscatter mechanisms of agricultural crops," Proc. of the 3rd International Workshop on Science Applications of SAR Polarimetry and Polarimetric Interferometry. PolInSAR 2007, 2007.

[83] A. Reigber, M. Jager, M. Neumann, and L. Ferro-Famil, "Polarimetric fuzzy k-means classification with consideration of spatial context," Proc. of the 3rd International Workshop on Science Applications of

SAR Polarimetry and Polarimetric Interferometry. PolInSAR 2007, 2007.

[84] P. Martinez, D. Schertzer, and K. Pham, "Texture analysis by universal multifractal features in polarimetric SAR image," Geoscience and Remote Sensing Symposium. IGARSS '96, 1996.

[85] L. Du and J. Lee, "Polarimetric SAR image classification based on target decomposition theorem and complex wishart distribution," Geoscience and Remote Sensing Symposium. IGARSS '96, 1996.

[86] J. Wang, M. Azimi-Sadjadi, and D. Reinke, "A temporally adaptive classifier for multispectral imagery," *IEEE Trans. Neural Networks*, vol. 15, pp. 159–165, 2004.

[87] F. Del Frate, F. Pacifici, G. Schiavon, and C. Solimini, "Use of neural networks for automatic classification from high–resolution images," *IEEE Trans. Geosci. Remote Sensing*, vol. 45, pp. 800–809, 2007.

[88] F. Del Frate, F. Pacifici, and D. Solimini, "Monitoring urban land cover in Rome, Italy, and its changes by single–polarization multi–temporal SAR images," *IEEE Journal of Selected Topics in Applied Earth Observations and Remote Sensing*, vol. 1, pp. 87–97, 2008.

[89] Y. Hara, R. Atkins, R. Shin, J. Kong, S. Yueh, and R. Kwok, "Application of neural networks for sea ice classification in polarimetric SAR images," *IEEE Trans. Geosci. Remote Sensing*, vol. 33, pp. 740–748, 1994.

[90] M. Hosokawa and T. Hoshi, "Polarimetric SAR data classification method using the self-organizing map," IEEE International Geoscience and Remote Sensing Symposium. IGARSS'02, 2002.

[91] K. Ersahin, B. Scheuchl, and I. Cumming, "Incorporating texture information into polarimetric radar classification using neural networks," Proc. IGARSS 2004, 2004.

[92] S. Ghaloum and M. Azimi-Sadjadi, "Terrain classification in SAR images using principal componentsanalysis and neural networks," IEEE International Joint Conference on Neural Networks, 1991.

[93] M. Azimi-Sadjadi, S. Ghaloum, and R. Zoughi, "Terrain classification in SAR images using principal components analysis and neural networks," *IEEE Trans. Geosci. Remote Sensing*, vol. 31, pp. 511–515, 1993.

[94] K. Chen, W. Huang, D. Tsay, and F. Amar, "Classification of multifreqfuency polarimetric SAR imagery using a dynamic learning neural network," *IEEE Trans. Geosci. Remote Sensing*, vol. 34, pp. 814–820, 1996.

[95] Y. Tzeng and K. Chen, "A fuzzy neural network to SAR image classification," *IEEE Trans. Geosci. Remote Sensing*, vol. 36, pp. 301–307, 1998.

[96] M. Hellmann, G. Jager, E. Kratzschmar, and M. Habermeyer, "Classification of full polarimetric SAR-data using artificial neural networks and fuzzy algorithms," IEEE International Geoscience and Remote Sensing Symposium. IGARSS'99, 1999.

[97] M. Yahia and Z. Belhadj, "Unsupervised classification of polarimetric SAR images using neural networks," IEEE International Geoscience and Remote Sensing Symposium. IGARSS'03, 2003.

[98] R. M. Barnes and W. Holm, "On radar polarization mixed target state," IEEE National radar conference, 1988.

[99] R. Jones, "A new calculus for the treatment of optical systems. description and discussions," *Journal of Optical Society of America*, vol. 31, pp. 488–493, 1941.

[100] R. Jones, "A new calculus for the treatment of optical systems II. proof of the three general equivalent theorems," *Journal of Optical Society of America*, vol. 31, pp. 493–499, 1941.

[101] R. Jones, "A new calculus for the treatment of optical systems III. the stokes theory of optical activity," *Journal of Optical Society of America*, vol. 31, pp. 500–503, 1941.

[102] E. Luneburg, "Principles of radar polarimetry," *Proceedings of the Transactions on Electronic Theory*, vol. E78-C, pp. 1339–1345, 1995.

[103] C. Graves, "Radar polarization power scattering matrix," *Proceedings of the IRE*, vol. 44, pp. 248–252, 1956.

[104] K. Soren, *Bismuth iron garnet films for magneto-optical photonic Crystals.* Stockholm, 2004.

[105] E. Krogager and Z. Czyz, "Properties of sphere, diplane and helix decomposition," Proceedings of the 3^{rd} International Workshop on Radar Polarimetry, 1995.

[106] T. Auermann, *Polarimetrische rararmessungen an der schmelzschicht und deren modelierung.* PhD thesis, DLR, Oberpfaffenhofen, Germany, 1998.

[107] K. Papathanassiou, *Polarimetric SAR interferometry.* PhD thesis, DLR, Oberpfaffenhofen, Germany, 1999.

[108] G. Strang, *Linear Algebra Applications.* Harcourt Brace Jovanovich College Publisher, 1988.

[109] A. Agrawal and W. Boerner, "Redevelopment of Kennaught's target characteristics polarization state theory using the polarization ratio formalism for the coherent case," *IEEE Trans. Geosci. Remote Sensing*, vol. 27, pp. 2–14, 1989.

[110] W. Boerner, W. Yan, A. Xi, and Y. Yamaguchi, "On the principles of radar polarimetry (invited review): The target characteristic polarization state theory of kennaugh, huynen's polarization fork concept, and its extension to the partially polarized case," IEEE Proc. Special Issue on Electromagnetic Theory, 1991.

[111] S. Baronti, F. Del Frate, P. Ferrazzoli, S. Paloscia, P. Pampaloni, and G. Schiavon, "SARpolarimetric features of agricultural areas," *International Journal of Remote Sensing*, vol. 16, pp. 2639–2656, 1995.

[112] F. Ulaby, R. Moore, and A. K. Fung, *Microwave Remote Sensing: Actice and Passive.* vol. II, Surface Scattering and Emission Theory, Addison–Wesley, 1982.

[113] M. Karam, A. Fung, R. Lang, and N. Chauhan, "A microwave scattering model for layered vegetation," *IEEE Trans. Geosci. Remote Sensing*, vol. GE–30, pp. 767–784, 1992.

[114] P. Ferrazzoli, D. Solimini, G. Luzi, and S. Paloscia, "Interpretation of Polarimetric MAC-91 data over Montespertoli agricultural area," *J. of electromagnetic Waves and Applications*, vol. 5, pp. 175–193, 1991.

[115] G. Sinclair, "Modifications of the radar range equation for arbitrary target and arbitrary polarizations," *Report 302–19, Antenna Laboratory, The Ohio State University Research Fundation*, 1948.

[116] F. Ulaby and K. Sarabandi, "Statistical properties of the Müller matrix of distributed targets," *IEEE Proceedings–F: Remote Sensing Radar*, vol. 2, pp. 136–146, 1992.

[117] D. Deirmendijan, *Electromagnetic scattering on spherical polydispersions.* Elsevier, New York, USA, 1969.

[118] H. Hulst, *Light scattering by small particles.* J. Wiley, New York, USA, 1957.

[119] A. Guissard, *Radar polarimetry with applications to satellite remote sensing.* TELE, U.C.L, 2003.

[120] L. E., "A revisitation of basic concepts," in A.H. Serbest and S.R. Cloude (eds.) Direct and inverse Scattering, 1996.

[121] S. Cloude, *Polarimetry: The Characterization of Polarimetric Effects in EM Scattering.* PhD thesis, University of Birmingham, UK, 1999.

[122] M. Borgeaud, "Theoretical models for polarimetric microwave remote sensing of earth terrain,," *Journal of Electromagnetic Waves and Applications*, vol. 3, pp. 61–81, 1989.

[123] S. R. Cloude, *Uniqueness of target decomposition theorems in radar polarimetry.* in Direct and Inverse Methods in Radar Polarimetry, Part I, NATO-ARW(W.M. Boerner et al., eds., Kluwer Academic Publishers), 1992.

[124] K. Tragl, "Polarimetric radar backscattering from reciprocal random targets," *IEEE Trans. Geosci. Remote Sensing*, vol. 28, pp. 590–597, 1990.

[125] J. Lee, K. Hoppel, S. Mango, and A. Miller, "Intensity and phase statistics of multi–look polarimetric and interferometric SAR imagery," *IEEE Trans. Geosci. Remote Sensing*, vol. 32, pp. 1017–1028, 1994.

[126] J. Lee, "Speckle suppression and analysis for synthetic aperture radar images," *SPIE Optical Engineering*, vol. 25, pp. 636–643, 1986.

[127] J. Lee, M. Grunes, and R. Kwok, "Classification of multi–look polarimetric SAR imaging based on complex Wishart distributions," *International Journal of Remote Sensing*, vol. 15, pp. 2299–2311, 1994.

[128] J. Lee, M. Grunes, and G. De Grandi, "Polarimetric SAR speckle filtering and its implications for classification," *IEEE Trans. Geosci. Remote Sensing*, vol. 37, pp. 2363–2373, 1999.

[129] F. Pacifci, F. Del Frate, C. Solimini, and W. Emery, *Neural Networks for Land Cover Applications.* in Computational intelligence for remote sensing, Manuel Grana, Richard Duro, Eds. Studies in Computational Intelligence, Springer, 2008.

[130] H. Skiver, J. Dall, T. Le Toan, S. Quegan, L. Ferro-Famil, E. Pottier, P. Lumsdon, and R. Moshammer, "Agriculture classification using polSAR data," Proc. POLinSAR Workshop, 2005.

[131] D. Watts, *Land cover mapping by combinations of multiple artificial neural networks.* PhD thesis, University of Calgary, Canada, 2001.

[132] C. Putignano, G. Schiavon, D. Solimini, and B. Trisasongko, "Unsupervised classification of a central italy landscape by polarimetric L-band SAR data," Geoscience and Remote Sensing Symposium. IGARSS '05, 2005.

[133] M. Del Greco, "Uso di mappe di kohonen per la classificazione di dati SAR polarimetrici," Master's thesis, Tor Vergata University, Rome, Italy, 2006.

[134] D. Hoekman and M. Vissers, "A new polarimetric classification approach evaluated for agricultural crops," *IEEE Trans. Geosci. Remote Sensing*, vol. 41, pp. 2881–2889, 2003.

[135] J. Lee and M. Vissers, "Digital image enhancement and noise filtering by use of local statistics," *IEEE Trans. on Pattern Analysis and Machine Intelligence*, vol. PAMI–2, pp. 165–168, 1980.

[136] A. Lopes, R. Touzi, and E. Nezry, "Adaptive speckle filters and scene heterogeneity," *IEEE Trans. Geosci. Remote Sensing*, vol. 28, pp. 992–1000, 1990.

[137] J. Daida, R. Samadani, and J. F. Vesecky, "Object-oriented feature tracking algorithms for SAR image of the marginal ice zone," *IEEE Trans. Geosci. Remote Sensing*, vol. 28, pp. 573–589, 1990.

[138] G. Hene and S. Guatama, "Optimisation of a coastline extraction algorithm for object-oriented matching of multisensor satellite imagery," Geoscience and Remote Sensing Symposium. IGARSS '00, 2000.

[139] H. Ghassemian and D. A. Landgrebe, "Object–oriented feature extraction method for image data compaction," *IEEE Control Systems Magazine*, vol. 8, pp. 42–48, 1998.

[140] U. Benz, P. Hofmann, G. Willhauck, I. Lingenfelder, and M. Heynen, "Multi-resolution, object-oriented fuzzy analysis of remote sensing data for gis-ready information," *ISPRS Journal of Photogrammetry and Remote Sensing*, vol. 58, pp. 239–258, 2004.

[141] M. Baatz and A. Schape, *Multiresolution segmentation an optimization approach for high quality multi-scale image segmentation.* In: Strobl, J., Blaschke, T., Griesebner, G. (Eds.), Angewandte Geographische Informations-Verarbeitung XII. Wichmann Verlag, Karlsruhe,, 2000.

[142] H. Anys, A. Bannari, D. He, and D. Morin, "Texture analysis for the mapping of urban areas using airborne MEIS–II images," First International Airborne Remote Sensing Conference and Exhibition, 1994.

[143] A. Burini, C. Putignano, F. Del Frate, M. Lazzarini, G. Licciardi, C. Pratola, G. Schiavon, D. Solimini, and P. Manunta, "TerraSAR–X imaging for unsupervised land cover classification and fire mapping," IEEE International Geoscience and Remote Sensing Symposium. IGARSS'08, 2008.

[144] A. Burini, C. Putignano, F. Del Frate, G. Licciardi, G. Schiavon, and D. Solimini, "TerraSAR–X/SPOT–5 fused images for supervised land cover classification," IEEE International Geoscience and Remote Sensing Symposium. IGARSS'08, 2008.

Curriculum Vitae

COSIMO PUTIGNANO

He received MS in Telecommunications Engineering Summa Cum Laude from the Tor Vergata University, Rome, defending the thesis entitled "SAR Polarimetry for unsupervised classification: Entropy, Anisotropy, alpha angle method".

From 2003 to March 2005 he was with SIPAL S.p.A. where he has been involved in the development of technical documentation for electronic devices for defense applications.

From April 2005 to April 2009, he was a Remote Sensing Engineer of GEO-K S.r.l., a Tor Vergata University spin-off company provider of Earth Observation based services.

Since May 2009, he's Sentinel-1 PDGS (Payload Data Ground Segment) Performance Engineer in ESA-ESRIN, Frascati (Rome)–Italy.

He participated in international remote sensing Conferences and Projects, mostly regarding the use of satellite data (Optical and Radar) for the production of land cover and change detection maps. He is also reviewer for IEEE Geoscience and Remote Sensing Letters and Rivista Italiana di Telerilevamento.

List of Publications

- **C. Putignano**, G. Schiavon, D. Solimini, B. Trisasongko, "Unsupervised classification of a Central Italy landscape by polarimetric L-band SAR data", IGARSS'05, Seoul, Korea, July 2005.
- E. Angiuli, F. Del Frate, G. Licciardi, **C. Putignano**, "Un algoritmo di rete neurale per la produzione di mappe di sealing da dati satellitari LANDSAT", Workshop congiunto AIT e SIFET sul Rilevamento Urbano da Piattaforma Aerea e Satellitare, Mantova, Italy, December 2005.
- **C. Putignano**, G. Schiavon, D. Solimini, B. Trisasongko, "Self-organizing neural networks for unsupervised classification of Polarimetric SAR data on complex landscapes", IGARSS'06, Denver, Colorado, U.S.A., August 2006.
- F. Del Frate, M. Del Greco, G. Schiavon, D. Solimini, **C. Putignano**, "Uso di reti neurali non supervisionate per la classificazione di dati SAR polarimetrici", XIII Riunione Cetem, IV Workshop AIT sul Telerilevamento a Microonde, Politecnico di Milano, November 2006.
- F. Del Frate, M. Del Greco, G. Schiavon, D. Solimini, **C. Putignano**, "Self-organizing maps of polarimetric SAR imagery", POLinSAR 2007, ESRIN, Frascati, Italy, January 2007.

- F. Del Frate, M. Del Greco, D. Solimini, **C. Putignano**, "Unsupervised classification of polarimetric SAR imagery by self-organizing neural networks", ESA-EUSC 2006: Image Information Mining for Security and Intelligence, EUSC, Torrejon Air Base - Madrid, Spain, November 2006.

- **C. Putignano**, Fabio Del Frate, Daniela Iasillo, Gerardo Sanchez Pea, Roberto Vallejo, Espen Volden, Thomas Hausler, "GSE Forest Monitoring project and the Spanish case", Earsel'07, Bolzano, Italy, June 2007.

- A.Burini, F. Del Frate, M. Del Greco,**C. Putignano**, G. Schiavon, D. Solimini "A neural approach to unsupervised classification of very-high resolution polarimetric SAR data", IGARSS'07, Barcelona, Spain, July 2007.

- **C. Putignano**, F. Del Frate, L. Licciardi, G. Schiavon, D. Solimini, "Multi-temporal SAR images at X-band: scattering features and potential in land cover classification", IGARSS'07, Barcelona, Spain, July 2007.

- **C. Putignano**, F. Del Frate, G. Licciardi, D. Iasillo, G. S. Pea, R. Vallejo,E. Golden, T. Hausler, "An innovative algorithm based on Neural Network applied to forestry mapping in GSE Forest Spanish case",ForestSAT'07, Montpellier, France, November 2007.

- **C. Putignano**, A. Burini, F. Del Frate, D. Iasillo, G. Signorile, "Produzione di mappe tematiche da dati satellitari:integrazione tra metodologie neurali e ad oggetti",11a Conferenza Nazionale ASITA, Torino, Italy, November 2007.

- A. Burini, **C. Putignano**, F. Del Frate, G. Licciardi, G. Schiavon, D. Solimini, "TerraSAR-X/SPOT5 fused images for supervised land cover classification",IGARSS'08, Boston, Massachusetts (U.S.A.), July 2008.

- A. Burini, **C. Putignano**, F. Del Frate, M. Lazzarini, G. Licciardi, C. Pratola, G. Schiavon, D. Solimini, F. De Biasi, P. Manunta, "TerraSAR-X imaging for unsupervised land cover classification and fire mapping",IGARSS'08, Boston, Massachusetts (U.S.A.), July 2008.

- G. Licciardi, F. Del Frate, **C. Putignano**, C. Pratola, "Tasseled Cap transformation and neural networks for the design of an optimum image classification algorithm using multispectral data", IGARSS'08, Boston, Massachusetts (U.S.A.), July 2008.

- F. Del Frate, M. Lazzarini, G. Licciardi, **C. Putignano**, C. Pratola, "Una procedura completamente automatica per la classificazione di immagini satellitari", XIV Riunione Annuale CeTeM / V Workshop AIT / XIV Giornata MECSA sull'Ingegneria delle Microonde, Roma, 23-24 Ottobre 2008.

- F. Del Frate, M. Del Greco, C. Pratola, **C. Putignano**, and D. Solimini, "Fully automatic land cover maps generation using polarimetric SAR data", in POLinSAR 2009, Frascati, Rome (Italy)

- J. Patruno, N. Dore, A. B. Ruescas, M. Lavalle, **C. Putignano**, A. M. Jaja, G. Galdieri, E. Loret and F. Sarti, "Preliminary results of ALOS PALSAR imaging for investigation of archaeological underground marks", in POLinSAR 2009, Frascati, Rome (Italy)

List of Tables

List of Figures